SMALL SCALE STOCHASTIC DYNAMICS FOR PARTICLE IMAGE VELOCIMETRY APPLICATIONS

A Thesis
Presented to
The Academic Faculty

by

Christel Hohenegger

In Partial Fulfillment
of the Requirements for the Degree
Doctor of Philosophy in the
School of Mathematics

Georgia Institute of Technology
May 2006

SMALL SCALE STOCHASTIC DYNAMICS FOR PARTICLE IMAGE VELOCIMETRY APPLICATIONS

Approved by:

Professor Peter J. Mucha, Adviser
School of Mathematics
Georgia Institute of Technology

Professor Evans M. Harrell
School of Mathematics
Georgia Institute of Technology

Professor Minami Yoda
School of Mechanical Engineering
Georgia Institute of Technology

Professor Haomin Zhou
School of Mathematics
Georgia Institute of Technology

Professor Guillermo Goldsztein
School of Mathematics
Georgia Institute of Technology

Date Approved: 03/16/2006

ACKNOWLEDGEMENTS

First, I would like to thank my adviser, Peter Mucha, for directing me towards exciting areas of applied mathematics at a time when analysis and partial differential equations had lost their attractions. He always trusted my ability to solve problems by myself and gave me a lot of freedom.

I would like to thank Minami Yoda for serving on my committee, for writing the letter of recommendations and for all the support she provided during this last year. Thanks also to Haifeng for fruitful discussions and clear descriptions of the experimental world.

I thank Professor Harrell for writing the letter of recommendation and serving on my committee, Professors Goldsztein and Zhou for serving on my committee and Professors McCuan and Loss for their help during my study in the School of Mathematics.

Computers sometimes have incomprehensible reactions. Thanks to Lew and Justin for fixing all my mysterious crashes and giving me access to plenty of computer resources.

Al tough she never understood why I had to study across the ocean, my sister Cathy has always been there to help me when nothing was working and to share amazing trips.

I would never have reached this point without the unconditional support of my parents who encouraged us to always be curious of new phenomena and to work hard for what we desire.

It has not always been easy, but those five years have been full of discoveries and new experiences. Thanks to Michael, Ian, Sam, Bill and Allison for in their own way widening my horizon and thanks to all my friends in Atlanta for a great time.

TABLE OF CONTENTS

LIST OF TABLES

LIST OF FIGURES

LIST OF ALGORITHMS

SUMMARY

Fluid velocities and Brownian effects at nanoscales in the near-wall region of microchannels can be experimentally measured in an image plane parallel to the wall using, for example, evanescent wave illumination technique combined with particle image velocimetry (see [29]). The depth of field of this technique being difficult to modify, reconstruction of the out-of-plane dependence of the in-plane velocity profile remains extremely challenging. Tracer particles are not only carried by the flow, but they undergo random fluctuation imposed by the proximity of the wall. We study such a system under a particle based stochastic approach (Langevin) and a probabilistic approach (Fokker-Planck). The necessary modeling assumptions are presented first. The Langevin description leads to a coupled system of stochastic differential equations. Because the simulated data will be used to test a statistical hypothesis, we pay particular attention to the strong order of convergence of the scheme developing an appropriate Milstein scheme of strong order of convergence 1. Based on the probability density function of mean in-plane displacements, a statistical solution to the problem of the reconstruction of the out-of-plane dependence of the velocity profile is proposed. We developed a maximum likelihood algorithm which determines the most likely values for the velocity profile based on simulated perfect particle position, simulated perfect mean displacements and simulated observed mean displacements. Effects of Brownian motion on the approximation of the mean displacements are briefly discussed. A matched particle is a particle that starts and ends in the same image window after a measurement time. AS soon as the computation and observation domain are not the same, the distribution of the out-of-plane distances sampled by matched particles during the measurement time is not uniform. The combination of a forward and a backward solution of the one dimensional Fokker-Planck equation is used to determine this probability density function. The non-uniformity of the resulting distribution is believed to induce a bias in the determination of slip length and is quantified for relevant experimental parameters.

CHAPTER I

INTRODUCTION

One of the many ways of measuring fluid in a channel is to illuminate small tracer particles to record their images through a camera. Under the assumption that the tracer particles follow the flow, a full three-dimensional velocity profile can be reconstructed by properly rotating the sample or changing the angle of illumination. Standard illumination techniques include spectroscopy and multiple laser sheets illumination (see [1], [37]). The limitation of tracking algorithms, which follow the position of every single tracer particle, and the desire for higher velocity field resolution has led to the development by Meinhart *et al.* ([35], [22], [36]) of a new technique. Micron-resolution particle image velocimetry (μPIV) combines improvements in instrument hardware with post processing algorithms to gain accuracy in the measurement and improve the spacial resolution from about 1 mm to about 1 μm. As microfluidic devices become smaller, the out-of-plane spatial resolution of approximately 2 μm of μPIV needs to be overcome in order to obtain velocity data in the near-wall region. The well established technique of illumination through multiple laser-sheets failing to provide fine enough measurements, a new illumination technique using evanescent wave has been proposed by Zettner *et al.* ([38]) and Sadr *et al.* ([29]). This method reduces the out-of-plane spatial resolution to approximately 400 nm, creating in the same time new experimental and theoretical questions about the influence of the wall and about what is effectively measured.

The work of this thesis is based on some of the problems and questions encountered by the group of Minami Yoda in the Woodruff School of Mechanical Engineering at the Georgia Institute of Technology.

1.1 Experimental Set-up

We begin by describing the techniques used by Yoda *et al.* to obtain velocity images at nanoscales. Figure 1 illustrates the experimental set-up around the region of interest (ROI) and some of the inherent experimental restrictions in terms of relative width, height and depth of the channel. Including the near-wall region of microchannels, Yoda *et al.* ([38],

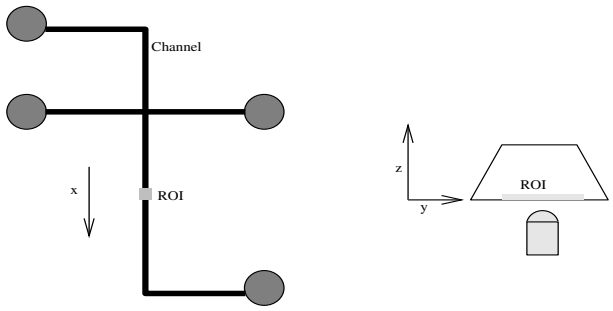

Figure 1: Experimental set-up: Region of interest (ROI), flow direction and wall location.

[29]) extend PIV to flows illuminated with evanescent waves generated by total internal reflection of a beam of light. Light undergoes total internal reflection between a medium (glass plate) and a less dense medium (water) when the angle of incidence exceeds the critical angle. An evanescent wave penetrates into the less dense medium and propagates parallel to the interface with an intensity that decays exponentially with the distance normal to the wall (see Fig. 2 and [38], [31]). The fluorescent particles illuminated by the evanescent wave are captured on a camera with a measurement time of approximately 2-5 ms.

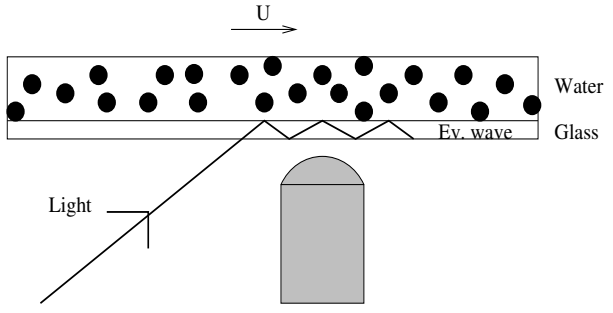

Figure 2: Evanescent wave illumination technique.

A background image consisting of the average of all images is then subtracted from all individual images to improve the contrast between the particle images and the background

noise ([29]). The result is an image matrix as illustrated in figure 3. Next, image pairs are

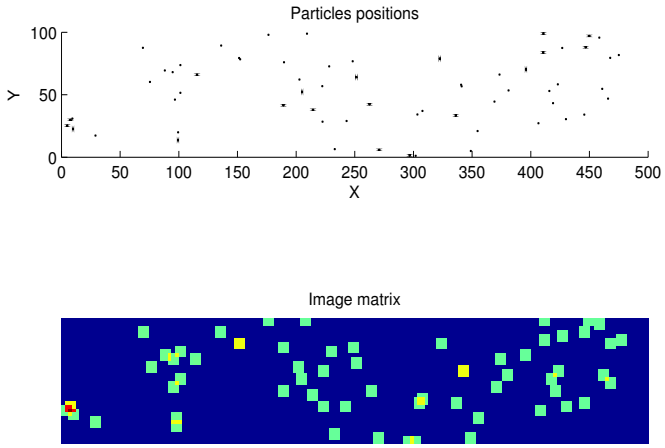

Figure 3: Simulated image flow and resulting image matrix.

cross-correlated and the location of the maximum of the cross-correlation peak is used to determine in-image-plane mean velocities. Subpixel accuracy is achieved through the use of a Gaussian surface fitting algorithm (see [35], [19], [22], [21], [38], [29]).

1.2 Experimental Results

In a laminar flow, Fuller *et al.* ([7]) show that it is possible to reconstruct the velocity gradient using light-scattering spectroscopy. This requires the knowledge of the intensity function and the technical capacity of turning the sample to get a proper angle of illumination. This last requirement can not be achieved with nPIV, because the images are limited to in-plane (parallel to the wall) images. However, since the evanescent wave has an intensity that decays exponentially away from the wall, the $z-$location (z distance normal to the wall) of a particle can be correlated to its image intensity. Using this idea, Li *et al.* ([18]) have proposed extending nPIV to multilayer nPIV for determining the velocity component tangential to the wall at several z-locations given an appropriate division of the

image into layers based on intensity. This new technique is extremely challenging, especially since background noise pollutes the images, while tracer non-uniformity corrupts the identification of particle position into layers.

At microscale, the effect of Brownian motion is independent of z. Therefore its effect on the height and the width of the cross-correlation peak can be explicitly quantified (see [23], [24], [26], [25]) leading to proper characterization of window size and windows overlapping. Moreover, a better resolution can be obtained when the consecutive cross-correlation functions are averaged over successive window pairs reducing the error due to Brownian motion at microscale to a negligible factor (see [21], [35], [36]).

Because nPIV with evanescent wave does not illuminate the entire microchannel, velocity measurements are limited to near-wall region over a distance comparable to the illumination wavelength (see [38], [29]). Therefore, Brownian motion and particle mismatch between two images are an important issue. Sadr *et al.* ([29]) show that hindered Brownian motion (the presence of the wall changes the drag coefficients and resulting Brownian motions of a particle because of its hydrodynamic interaction with the wall) creates additional errors in the measurements, especially if the particle mismatch (we say that a particle is mismatched if it only appears in one image of a PIV image pair, because of its motion during the time interval) between two windows exceeds 45%. The percentage of particle mismatch itself is a function of the dimensionless diffusion time $D_\infty T/a^2$, where D_∞ is the Stokes-Einstein diffusion coefficient in the region away from the wall, T is the time interval between two windows and a is the radius of the particles.

Questions remain about the influence of hindered Brownian diffusion on measured velocity profiles, in particular, when extrapolating slip length from the velocity profile. Slip lengths of various order of magnitudes have been reported and explanations ranging from the non-smoothness of the glass surface, to the presence of an air layer or to electro-kinetic effects have been proposed (see [20], [15], [17], [16], [11],[32], [34], [12]). Considering this problem

as a result of Brownian diffusion, Sadr *et al.*([30]) computationally determine the bias in the z-distribution of matched particles.

1.3 Motivation

The information lost with in-plane images is vital to the characterization of physical properties of the flow (see [31]). Since distinguishing particle brightness given by the intensity function from background noise remains extremely challenging, we want to find an alternate method to reconstruct the out-of-plane dependence of the velocity profile. The method is a statistical approach based on the probability density function of the displacement. Choosing a probabilistic point of view should also allow for a more precise discussion of the influence of Brownian motion on the cross-correlation function and of the bias generated by particle mismatch. In order to prove that the concept is valid, a computer model will be constructed and results will be derived from simulated data similar to experimental data. Because of the numerous technical uncertainties, we hope that simplifying the problem will enable us to pinpoint dominant effects and parameters of measured flows in near-wall region.

1.4 Outline

Constructing a computer model requires first to choose the adequate framework for the problem and second to simplify and neglect some experimental parameters. Both of these aspects are presented in chapter 2 describing the derivation of a particle model using a Langevin and a Fokker-Planck approach.

Because of hindered Brownian diffusion, the Langevin system of equations is stochastic and we present its numerical simulation in chapter 3. Numerical methods for stochastic differential equations are more complicated than those for non-stochastic systems and become even more complicated for uncoupled system. In our case, Brownian diffusion depends on z, thus the system is coupled through the z-coordinate. The reconstruction method being of probabilistic type, we want the simulation to have higher order of strong convergence

than that used in the reconstruction technique. Therefore we need to include higher order terms to improve the Euler-Maruyama (equivalent to a deterministic forward Euler) scheme of strong order of convergence 1/2 to a Milstein scheme of strong order of convergence 1. Computation of Ito-integrals with respect to two distinct Brownian motions are carefully discussed in Chapter 3.

Having at our disposal a robust code, we can proceed to the main result about the reconstruction of velocity profile using a statistical method (see [10]). This part covers chapters 4 to 6 each one of them including elements closer to the experiments. To test the validity of the reconstruction algorithm we first limit ourselves to perfect particle identification in chapter 4. Experimentally, this corresponds to a particle tracking algorithm where the position of each particle is exactly known. Because nPIV techniques produce an approximation of the mean displacements, we extend in chapter 5 the algorithm to exact mean measurement of displacements between two windows. This remains an idealization, since the computer simulation provides us with the exact value for the mean displacements. Having demonstrated that a statistical reconstruction algorithm is valid, we finally discuss, in chapter 6, the additional error generated when the mean displacements are not exact but approximated via cross-correlation. Moreover, in chapter 6 we also describe the details of a PIV algorithm similar to the one used by the experimentalists.

Next, we turn our attention to the bias in the distribution of matched particles and present in chapter 7 an algorithm for the generation of the probability density function of the z-distance of particles present in the window at the beginning and end of the measurement. The algorithm is extremely fast, since it does not require the knowledge of the position of each particle but uses a probability density function computed from the Fokker-Planck equation. Applications to the determination of the bias and corrections to slip length terms are also presented.

Finally, we discuss in chapter 8 results on correction terms that could be used in the

quantification of the effects of hindered Brownian diffusion on the width and height of the cross-correlation peak.

We conclude by discussing possible improvements of the model and directions for further research.

CHAPTER II

PARTICLE MODEL

What makes the problem of measurement of fluid velocities in near-wall region interesting is the fact that tracer particles are not only carried by the flow, but their random Brownian motions are affected by the presence of the wall. This is not some type of reflection at the wall, but a random forcing whose magnitude depends on the distance from the wall. It is obvious that, in the bulk region, tracers follow the flow on average and the wall has no influence. In this chapter, we present two ways (Langevin or Fokker-Planck) of describing a Brownian system with non-constant diffusion tensor. In doing so, we make some simplifying assumptions on the nature of the underlying flow and we always assume that the perfect spherical particles do not interact with each other, a reasonable assumption since the volume fraction in practical applications is smaller than 10^{-3}. Proceeding with a dimensional analysis, we derive a stochastic particle based (Langevin) and a probabilistic (Fokker-Planck) description with characteristic dimensionless parameters of a simplified stochastic system that retains the main properties of the experimental model.

2.1 Langevin Description

We describe the problem as a simple stochastic model of particle motions. Each particle is assumed to have a fixed radius a and we consider a system of n Brownian particles obeying Stokes drag relations, linearly dependent on the velocity. A general description of such systems is provided by Ermak and McCammon ([6]) starting from Newton's law

$$m_i \dot{v}_i = -\sum_{j=1}^{3n} M_{ij} v_j + F_i + \sum_{j=1}^{3n} \alpha_{ij} f_j \quad i = 1, \ldots, 3n. \tag{1}$$

$\mathbf{F}$ describes the external and interaction forces and $\mathbf{M}$ is the mobility tensor related to the configuration diffusion tensor $\mathbf{D}$ by $\mathbf{MD} = \mathbf{DM} = k\Theta\mathbf{I}$ with k Boltzmann constant, Θ temperature, and $\mathbf{I}$ is the identity tensor. The random forcing $\mathbf{f}$ is described by a Gaussian

distribution with mean $\overline{f_i} = 0$ and covariance $\overline{f_i(t)f_j(t')} = 2\delta_{ij}\delta(t-t')$. The matrix α is given by the relation $k\Theta\mathbf{M} = \alpha\alpha^T$.

For a time step dt bigger than the force relaxation time $m_i D_{ii}/k\Theta$, Ermak and McCammon show that the previous equation for a position vector $\mathbf{r}$ leads to

$$dr_i = \sum_{j=1}^{3n} \frac{\partial D_{ij}}{\partial r_j} dt + \sum_{j=1}^{3n} \frac{D_{ij}F_j}{k\Theta} dt + W_i(dt), \quad i = 1, \ldots, 3n, \tag{2}$$

where $W_i(dt)$ is a random displacement with a Gaussian distribution function whose average value is zero and whose variance-covariance matrix is $2\mathbf{D}dt$. The Brownian displacement can be expressed as

$$W_i(dt) = \sum_{j=1}^{i} \sigma_{ij} dW_j \quad \sigma = \sqrt{2\mathbf{D}dt} \quad dW_j = \mathcal{N}(0,1), \quad j = 1, \ldots, 3n, \tag{3}$$

using the notation $\mathcal{N}(\mu_0, \sigma_0^2)$ for a normal random variable of mean μ_0 and variance σ_0^2.

2.2 Fokker-Planck Description

Another way of describing the system when interested by statistical properties and not exact particle location is to use the Fokker-Planck equation. The n particle phase-space distribution function $\mathcal{W}(\{r_i\}, \{p_i\}, t)$ is the average number density of particles with position r_i and momentum p_i at time t which evolves from the initial distribution $\mathcal{W}(r_i, p_i, 0)$.

Under the assumption that the momentum variables relax to equilibrium more rapidly than the position variables ($dt \gg m_i D_{ii}/k\Theta$), the equation for the n particle system is ([6])

$$\frac{\partial \mathcal{W}}{\partial t} = \sum_{i=1}^{3n} \sum_{j=1}^{3n} \frac{\partial}{\partial r_j} D_{ij} \left(\frac{\partial \mathcal{W}}{\partial r_j} - \frac{1}{k\Theta} F_j \mathcal{W} \right), \tag{4}$$

where $\mathcal{W}(\{r_i\}, t)$ is the configuration space distribution function and $\mathbf{D}$, $\mathbf{F}$ are the diffusion tensor and the force vector as defined in section 2.1.

2.3 Diffusion Tensor

2.3.1 Approximation through images

A first approximation of the non-constant diffusion tensor is obtained by the methods of image singularities for Stokes flows ([28], [5]), valid for particle center-to-wall distance, z, that is large compared to the particle radius, a. Let μ be the viscosity of water, keeping in mind that μ depends on the temperature Θ. Assuming that there is no contribution from the particle neighbors, the diffusion tensor can be expressed as ([28])

$$\begin{aligned} D_{ij} &= k\Theta\left(\frac{\delta_{ij}}{6\pi\mu a} + G^W_{ij}(2z\mathbf{e}_z)\right) \\ &= k\Theta\left(\frac{\delta_{ij}}{6\pi\mu a} - G^S_{ij}(2z\mathbf{e}_z) + 2z^2 G^D_{ij}(2z\mathbf{e}_z) - 2z G^{SD}_{ij}(2z\mathbf{e}_z)\right), \end{aligned} \tag{5}$$

where $\mathbf{G}^W$, $\mathbf{G}^S$, $\mathbf{G}^{SD}$, $\mathbf{G}^D$ are the Green tensor associated with the wall, a stokeslet, a stokeslet doublet, and a source doublet and z is the particle center-to-wall distance with unit direction vector $\mathbf{e}_z$. This leads to the diffusion tensor $\mathbf{D}$ ([5])

$$\mathbf{D} = \frac{k\Theta}{6\pi\mu a}\begin{pmatrix} 1-\frac{9}{16}\frac{a}{z} & 0 & 0 \\ 0 & 1-\frac{9}{16}\frac{a}{z} & 0 \\ 0 & 0 & 1-\frac{9}{8}\frac{a}{z} \end{pmatrix} = D_\infty \beta(z), \tag{6}$$

where $D_\infty = k\Theta/(6\pi\mu a)$ is the Stokes-Einstein relation in the bulk limit far from the wall.

2.3.2 Hindered diffusion

The out-of-plane diffusion perpendicular to the wall has the physically impermeable property that the diffusion coefficient goes to zero for a spherical particle touching the wall ($z = a$). This is not satisfied by the diffusion tensor (6), but it is satisfied by the empirical Bevan-Prieve relation (see [2]). Experimental verification shows that the infinite series representing the modified diffusion coefficient in the out-of-plane direction z can be approximated by the rational function

$$D_{33} = \frac{k\Theta}{6\pi\mu a}\frac{6z^2 - 10az + 4a^2}{6z^2 - 3az - a^2}. \tag{7}$$

Correction terms can also be found for the in-plane component leading to a power series in a/z (see [29])

$$D_{11} = D_{22} = \frac{k\Theta}{6\pi\mu a}\left(1 - \frac{9}{16}\frac{a}{z} + \frac{1}{8}\left(\frac{a}{z}\right)^3 - \frac{45}{256}\left(\frac{a}{z}\right)^4 - \frac{1}{16}\left(\frac{a}{z}\right)^5\right). \tag{8}$$

Considering for simplicity only the lowest-order a/z corrections for diffusion components parallel to the wall and the Bevan-Prieve relation, the diffusion tensor is found to be

$$\mathbf{D} = \frac{k\Theta}{6\pi\mu a}\begin{pmatrix} 1 - \frac{9}{16}\frac{a}{z} & 0 & 0 \\ 0 & 1 - \frac{9}{16}\frac{a}{z} & 0 \\ 0 & 0 & \frac{6z^2 - 10az + 4a^2}{6z^2 - 3az - a^2} \end{pmatrix} = D_\infty \beta(z). \tag{9}$$

2.4 External Force: Hydrodynamic

For a force-free fluid velocity fluid $\mathbf{u}$ of the particles themselves, the hydrodynamic forces on the particle is given by $k\Theta\mathbf{D}^{-1}(\mathbf{u} - \mathbf{U})$ for tracer particle velocity $\mathbf{U}$. Because of hydrodynamic balance $\mathbf{u} = \mathbf{U}$ and the external force $\mathbf{F}$ becomes

$$\mathbf{F} = k\Theta\mathbf{D}^{-1}\mathbf{u}. \tag{10}$$

In the physical experiments, additional corrections are required to relate the force-free velocity profiles of the tracers to that of the flow ([11]).

2.5 Flow

We consider a velocity profile $\mathbf{u}$ directed in one in-plane direction x and a simulated channel of height H. Experimentally three different flows are most frequently encountered: shear flow, pressure-driven flow, and electro-osmotically pumped flow.

Let u_∞ be the "bulk" velocity and $\mathbf{e}_x$ be the unit vector in the x-direction. We set $\mathbf{u} = u_\infty\gamma(z)\mathbf{e}_x$, where the dependence from the out-of-plane component z is $\gamma(z)$. Corresponding

to the three experimental cases (shear, pressure-driven and electro-osmotically pumped), we have

$$\gamma(z) = \frac{1}{H-a}(z-a) \qquad \text{linear} \tag{11}$$

$$\gamma(z) = \frac{4}{(2H-a)^2} z(2H-z) \qquad \text{parabolic} \tag{12}$$

$$\gamma(z) = 1 - \exp(1 - z/a) \qquad \text{exponentially decaying.} \tag{13}$$

2.6 Particle Model

2.6.1 Explicit Langevin model

We denote by x the component parallel to the wall in which the flow is directed, y the component parallel to the wall affected only by random fluctuation and z the component perpendicular to the wall. Consequently the three non-zero components of the diffusion tensor can be expressed as $\beta_{11}(z) = \beta_{22}(z) = \beta_{||}(z)$ and $\beta_{33}(z) = \beta_{\perp}(z)$.

Combining the results from the previous sections, we derive the simplified Langevin model. We set $\mathbf{u} = u_\infty \gamma(z)\mathbf{e}_x$ with $\gamma(z)$ given by (11)-(13). The external force $\mathbf{F}$ is given by (10). Substituting these assumptions together with the out-of-plane dependent diffusion tensor $\mathbf{D}$ (9) into the Langevin model (2)-(3) we obtain the system of stochastic differential equations

$$dx = u_\infty \gamma(z)dt + \sqrt{2D_\infty \beta_{||}(z)dt}dW^1, \tag{14}$$

$$dy = \sqrt{2D_\infty \beta_{||}(z)dt}dW^2, \tag{15}$$

$$dz = D_\infty \frac{d\beta_\perp(z)}{dz}dt + \sqrt{2D_\infty \beta_\perp(z)dt}dW^3, \tag{16}$$

with $dW^i = \mathcal{N}(0,1), i = 1, \ldots, 3$.

2.6.2 Explicit Fokker-Planck equation

The statistical description of the system through the Fokker-Planck equation (4) results from the same assumptions as in the Langevin model into a space-time partial differential

equation

$$\begin{aligned}\frac{\partial \mathcal{W}(x,y,z,t)}{\partial t} =& D_\infty \beta_{||}(z)\frac{\partial^2 \mathcal{W}(x,y,z,t)}{\partial x^2} - u_\infty \gamma(z)\frac{\partial \mathcal{W}(x,y,z,t)}{\partial x} \\ &+ D_\infty \beta_{||}(z)\frac{\partial^2 \mathcal{W}(x,y,z,t)}{\partial y^2} + D_\infty \frac{d\beta_\perp(z)}{dz}\frac{\partial \mathcal{W}(x,y,z,t)}{\partial z} \\ &+ D_\infty \beta_\perp(z)\frac{\partial^2 \mathcal{W}(x,y,z,t)}{\partial z^2}.\end{aligned} \tag{17}$$

Solving the partial differential equation (17) numerically requires very evolved schemes.

Since it has been experimentally observed that the major difficulties arise from the displacement of particles in the direction perpendicular to the wall (z), we will study a one-dimensional space-time Fokker-Planck equation, assuming a uniform distribution of particles in the in-plane direction. We obtain the following partial differential equation

$$\frac{\partial \mathcal{W}(z,t)}{\partial t} = D_\infty \frac{d\beta_\perp(z)}{dz}\frac{\partial \mathcal{W}(z,t)}{\partial z} + D_\infty \beta_\perp(z)\frac{\partial^2 \mathcal{W}(z,t)}{\partial z^2}, \tag{18}$$

where $\mathcal{W}(z,t)$ is the $z-$distribution function over time.

We remark that if the diffusion coefficient were constant (Stokes-Einstein D_∞, in the region away from the wall), the partial differential equation (18) reduces to the well-known heat equation $\frac{\partial \mathcal{W}(z,t)}{\partial t} = D_\infty \frac{\partial^2 \mathcal{W}(z,t)}{\partial z^2}$.

2.7 Dimensional Analysis

In order to determine relevant parameters, we perform a dimensional analysis on the model. We choose T the time elapsed between two window measurements and a the particle radius to be the characteristic time and length scales. Let $x = aX$, $y = aY$, $z = aZ$ and $t = T\tau$ define the dimensionless variables. The resulting dimensionless parameters are $\Pi_1 = \frac{u_\infty T}{a}$ and $\Pi_2 = \frac{D_\infty T}{a^2}$. They represent the dimensionless deterministic time and diffusive time. Using dimensionless units it is easy to plot (Fig. 4) the velocity profiles (11)-(13) and the diffusion tensor (9) obtained with the Bevan-Prieve relation for the experiments $a = 50$ nm, $H = 450$ nm, $\Theta = 300$ K and $\mu = 0.856$ kg/ms.

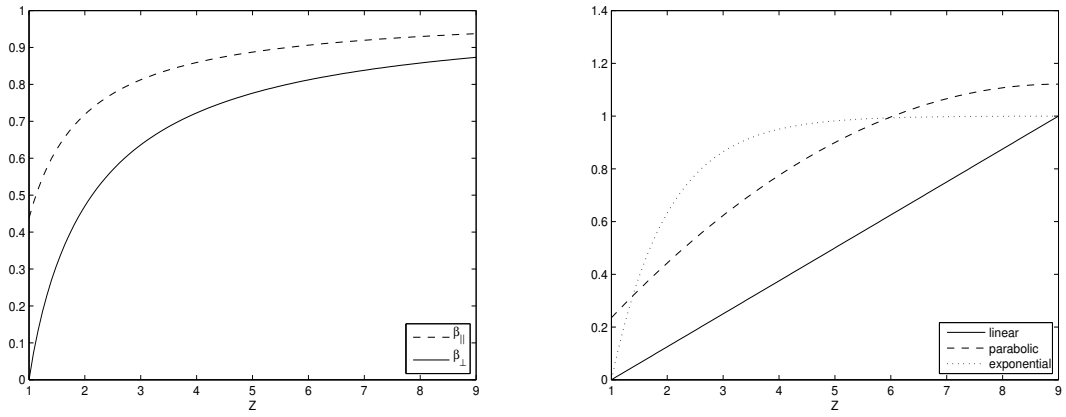

(a) Components of $\beta(aZ)$

(b) Velocity profiles $\gamma(aZ)$

Figure 4: (a) Dimensionless diffusion coefficient $\beta_\perp$ and $\beta_{||}$ as a function of the dimensionless position Z (b) Dimensionless linear (Couette), parabolic (Poiseuille), and exponentially decaying (electro-osmotic) profile γ as a function of the dimensionless position Z.

2.7.1 Dimensionless Langevin model

The dimensionless Langevin model (14)-(16) with $dW^i = \mathcal{N}(0,1), i = 1,\ldots,3$ becomes

$$dX = \Pi_1 \gamma(aZ)d\tau + \sqrt{2\Pi_2 \beta_{||}(aZ)d\tau}dW^1, \tag{19}$$

$$dY = \sqrt{2\Pi_2 \beta_{||}(aZ)d\tau}dW^2, \tag{20}$$

$$dZ = \Pi_2 \frac{d\beta_\perp(aZ)}{dZ}d\tau + \sqrt{2\Pi_2 \beta_\perp(aZ)d\tau}dW^3. \tag{21}$$

This is a system of stochastic differential equations of the form $d\mathbf{X} = \mathbf{a}(\mathbf{X})d\tau + \mathbf{b}(\mathbf{X})d\mathbf{W}$ with $\mathbf{W} = \mathcal{N}(0,1)$ and position dependent diagonal stochastic forcing $\mathbf{b}$ (see Chap. 3).

2.7.2 Dimensionless Fokker-Planck equation

The dimensionless one dimensional space-time Fokker-Planck equation (18) becomes

$$\frac{\partial \mathcal{W}(aZ,T\tau)}{\partial \tau} = \Pi_2 \frac{d\beta_\perp(aZ)}{dZ}\frac{\partial \mathcal{W}(aZ,T\tau)}{\partial Z} + \Pi_2 \beta_\perp(aZ)\frac{\partial^2 \mathcal{W}(aZ,T\tau)}{\partial Z^2}. \tag{22}$$

The above equation is an advection-diffusion equation or a diffusion equation with non-constant diffusivity, whose analytical solution is so far unknown.

CHAPTER III

NUMERICAL SIMULATION

The Langevin system of equations (19)-(21) is, because of the random forcing, stochastic. Before presenting general numerical simulations for such systems, we review basic and important facts from stochastic calculus. Finally, in section 3.3, we apply the theoretical considerations to our particular system.

3.1 Stochastic Calculus

Definition 3.1 (Scalar Brownian motion) *Let $(\Omega, \mathcal{A}, P)$ be a probability space and $[0,T]$ a time interval.*

1. *A stochastic process $X = \{X(t), t \in [0,T]\}$ is a collection of random variables on $(\Omega, \mathcal{A}, P)$ indexed by $t \in T$. We write X_t for $X(t)$.*

2. *A Gaussian process is a stochastic process whose joint distribution is Gaussian.*

3. *A standard Brownian motion $W = \{W_t, t \in [0,T]\}$ is a Gaussian process with independent increments satisfying*

$$W_0 = 0 \text{ with probability 1 } (w.p.1) \tag{23}$$

$$\mathbb{E}(W_t) = 0 \tag{24}$$

$$Var(W_t - W_s) = t - s. \tag{25}$$

Let W be a Brownian process and let $\{\mathcal{A}_t, t \geq 0\}$ be an increasing family of sub $\sigma-$algebras of $\mathcal{A}$ so that W_t is $\mathcal{A}_t-$measurable with $\mathbb{E}(W_t|\mathcal{A}_0) = 0$ and $\mathbb{E}(W_t - W_s|\mathcal{A}_s) = 0$ $w.p.1$ for all $0 \leq s \leq t$. Here $Y = \mathbb{E}(X|\mathcal{S})$ is the unique $\mathcal{S}-$measurable random variable with $\int_S Y dP = \int_S X dP$.

Definition 3.2 *For $0 < T < \infty$ we define $\mathcal{L}_T^2$ as the space of functions $f : [0,T] \times \Omega \to \mathbb{R}$ so that f is jointly $\mathcal{L} \times \mathcal{A}-$measurable ($\mathcal{L}$ Lebesgue $\sigma-$algebra), $\int_0^T \mathbb{E}(f(t,\cdot)^2)dt < \infty$,*

$\mathbb{E}(f(t,\cdot)^2) < \infty$ *for each* $0 \le t \le T$, *and* $f(t,\cdot)$ *is* $\mathcal{A}_t-$*measurable for each* $0 \le t \le T$. *We define a norm on* $\mathcal{L}_T^2$ *by* $||f||_{2,T}^2 = \int_0^T \mathbb{E}(f(t,\cdot)^2)dt$.

Identifying functions that are equal except on a set of measure zero, $(\mathcal{L}_T^2, ||\cdot||_{2,T})$ is a Banach space.

Definition 3.3 *A step function* $f \in \mathcal{L}_T^2$ *is defined by* $f(t,\omega) = f_j(\omega)$ *w.p.*1, *for a partition* $t_j \le t < t_{j+1}$ *and mean-square integrable* $\mathcal{A}_{t_j}-$*measurable random variables* f_j, $j = 1, \ldots, n$. *We denote by* $\mathcal{S}_T^2$ *the subset of all step functions in* $\mathcal{L}_T^2$.

Definition 3.4 (Ito integral) *We define the Ito stochastic integral in two steps.*

1. *Let* $f \in \mathcal{S}_T^2$. *The Ito stochastic integral for* f *over the interval* $[0,T]$ *is*

$$I(f)(\omega) = \sum_{j=1}^{n} f_j(\omega)(W_{t_j+1}(\omega) - W_{t_j}(\omega)) \quad w.p.1. \tag{26}$$

2. *Let* $f \in \mathcal{L}_T^2$. *Let* $f_n \in \mathcal{S}_T^2$ *so that* $f_n \to f$ *in* $(\mathcal{L}_T^2, ||\cdot||_{2,T})$. *The Ito stochastic integral of* f *is the mean-square limit of* $I(f_n)$ *with* $I(f_n)$ *given by* (26).

Remark

If $f \equiv 1$, then $I(f)(\omega) = W_T(\omega) - W_0(\omega) = W_T(\omega)$.

Definition 3.5 (Scalar stochastic differential) *Let* e *with* $\sqrt{|e|} \in \mathcal{L}_T^2$ *and* $f \in \mathcal{L}_T^2$. *A stochastic differential is an expression of the form*

$$dX_t(\omega) = e(t,\omega)dt + f(t,\omega)dW_t(\omega),$$

which is a symbolic way of writing

$$X_t(\omega) - X_s(\omega) = \int_s^t e(u,\omega)du + \int_s^t f(u,\omega)dW_u(\omega) \quad w.p.1 \quad \textit{for all } 0 \le s \le t \le T. \tag{27}$$

Let $U : [0,T] \times \mathbb{R} \to \mathbb{R}$ have continuous partial derivatives $\frac{\partial U}{\partial t}$, $\frac{\partial U}{\partial x}$, $\frac{\partial^2 U}{\partial x^2}$. Let X_t satisfy (27).

Theorem 3.1 (Ito formula) *Let* $Y_t = U(t, X_t)$ *for* $0 \le t \le T$. *Then*

$$Y_t - Y_s = \int_s^t \left(\frac{\partial U(u,X_u)}{\partial t} + e_u \frac{\partial U(u,X_u)}{\partial x} + \frac{1}{2} f_u^2 \frac{\partial^2 U(u,X_u)}{\partial x^2} \right) du + \int_s^t f_u \frac{\partial U(u,X_u)}{\partial x} dW_u, \tag{28}$$

*w.p.*1, *for any* $0 \le s \le t \le T$, *where* $e_u = e(u,\cdot)$ *and* $f_u = f(u,\cdot)$.

The proof (see [14]) is a consequence of the Taylor and Mean Value Theorems:

$$U(t+\Delta t, x+\Delta x) - U(t,x) = \frac{\partial U(t+\alpha\Delta t, x)}{\partial t}\Delta t + \frac{\partial U(t,x)}{\partial x}\Delta x + \frac{1}{2}\frac{\partial^2 U(t, x+\beta\Delta x)}{\partial x^2}(\Delta x)^2.$$

Definition 3.6 (Vector Brownian motion) *Let W^j, $j = 1, \ldots, m$ be scalar pairwise independent Brownian motions. Then $\mathbf{W} = \{\mathbf{W}_t = (W_t^1, W_t^2, \ldots, W_t^m), t \geq 0\}$ is an $m-$dimensional Brownian motion.*

Definition 3.7 (Vector stochastic differential) *A $d-$dimensional vector stochastic differential for an $m-$dimensional Brownian motion is a symbolic equation of the form*

$$d\mathbf{X}_t = \mathbf{e}_t dt + \mathbf{F}_t d\mathbf{W}_t$$

representing the vector stochastic integral expression

$$\mathbf{X}_t - \mathbf{X}_s = \int_s^t \mathbf{e}_u du + \int_s^t \mathbf{F}_u d\mathbf{W}_u \quad \textit{for any } 0 \leq s \leq t \leq T \tag{29}$$

or componentwise

$$X_t^k - X_s^k = \int_s^t e_u^k du + \sum_{j=1}^m \int_s^t F_u^{k,j} dW_u^j, \quad w.p.1, \quad k = 1, \ldots d. \tag{30}$$

Let $U : [0,T] \times \mathbb{R}^d \to \mathbb{R}$ have continuous partial derivatives $\frac{\partial U}{\partial t}$, $\frac{\partial U}{\partial x_k}$, $\frac{\partial^2 U}{\partial x_k \partial x_i}$, $i, k = 1, \ldots, d$ and let X_t satisfy (29). The analogue to the Ito formula (28) is given in the next theorem.

Theorem 3.2 *Let $Y_t = \{Y_t, 0 \leq t \leq T\}$ be defined as $Y_t = U(t, \mathbf{X}_t)$ w.p.1. Then the stochastic differential for Y_t is*

$$dY_t = \left(\frac{\partial U}{\partial t} + \sum_{k=1}^d e_t^k \frac{\partial U}{\partial x_k} + \frac{1}{2}\sum_{j=1}^m \sum_{i,k=1}^d F_t^{i,j} F_t^{k,j} \frac{\partial^2 U}{\partial x_i \partial x_k}\right) dt + \sum_{j=1}^m \sum_{i=1}^d F_t^{i,j} \frac{\partial U}{\partial x_i} dW_t^j. \tag{31}$$

Iterated applications of the Ito formula (28) and (31) leads to Ito-Taylor expansions, the analogue of the deterministic Taylor expansion.

We consider a $d-$dimensional Ito stochastic process satisfying

$$\mathbf{X}_t = \mathbf{X}_{t_0} + \int_{t_0}^t \mathbf{a}(X_s, s) ds + \sum_{j=1}^m \int_{t_0}^t \mathbf{b^j}(X_s, s) dW_s^j. \tag{32}$$

The random forcing $\mathbf{b}$ in (32) is called noise. We define for $j = 1, \ldots, m$ the operator $L^j = \sum_{k=1}^{d} b^{k,j} \frac{\partial}{\partial x^k}$. Let $I_{(j_1,\ldots,j_l)}$ denote the multiple Ito integrals

$$I_{(j_1,\ldots,j_l)} = \int_{t_0}^{t} \ldots \int_{t_0}^{s_2} dW_{s_1}^{j_1} dW_{s_2}^{j_2} \ldots dW_{s_l}^{j_l}.$$

The first non-trivial Ito-Taylor expansion for a multi-dimensional Ito process is

$$X_t^k = X_{t_0}^k + a^k(\mathbf{X}_{t_0}, t_0) \int_{t_0}^{t} ds + \sum_{j=1}^{m} b^{k,j}(\mathbf{X}_{t_0}, t_0) I_{(j)} + R^k \tag{33}$$

and the second one becomes

$$X_t^k = X_{t_0}^k + a^k(\mathbf{X}_{t_0}, t_0) \int_{t_0}^{t} ds + \sum_{j=1}^{m} b^{k,j}(\mathbf{X}_{t_0}, t_0) I_{(j)} + \sum_{j_1,j_2=1}^{m} L^{j_1} b^{k,j_2}(\mathbf{X}_{t_0}, t_0) I_{(j_1,j_2)} + \overline{R^k}, \tag{34}$$

where $\mathbf{R}$ and $\overline{\mathbf{R}}$ are remainder terms.

Theorem 3.3 *The following statements are true for multiple Ito integrals.*

1. $I_{(j)} = W_t^j - W_{t_0}^j$.
2. $I_{(j,j)} = \frac{1}{2}\Big((W_t^j - W_{t_0}^j)^2 - (t - t_0)\Big)$.

Proof

1. This follows from the definition of Ito integrals: $I_{(j)} = \int_{t_0}^{t} dW_s = W_t^j - W_{t_0}^j$.

2. By definition of $I_{(j_1,j_2)}$ and the first part of the theorem we have

$$\begin{aligned} I_{(j,j)} &= \int_{t_0}^{t} \int_{t_0}^{s_2} dW_{s_1}^j dW_{s_2}^j = \int_{t_0}^{t} (W_{s_2}^j - W_{t_0}^j) dW_{s_2}^j = \int_{t_0}^{t} W_{s_2}^j dW_{s_2}^j - W_{t_0}^j \int_{t_0}^{t} dW_{s_2}^j \\ &= \int_{t_0}^{t} W_{s_2}^j dW_{s_2}^j - W_{t_0}^j (W_t^j - W_{t_0}^j). \end{aligned}$$

   Let $X_t = W_t$ (i.e $e \equiv 0$, $f \equiv 1$) and $U(t,x) = x^2$. By Ito formula (28) we find for $Y_t = U(t, X_t)$

$$dY_t = d((W_t)^2) = dt + 2W_t dW_t,$$

   in other words

$$(W_t)^2 - (W_{t_0})^2 = \int_{t_0}^{t} ds + 2 \int_{t_0}^{t} W_s dW_s.$$

This implies that

$$\int_{t_0}^{t} W_t^j dW_t^j = \frac{1}{2}\bigg((W_t^j)^2 - (W_{t_0}^j)^2 - (t-t_0)\bigg).$$

Finally, we have

$$I_{(j,j)} = \frac{1}{2}\bigg((W_t^j)^2 + (W_{t_0}^j)^2 - (t-t_0) - 2W_{t_0}^j W_t^j\bigg) = \frac{1}{2}\bigg((W_t^j - W_{t_0}^j)^2 - (t-t_0)\bigg).$$

□

3.2 Numerical Approximation

Let $\Delta = \frac{T-t_0}{N}$ for a time discretization $t_0 < t_1 < \ldots < t_N = T$. Let $\Delta W_n^j = W_{t_{n+1}}^j - W_{t_n}^j$, $n = 0, \ldots, N-1$, $j = 0, \ldots, m$ for the $m-$dimensional Brownian motion $\mathbf{W} = \{(W_t^1, \ldots, W_t^m), t \geq 0\}$. From definition 3.1 we know that the ΔW^j increments are independent and $\Delta W^j = \mathcal{N}(0, \Delta)$ for $j = 1, \ldots, m$. Therefore we use a sequence of independent Gaussian numbers to generate ΔW^j, $j = 1, \ldots, m$ (see [9]).

We consider a $d-$dimensional stochastic process $\mathbf{X}_t$ satisfying (32). Let $\mathbf{Y}_n$ be a discrete stochastic process so that $\mathbf{Y}_n$ is an approximation of $\mathbf{X}_{t_n}$: $\mathbf{Y}_n \approx \mathbf{X}_{t_n}$.

Definition 3.8 (Strong order of convergence) *Y^k converges strongly with order Γ_1 to X^k if there exists a positive constant C_1, which does not depend on Δ and $\Delta_0 > 0$, with*

$$\mathbb{E}(|X_{t_n}^k - Y_n^k|) \leq C_1 \Delta^{\Gamma_1}$$

for any fixed $t \in [t_0, T]$ and $\Delta \in (0, \Delta_0)$.

Definition 3.9 (Weak order of convergence) *Y^k converges weakly with order Γ_2 to X^k, if there exists a positive constant C_2, which does not depend on Δ and $\Delta_0 > 0$, with*

$$|\mathbb{E}(X_{t_n}^k) - \mathbb{E}(Y_n^k)| \leq C_2 \Delta^{\Gamma_2}$$

for any fixed $t \in [t_0, T]$ and $\Delta \in (0, \Delta_0)$.

The first non-trivial Ito-Taylor expansion (33), containing only time and Ito integrals of multiplicity one, leads to the Euler-Maruyama approximation.

Definition 3.10 (Euler-Maruyama scheme) *For the d-dimensional stochastic process* (32)*, the kth component of the Euler-Maruyama scheme is given by*

$$Y_{n+1}^k = Y_n^k + a_n^k \Delta + \sum_{j=1}^{m} b_n^{k,j} \Delta W_n^j. \tag{35}$$

The following theorem about the orders of convergence of the Euler-Maruyama scheme is proved by Kloeden and Platen ([14]).

Theorem 3.4 *Assuming that* $\mathbf{a}$ *and* $\mathbf{b}$ *are four times continuously differentiable and satisfy Lipschitz and linear growth conditions, then the Euler-Maruyama scheme* (35) *has the order of strong convergence* $\Gamma_1 = \frac{1}{2}$ *and weak convergence* $\Gamma_2 = 1$*.*

Keeping the next order term in the Ito-Taylor expansion (34), we define the Milstein scheme.

Definition 3.11 (Milstein scheme) *For the d-dimensional stochastic process* (32)*, the kth component of the Milstein scheme is given by*

$$Y_{n+1}^k = Y_n^k + a_n^k \Delta + \sum_{j=1}^{m} b_n^{k,j} \Delta W_n^j + \sum_{j_1,j_2=1}^{m} L^{j_1} b^{k,j_2} I_{(j_1,j_2)}. \tag{36}$$

Kloeden and Platen ([14]) show that the next theorem holds.

Theorem 3.5 *Under the assumption that* $\mathbf{a} \in \mathcal{C}^{1,1}(\mathbb{R}^d \times \mathbb{R}^+)$ *and* $\mathbf{b} \in \mathcal{C}^{1,2}(\mathbb{R}^d \times \mathbb{R}^+)$*, the Milstein scheme* (36) *has strong order of convergence* $\Gamma_1 = 1$ *and weak order of convergence* $\Gamma_2 = 1$*.*

Definition 3.12 (Diagonal noise) *A noise* $\mathbf{b}$ *is diagonal, when* $d = m$ *and each component* X^k *of the Ito process* $\mathbf{X}$ *is distributed only by the corresponding component* W^k *of the Brownian motion* $\mathbf{W}$ *and the diagonal diffusion coefficient* $b^{k,k}$ *depends only on* x^k*, that is*

$$b^{k,j}(x,t) = 0 \quad \textit{and} \quad \frac{\partial b^{j,j}(x,t)}{\partial x^k} = 0.$$

Claim 3.1 (Milstein scheme for diagonal noise) *The Milstein scheme* (36) *for a diagonal noise reduces to*

$$Y_{n+1}^k = Y_n^k + a_n^k \Delta + b_n^{k,k} \Delta W_n^k + \frac{1}{2} b_n^{k,k} \frac{\partial b_n^{k,k}}{\partial x^k} \Big((\Delta W_n^k)^2 - \Delta \Big). \tag{37}$$

This is a simple consequence of the definition of a diagonal noise and of the second part of theorem 3.3 for double Ito integrals.

In the case of a non-diagonal noise, the implementation of the Milstein scheme requires the evaluation of double Ito integrals $I_{(j_1,j_2)}$ for $j_1 \neq j_2$. Because there are no simplifications analogous to theorem 3.3 for $I_{(j_1,j_2)}$, $j_1 \neq j_2$, we consider the system of Ito stochastic differential equations (see [13])

$$\begin{cases} dX_t = Y_t dW_t^{j_2} \quad X_{t_0} = 0 \\ dY_t = dW_t^{j_1} \quad Y_{t_0} = 0 \end{cases} . \tag{38}$$

Integrating the system we have

$$Y_t = \int_{t_0}^{t} dW_s^{j_1} \quad \text{and} \quad dX_t = \left(\int_{t_0}^{t} dW_s^{j_1} \right) dW^{j_2}. \tag{39}$$

The last equation is equivalent to

$$X_t = \int_{t_0}^{t} \int_{t_0}^{s_2} dW_{s_1}^{j_1} dW_{s_2}^{j_2} = I_{(j_1,j_2)}. \tag{40}$$

Therefore a double Ito stochastic integral $I_{(j_1,j_2)}$ with $j_1 \neq j_2$ is numerically approximated via an Euler-Maruyama scheme as the solution of the stochastic differential system (38). If the time step Δ is small enough in the approximation of $I_{(j_1,j_2)}$, then the Milstein scheme remains of strong order of convergence $\Gamma_1 = 1$.

3.3 Dimensionless Langevin Simulation

We apply a discretized numerical scheme to the dimensionless Langevin equations (19)-(21). We have, in the description of the stochastic differential equation (32), $d = m = 3$ and

$$\mathbf{X}_\tau = \begin{pmatrix} X \\ Y \\ Z \end{pmatrix}, \mathbf{a} = \begin{pmatrix} \Pi_1 \gamma(aZ) \\ 0 \\ \Pi_2 \frac{d\beta_\perp(aZ)}{dZ} \end{pmatrix}, \mathbf{b} = \begin{bmatrix} \sqrt{2\Pi_2 \beta_{||}(aZ)} & 0 & 0 \\ 0 & \sqrt{2\Pi_2 \beta_{||}(aZ)} & 0 \\ 0 & 0 & \sqrt{2\Pi_2 \beta_\perp(aZ)} \end{bmatrix},$$

for $\tau \in [0,1]$ and $Z \in [1, H/a]$. The stochastic differential is therefore

$$d\mathbf{X}_\tau = \mathbf{a}(\mathbf{X}_\tau) d\tau + \mathbf{b}(\mathbf{X}_\tau) d\mathbf{W}_\tau, \tag{41}$$

with $\mathbf{W}_\tau$ a 3-dimensional Brownian motion with independent increments. We emphasize that, while $\mathbf{b}$ is a diagonal tensor, the recurring Z dependence violates the definition of diagonal noise.

Let $\Delta\tau = \frac{1}{N}$ be the time step discretization. Let ΔW^k, $k = 1, \ldots, 3$ be independent $\mathcal{N}(0, \Delta\tau)$-distributed increments. Initially the particles ($a = 50$ nm) are uniformly distributed in the channel of dimensions: $H = 450$ nm, $H_x = 2500$ nm, and $H_y = 5000$ nm. We study both the Euler-Maruyama scheme (35) and the Milstein sheme (36) for the simulation of particles displacements obeying the stochastic differential equation (41).

3.3.1 Euler-Maruyama scheme

The Euler-Maruyama scheme for the Langevin stochastic differential equation (41) becomes

$$X_{n+1} = X_n + \Pi_1\gamma(aZ_n)\Delta\tau + \sqrt{2\Pi_2\beta_{||}(aZ_n)}\Delta W_n^1 \tag{42}$$

$$Y_{n+1} = Y_n + \sqrt{2\Pi_2\beta_{||}(aZ_n)}\Delta W_n^2 \tag{43}$$

$$Z_{n+1} = Z_n + \Pi_2\frac{d\beta_\perp(aZ)}{dZ}\bigg|_{Z=Z_n}\Delta\tau + \sqrt{2\Pi_2\beta_\perp(aZ_n)}\Delta W_n^3. \tag{44}$$

We expect the strong order of convergence of the scheme (42)-(44) to be $\Gamma_1 = 1/2$ and the weak order of convergence to be $\Gamma_2 = 1$ (Thm. 3.4).

In the next figure (Fig. 5) we logarithmically plot each component of the strong error at $\tau = 1$: $\mathbb{E}(|X(1) - X_N|)$, $\mathbb{E}(|Y(1) - Y_N|)$ and $\mathbb{E}(|Z(1) - Z_N|)$ as a function of $\Delta\tau$. Because there is no particle-particle interaction, the sample mean is taken over 2^9 particles. Since the exact solution $\mathbf{X}(1)$ is unknown, we use $\mathbf{X}_N$ with the smallest $\Delta\tau = 2^{-16}$ as the best approximation for $\mathbf{X}(1)$ (see [9]). We choose $\Pi_1 = 3$ and $\Pi_2 = 4$ corresponding to 50 nm particles in water at room temperature with $u_\infty = 0.1$ mm/s and γ to be on the left the linear profile (Eq. (11)) and on the right the parabolic profile (Eq. (12)). Both plots in figure 5 show that the Euler-Maruyama scheme for the Langevin system ((42)-(44)) has strong order of convergence $\Gamma_1 = 1/2$ and that generating the data with $N = 2^{12}$

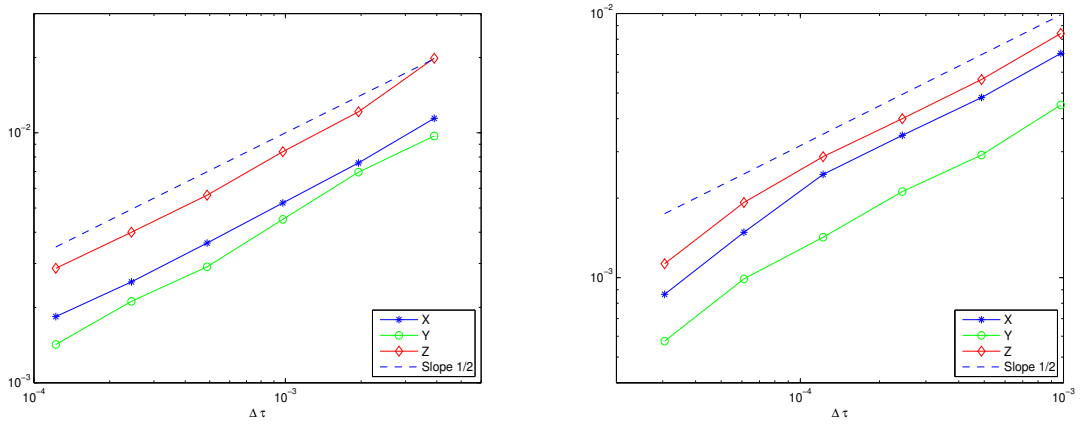

(a) Linear profile

(b) Parabolic profile

Figure 5: Log-Log strong convergence of the X-, Y- and Z-components of the Euler-Maruyama simulation of the dimensionless Langevin system at $\tau = 1$ as a function of $\Delta\tau$ compared to a line of slope 0.5.

($\Delta\tau = 2^{-12} = 2.33 \cdot 10^{-4}$) will guarantee a reasonable accuracy. The same result holds for the exponentially decaying profile (Eq. (13)).

Next we look at the weak convergence of the Euler-Maruyama scheme for the Langevin system (42)-(44). In figure 6, we logarithmically plot each component of the weak error at $\tau = 1$: $|\mathbb{E}(X(1)) - \mathbb{E}(X_N)|$, $|\mathbb{E}(Y(1)) - \mathbb{E}(Y_N)|$ and $|\mathbb{E}(Z(1)) - \mathbb{E}(Z_N)|$ as a function of $\Delta\tau$. Again the sample mean is over 2^9 particles, the approximate solution at $\tau = 1$ with the smallest $\Delta\tau$ is used for the exact solution $\mathbf{X}(1)$ and the parameters are $\Pi_1 = 3$ and $\Pi_2 = 4$. We find that the weak convergence is harder to check especially in the Y-direction. The oscillations come from the variation in the variance of the Brownian increments generated with *randn* in Matlab and are therefore inevitable. Because in the X- and Z-direction the weak error decays with a slope of 1 and the strong convergence order is 1/2, we set $N = 2^{12}$ or $N = 2^{14}$ in the generation of the particles displacement with an Euler-Maruayama scheme.

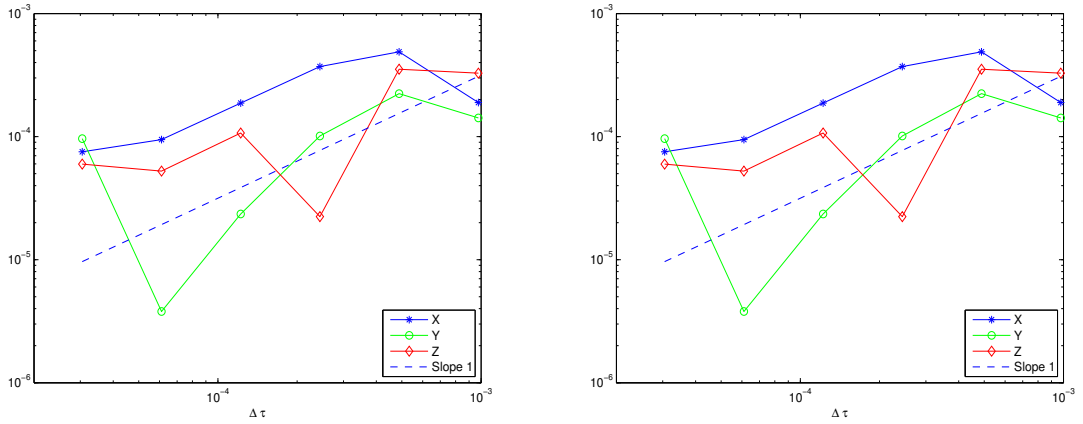

(a) Linear profile

(b) Parabolic profile

Figure 6: Log-Log weak convergence of the X-, Y- and Z-components of the Euler-Maruyama simulation of the dimensionless Langevin system at $\tau = 1$ as a function of $\Delta\tau$ compared to a line of slope 1.

3.3.2 Milstein scheme

Because we will develop a probabilistic method to reconstruct the velocity profile, we want the simulation to have a higher order of convergence, in order to properly address (see Chap. 4-6) the validity of the developed reconstruction algorithm.

The noise **b** is not a diagonal noise, even if it is a diagonal matrix. Therefore the implementation of the Milstein scheme requires the simulation of $I_{(3,1)}$ and $I_{(3,2)}$ through the system of stochastic differential equations (38). The Milstein scheme (36) for a non-diagonal noise with diagonal entries becomes

$$Y_{n+1}^k = Y_n^k + a_n^k \Delta t + b_n^{k,k} \Delta W_n^k + \sum_{j_1=1}^{3} L^{j_1} b^{k,j_1} I_{(j_1,k)} \tag{45}$$

$$= Y_n^k + a_n^k \Delta t + b_n^{k,k} \Delta W_n^k + b^{3,3} \frac{\partial b^{k,k}}{\partial Z} I_{(3,k)}. \tag{46}$$

With the definitions of **a**, **b** and theorem 3.3 we find for the Langevin stochastic differential

equation (41)

$$X_{n+1} = X_n + \Pi_1 \gamma(aZ_n)\Delta\tau + \sqrt{2\Pi_2 \beta_\perp(aZ_n)}\Delta W_n^1 + \Pi_2 \sqrt{\frac{\beta_\perp(aZ_n)}{\beta_{||}(aZ_n)}} \frac{d\beta_{||}(aZ)}{dZ}\bigg|_{Z=Zn} I_{(3,1)} \tag{47}$$

$$Y_{n+1} = Y_n + \sqrt{2\Pi_2 \beta_\perp(aZ_n)}\Delta W_n^2 + \Pi_2 \sqrt{\frac{\beta_\perp(aZ_n)}{\beta_{||}(aZ_n)}} \frac{d\beta_{||}(aZ)}{dZ}\bigg|_{Z=Zn} I_{(3,2)} \tag{48}$$

$$Z_{n+1} = Z_n + \Pi_2 \frac{d\beta_\perp(aZ)}{dZ}\bigg|_{Z=Z_n} \Delta\tau + \sqrt{2\Pi_2 \beta_\perp(aZ_n)}\Delta W_n^3 + \frac{\Pi_2}{2}\frac{d\beta_\perp(aZ)}{dZ}\bigg|_{Z=Z_n} ((\Delta W_n^3)^2 - \Delta\tau). \tag{49}$$

Here $I_{(3,1)}$ and $I_{(3,2)}$ are obtained as solutions of the system of stochastic differential equations (38) approximated with an Euler-Maruyama scheme with 2^6 steps. The purpose of the Milstein scheme is to achieve a strong order of convergence $\Gamma_1 = 1$ and to keep the weak order of convergence $\Gamma_2 = 1$ (see Thm. 3.5).

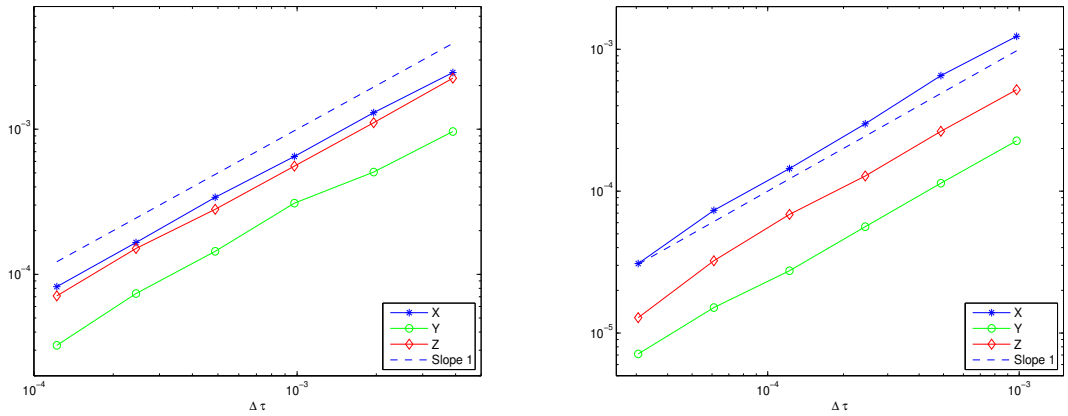

(a) Linear Profile

(b) Parabolic Profile

Figure 7: Log-Log strong convergence of the X-, Y- and Z-components of the Milstein simulation of the dimensionless Langevin system at $\tau = 1$ as a function of $\Delta\tau$ compared to a line of slope 1.

In figure 7, we logarithmically plot each component of the strong error over 2^9 particles at $\tau = 1$ as a function of $\Delta\tau$ for the linear (Fig. 7(a)) and parabolic profile (Fig. 7(b)) at $\Pi_1 = 3$ and $\Pi_2 = 4$. We set the number of time steps in the Euler-Maruyama simulation of

$I_{(3,1)}$ and $I_{(3,2)}$ to $\frac{\Delta\tau}{2^6}$. We find for each of the components the expected linear decay. We conclude that it is enough to set $N = \{2^{10}, 2^{12}, 2^{14}\}$ in the generation of data.

Finally, we logarithmically plot each component of the weak error at $\tau = 1$ with the same parameters to check that the weak order of convergence of the scheme (47)-(49) is $\Gamma_2 = 1$. In the case of the Milstein scheme, the oscillations due to the variance of the Brownian

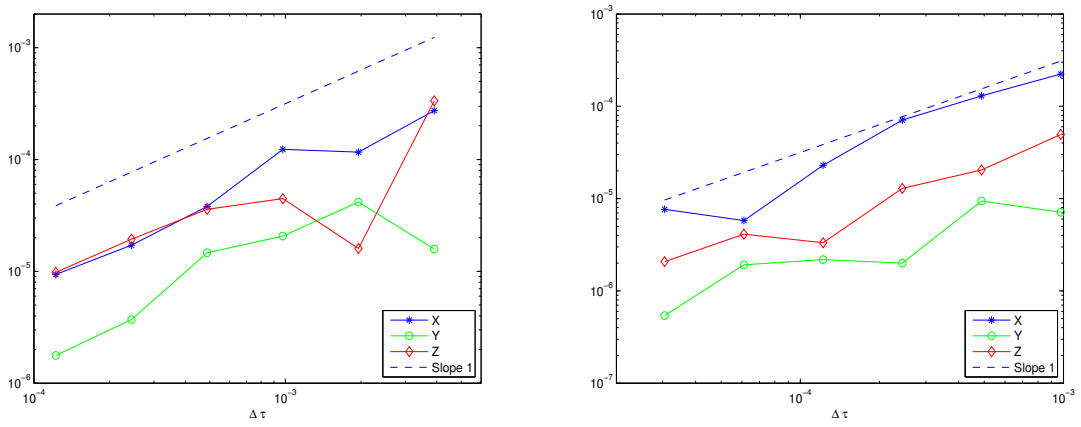

(a) Linear Profile

(b) Parabolic Profile

Figure 8: Log-Log weak convergence of the X-, Y- and Z-components of the Milstein simulation of the dimensionless Langevin system at $\tau = 1$ as a function of $\Delta\tau$ compared to a line of slope 1.

increments (in comparison with figure 6) diminish and we demonstrate the linear decay of the weak error.

3.3.3 Flow simulation

Having established that the Milstein scheme (47)-(49) with $N = 2^{12}$ has the desired order of strong convergence ($\Gamma_1 = 1$) we are now able to simulate the effect of a flow in a microchannel, including the near-wall region.

Experimentally, particles are confined to the channel. The size of the channel and the particle density are chosen to match the experiments of Sadr *et al.* ([29], [38]). We set: $a = 50$

nm, $H = 450$ nm, $H_x = 2500$ nm, $H_y = 5000$ nm and $n = 64$.

The no-flux boundary condition at $Z = 1$ is a consequence of the fact that $\beta_\perp(aZ)$ is zero at $Z = 1$. However, in the numerical simulation a negative Brownian increment ΔW_n^k may cause the particle to cross the wall. To avoid this situation, we impose an artificial boundary condition at the wall in the form of a perfectly elastic reflection. We remark that it is enough for $\Delta\tau$ to be smaller than 2^{-8} for the number of particles that have to be reflected at the wall to be zero in practice.

The upper wall at $Z = H/a$ does not influence any of the experimental measurements, but to make sure that particles stay in the channel we impose numerically an elastic boundary condition at $Z = H/a$. The dimensions of the channel in the plane parallel to the wall are big compared to the channel height H. Therefore we set periodic boundary conditions on the X- and Y-displacements.

Images of particle flow are taken with a lag time T ($T = 2^{-9}$ s). In the dimensionless numerical description, the location of the particles position at $\tau = 1$, corresponding to T, is found through a Milstein scheme with 2^{12} time steps. Therefore multiple consecutive images are obtained by repeating the simulation (see Fig. 3). To generate and save three particle positions for 2^{16} windows with 2^{12} Milstein steps takes on a dual 2GHz AMD Athlon with 2GB RAM 10 to 14 days. The size of each of the resulting binary position file is 256M.

CHAPTER IV

VELOCITY PROFILE RECONSTRUCTION WITH PERFECT PARTICLE IDENTIFICATION

The goal is to reconstruct the dependence of the in-plane velocity profile from the distance normal to the wall, Z, without using any information about the location of the particle (for example, through the brightness of particle images). The assumptions leading to the statistical reconstruction concerns the distribution of the particles between two window measurements. Because we have chosen to focus on the deterministic part of the displacement, we assume that the diffusion tensor is known as $D_\infty\beta(aZ)$, where β is given by (9) and D_∞ is the Stokes-Einstein relation. For simplicity, we assume that the computation and observation domain are the same, thereby eliminating errors due to particle drop-in/out. We first consider the ideal case where the displacement of each particle is known.

The general idea is to reformulate the problem as a maximum likelihood estimate where the unknown velocity profile is the one that makes the observed data most likely. Therefore, we first describe the statistical assumptions in terms of the probability density function of a displacement. Then, we derive an algorithm to reconstruct the velocity profile for the perfect particle identification case followed by a discussion of basic examples. The main result together with error estimates is presented in chapter 5, when we replace perfect particle identification with exact mean displacement between two windows.

4.1 Probability Density Functions

We recall that X and Y are the in-plane dimensionless position of the particle, $Z \in [1, H/a]$ is the out-plane dimensionless position, Π_1 is the dimensionless deterministic time and Π_2 is the dimensionless diffusive time.

Definition 4.1 *Let f_Z be the probability density function of the Z-position. Let $f_{\Delta X}$ be the probability density function of the X-position. Let $f_{\Delta X \Delta Y}$ be the joint probability density function of a pair displacement $(\Delta X, \Delta Y)$. Let f be the joint probability density function of N displacement pairs.*

We know from the experimental setting that the X-displacement depends on the Z-position through the diffusion coefficient and the velocity profile and that the Y-displacement depends on the Z-position through the diffusion coefficient only (we assume unidirectional flow). Therefore we define the following probability density functions.

Definition 4.2 *Let $f_{\Delta X|Z}$ and $f_{\Delta Y|Z}$ be the probability density function of a displacement ΔX given Z and a displacement ΔY given Z, respectively. Let $f_{\Delta X \Delta Y|Z}$ be the joint probability density function of a pair displacement $(\Delta X, \Delta Y)$ given Z.*

Claim 4.1 *Assuming independence between both in-plane displacements and consecutive displacements, we find*

$$f_{\Delta X \Delta Y|Z} = f_{\Delta X|Z} f_{\Delta Y|Z} \tag{50}$$

$$f_{\Delta X \Delta Y} = \int f_{\Delta X \Delta Y|Z} f_Z dZ \tag{51}$$

$$f_{\Delta X} = \int f_{\Delta X|Z} f_Z dZ \tag{52}$$

$$f = \prod_{i=1}^{N} f_{\Delta X \Delta Y}. \tag{53}$$

In other words, the probability density function of a series of N displacements is given by

$$f = \prod_{i=1}^{N} \int f_{\Delta X|Z} f_{\Delta Y|Z} f_Z dZ. \tag{54}$$

Remark

The second assumption about independence between two displacements is incorrect, since consecutive $(\Delta X, \Delta Y)$ displacements are correlated by the continuity-in-time of the particles Z positions. This effect being small, equation (54) is valid.

Next we make a modeling assumption.

Assumption 4.1 *The dimensionless displacement between two consecutive windows can be approximated by an Euler step of the form*

$$\Delta X \approx \Pi_1 \gamma(aZ) + \sqrt{2\Pi_2 \beta_{||}(aZ)} dW^1 \tag{55}$$

$$\Delta Y \approx \sqrt{2\Pi_2 \beta_{||}(aZ)} dW^2 \tag{56}$$

where γ is the velocity profile given by (11)-(12)*, β is the diffusion coefficient* (9) *and dW^1, dW^2 are $\mathcal{N}(0,1)-$distributed.*

In other words, the X- and Y-displacements are normally distributed with respective means $\Pi_1\gamma(aZ)$ and 0 and variance $2\Pi_2\beta_{||}(aZ)$. Thus, we have an explicit formula for the probability density functions $f_{\Delta X|Z}$ and $f_{\Delta Y|Z}$

$$f_{\Delta X|Z}(\Delta X, Z) = \frac{1}{2\sqrt{\pi\Pi_2\beta_{||}(aZ)}} e^{\frac{-(\Delta X - \Pi_1\gamma(aZ))^2}{4\Pi_2\beta_{||}(aZ)}} \tag{57}$$

$$f_{\Delta Y|Z}(\Delta Y, Z) = \frac{1}{2\sqrt{\pi\Pi_2\beta_{||}(aZ)}} e^{\frac{-\Delta Y^2}{4\Pi_2\beta_{||}(aZ)}}. \tag{58}$$

Because we restrict ourselves to the case where the computation and observation domain are the same, we make the following assumption about the Z distribution.

Assumption 4.2 *The Z-positions are uniformly distributed in the region of interest, i.e*

$$f_Z = \frac{a}{H-a}\chi_{[1,H/a]}(Z). \tag{59}$$

Therefore we have for the probability density function $f_{\Delta X}$ and for the joint probability density function $f_{\Delta X \Delta Y}$ with claim 4.1, assumption 4.2 and equations (57)-(58)

$$f_{\Delta X} = \frac{a}{2\sqrt{\pi\Pi_2}(H-a)} \int_1^{\frac{H}{a}} \frac{1}{\sqrt{\beta_{||}(aZ)}} e^{-\frac{(\Delta X - \Pi_1\gamma(aZ))^2}{4\Pi_2\beta_{||}(aZ)}} dZ \tag{60}$$

$$f_{\Delta X \Delta Y} = \frac{a}{4\pi\Pi_2(H-a)} \int_1^{\frac{H}{a}} \frac{1}{\beta_{||}(aZ)} e^{-\frac{(\Delta X - \Pi_1\gamma(aZ))^2}{4\Pi_2\beta_{||}(aZ)}} e^{-\frac{\Delta Y^2}{4\Pi_2\beta_{||}(aZ)}} dZ. \tag{61}$$

Figures 9 are Maple plots of the joint probability density function $f_{\Delta X \Delta Y}$ for the linear (Eq. (11)) and parabolic (Eq. (12)) profile with $\Pi_1 = 3$ and $\Pi_2 = 4$ corresponding to

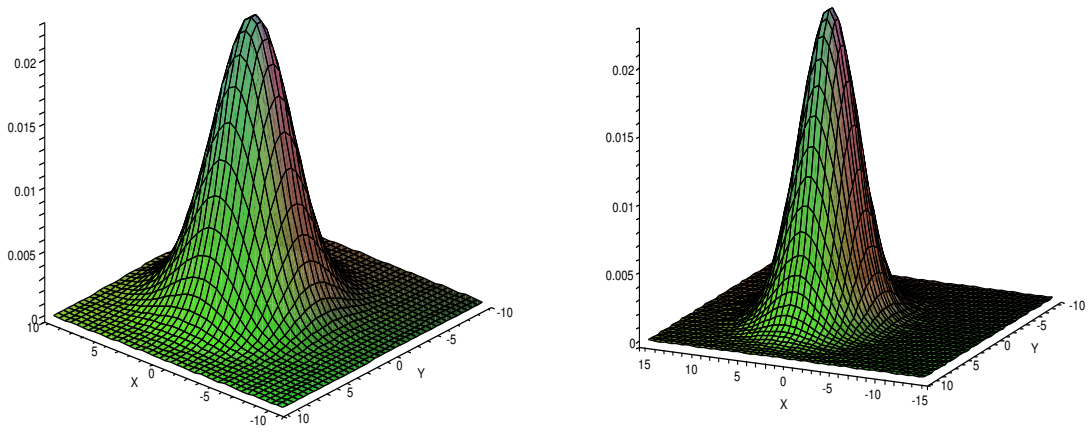

(a) Linear profile

(b) Parabolic profile

Figure 9: Joint probability density function $f_{\Delta X \Delta Y}$ for the linear and parabolic profile with $\Pi_1 = 3$ and $\Pi_2 = 4$.

experimental values. Even though the two dimensional joint probability density function is the integral of the product of two Gaussian distributions the shape remains similar to a Gaussian distribution. We note the slight difference in the height and width of the peak between the two velocity profiles (similarly for the exponentially decaying profile) signaling that a statistical reconstruction will be extremely sensitive.

This is reinforced by the next plot (Fig. 10) which is a normal plot of 2^{18} X-displacements for 64 particles for the linear profile with $\Pi_1 = 3$ and Π_2=4. It shows the deviance of the X-displacements from a true normal distribution. Thus, we conclude that even if the differences between an integrated Gaussian and a simple Gaussian are minimal, equation (55) is valid.

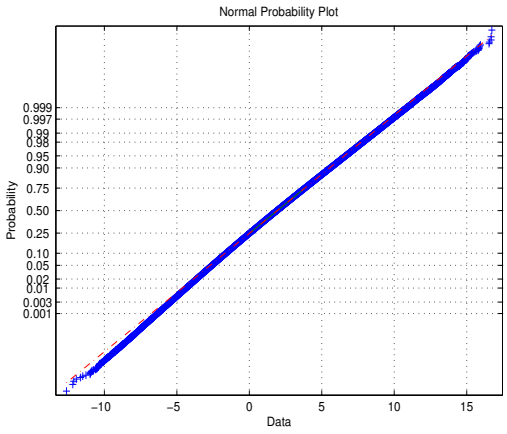

Figure 10: Normal probability plot of the X-displacements for the linear profile with $\Pi_1 = 3$, $\Pi_2 = 4$, $n = 64$ and $N = 2^{18}$.

4.2 Maximum Likelihood Estimate

Using N displacement pairs of n particles, we want to reconstruct $\gamma(aZ)$ through the probability density functions (61) and (54).

Given Nn measured displacement pairs $(\Delta X_i, \Delta Y_i)$, $i = 1, \ldots, Nn$, Π_1, Π_2 and $\beta_{||}(aZ)$, the maximum likelihood estimate of $\gamma(aZ)$ is the value of $\gamma(aZ)$ that makes the observed displacements most likely. Led by the independence assumption, we define the function

$$\phi(\{u_j\}_{j=1}^{M}) = -\sum_{i=1}^{Nn} \ln f_{\Delta X \Delta Y}(\Delta X_i, \Delta Y_i), \tag{62}$$

where M is the number of points Z at which we estimate γ, i.e $\gamma_j = \gamma(aZ_j)$, $j = 1, \ldots, M$. The most likely values for γ_j, $j = 1, \ldots, M$, are obtained by minimizing ϕ.

The statistical reconstruction problem has thus been reduced to two numerical algorithms. First, we evaluate the probability density function $f_{\Delta X \Delta Y}$ in (61) computing the integral with Gauss-Legendre quadrature for given γ_j values at the collocation points Z_j, $j = 1, \ldots, M$. We subsequently minimize the function ϕ with a direct simplex algorithm penalizing solutions that do not produce an increasing sequence, since we know that all three velocity profiles are increasing to the bulk velocity away from the wall. Both algorithms are presented next.

4.2.1 Numerical integration

We use Gauss-Legendre collocation points and Gauss quadrature (see [33]) to evaluate the integral over $Z \in [1, H/a]$.

Let I_i denote the numerical integration of $\int_1^{\frac{H}{a}} f_{\Delta X|Z}(\Delta X_i, Z) f_{\Delta Y|Z}(\Delta Y_i, Z) dZ$ for a given set of values γ_j, $j = 1, \ldots, M$ and a displacement pair $(\Delta X_i, \Delta Y_i)$. Let $f^i_{\Delta X \Delta Y}$ denote the numerical approximation of $f_{\Delta X \Delta Y}(\Delta X_i, \Delta Y_i)$. Then

$$f^i_{\Delta X \Delta Y} = \frac{a I_i}{H - a}$$

as in equation (61).

Algorithm 4.1 Numerical approximation of $f_{\Delta X \Delta Y}(\Delta X_i, \Delta Y_i)$

- Given: $\beta_{||}(aZ)$, Π_1 and Π_2
- Input: $(\Delta X_i, \Delta Y_i)$ and γ_j, $j = 1, \ldots, M$
- Define M Gauss-Legendre points s_j and weights w_j on $[-1, 1]$, $j = 1, \ldots, M$ ([33])
- Transform the points $Z_j \in [1, H/a]$ to s_j with $Z_j = 1 + \frac{s_j + 1}{2}(\frac{H}{a} - 1)$, $j = 1, \ldots, M$
- Evaluate with Gauss quadrature $I_i = \frac{H-a}{2a} \sum_{j=1}^{M} w_j f_{\Delta X|Z}(\Delta X_i, Z_j) f_{\Delta Y|Z}(\Delta Y_i, Z_j)$ with $f_{\Delta X|Z}$ and $f_{\Delta Y|Z}$ given by (55) and (56)
- Probability distribution function $f^i_{\Delta X \Delta Y} = \frac{a I_i}{H-a}$
- Output: $f^i_{\Delta X \Delta Y}$

4.2.2 Minimization with perfect particle identification

With Φ denoting the numerical approximation of ϕ the Matlab minimization using the build-in Matlab function *fminsearch* for a data set $(\Delta X_i, \Delta Y_i)$, $i = 1, \ldots, Nn$ follows, assuming that an initial guess $\gamma_{0,j}$, $j = 1, \ldots, M$ can be found. Non-increasing solutions are penalized by adding to the function a multiple (usually 10^3) of the sum of the squares of the negative

increments.

Algorithm 4.2 Minimization with perfect particle identification

- Given: $\beta_{||}(aZ)$, Π_1 and Π_2
- Input: $(\Delta X_i, \Delta Y_i)$, $i = 1, \ldots, Nn$
- Initial guess: $\gamma_{0,j}$, $j = 1, \ldots, M$
- Compute the numerical probability density function $f^i_{\Delta X \Delta Y}$ with algorithm 4.1
- Function to be minimized: $\Phi(\{\gamma_j\}_{j=1}^M) = -\sum_{i=1}^{Nn} \ln f^i_{\Delta X \Delta Y}$
- Penalty: Add to Φ a multiple of the sum of the squares of the negative increments
- Minimization using *fminsearch*, a simplex direct search method
- Output: γ_j, $j = 1, \ldots, M$

4.3 Results

Because the goal is to improve from perfect particle identification to exact mean, the discussion of the results is not as thorough as the one presented below in chapter 5. In particular, there is no discussion of error, and we limit ourselves to the illustration of the validity of a statistical reconstruction. We consider the linear profile (11) and the parabolic profile (12) with $\Pi_1 = 3$, $\Pi_2 = 4$, $n = 64$ and $N = 2^{18}$.

Including both the X- and Y-displacements for each particles, we have to process, at every function evaluation of Φ, 2^{25} data. Because of RAM memory limitation, we divide the X and Y data set into $B = 128$ blocks each of size 2^{17}. Let $\overline{\gamma_j}$, $j = 1, \ldots, M$ denote the mean of the approximated γ over the 128 blocks. In other words,

$$\overline{\gamma_j} = \frac{1}{B} \sum_{k=1}^{B} \gamma_j^k, \; j = 1, \ldots, M.$$

Figure 11 illustrates the statistical reconstruction in the case of the linear profile with $M = 3$ and $M = 5$. Note that because of the symmetry of Gauss-Legendre collocation points, we limit ourselves to odd numbers M. In both cases (Fig. 11), we plot the mean of the block

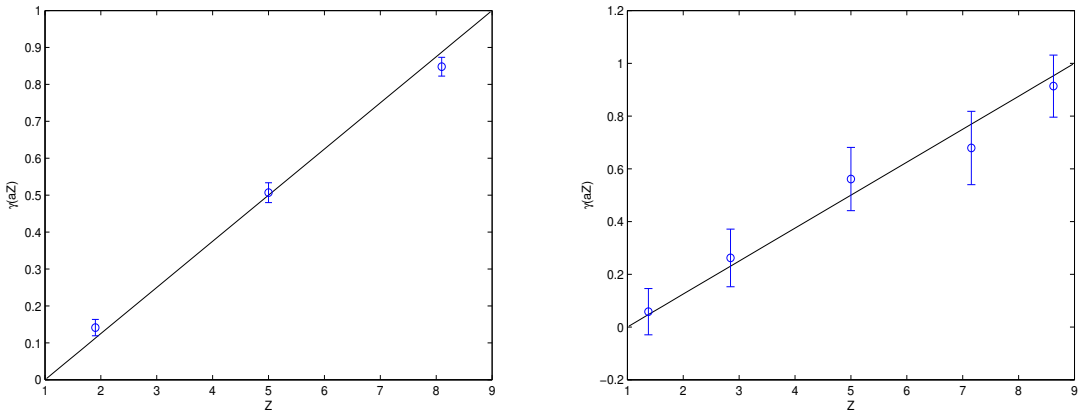

(a) $M = 3$ (b) $M = 5$

Figure 11: Perfect particle identification: Errorbar reconstruction for the linear profile with $B = 128$, 90% confidence interval for $M = 3$ and $M = 5$.

reconstructed values $\overline{\gamma_j}$, $j = 1, \ldots, M$ as well as the standard deviation, represented as 90% confidence interval together with the true linear profile. We see that with $M = 3$ (Fig. 11(a)) there is not much variation in γ_j^k, $k = 1, \ldots, B$ for each points Z_j, $j = 1, \ldots, B$, while the errorbars are more significant on a $M = 5$ (Fig. 11(b)) reconstruction. Thus, it follows that the standard deviation among different averaged block recontructed profiles is determined by the size of the given data. The more discrete points M, the bigger each set of data should be to reduce discrepancy. We remark that the approximation for $\gamma(aZ_j)$ through the mean over the blocks $\overline{\gamma_j}$, $j = 1, \ldots, M$ is equivalently good for both cases.

Next, we apply the same reconstruction with mean over blocks to the parabolic profile (Fig. 12) with $M = 3$ and $M = 5$. Again $\overline{\gamma_j}$, $j = 1, \ldots, M$ is plotted together with the standard deviation in the form of 90% confidence interval and the true profile. The results are similar to the linear case with bigger errorbar with $M = 5$ (Fig. 12(b)) than with $M = 3$ (Fig. 12(a)) and equally good approximation of $\gamma(aZ_j)$ through $\overline{\gamma_j}$, $j = 1, \ldots, M$.

From figures 11 and 12, we conclude that it is possible to statistically reconstruct the velocity profile based on the probability density function of the X- and Y-displacements provided

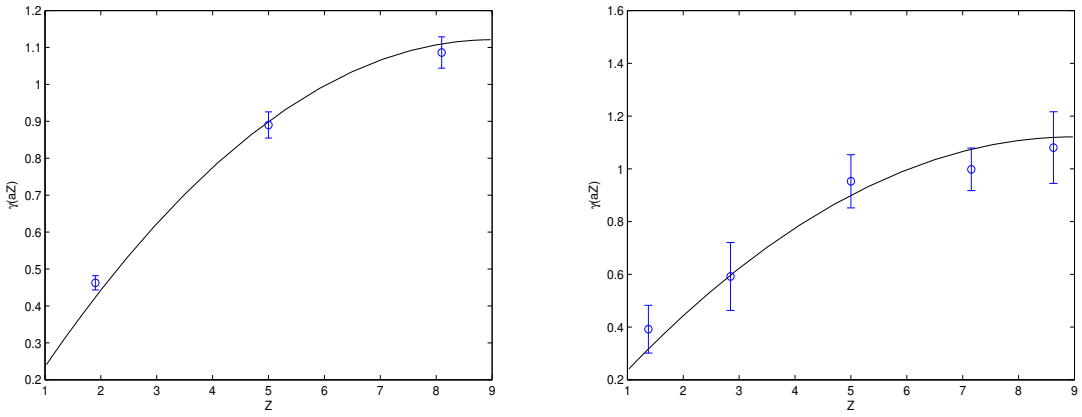

(a) $M = 3$ (b) $M = 5$

Figure 12: Perfect particle identification: Errorbar reconstruction for the parabolic profile with $B = 128$, 90% confidence interval for $M = 3$ and $M = 5$.

that we know the exact displacement of each particle. In the next chapter (Chap. 5), we discuss what modifications have to be incorporated in order to extend the reconstruction to exact mean displacements of n particles.

We remark that the developed algorithm corresponds to an experimental particle tracking problem.

4.4 Computational Cost

As an indication for the computational resources needed in the reconstruction, we list in table 1 the time required by the four examples presented in figures 11 and 12.

Each node of the cluster is a dual 2 GHz AMD Athlon processor with 2 GB RAM. The main problem is RAM memory, because a typical X-displacement file has size 256M.

	Linear	Parabolic
$M = 3$	1h40	1h44
$M = 5$	8h18	9h30

Table 1: Computational time for perfect particle identification.

When comparing the times in table 1 to the 10 days necessary to the Milstein generation of the data, we conclude that we have developed a fast reconstruction algorithm.

CHAPTER V

VELOCITY PROFILE RECONSTRUCTION WITH EXACT MEAN DISPLACEMENTS

In this chapter, we consider exactly observed mean displacements. By this, we mean that the exact position of each particle is known in the simulation, but only the mean displacement is available for reconstruction. Cross-correlation processing of image pair in PIV (see chapter 6) extracts, up to various sources of error, the mean displacement of "matched" particles: those that contribute to both images. The general idea is the same as in chapter 4, we use a maximum likelihood estimate on a set of mean displacements. Therefore we first extend the probability density function to mean displacements, before presenting the algorithms, examples and error plots leading to the reconstruction for the three velocity profiles (11)-(13). During the reconstruction process, we use the Milstein simulated data as a given set of particle displacements forgetting the a-priori knowledge of the underlying deterministic velocity profile. Because all the information about $\gamma(aZ)$ is in the X-direction and we assume independence between in-plane displacement, we will not take into account the Y-displacements. Therefore, flow along two directions can be reconstructed individually.

5.1 Probability Density Functions

The problem is to find the probability density function of the mean of a random variable knowing the probability density function of the random variable.

Definition 5.1 *Let f be a probability density function. Define the characteristic function Φ_f of f as $\Phi_f(t) = \mathbb{E}(e^{itx})$.*

Remark

We note that the characteristic function can be written in the following way

$$\Phi_f(t) = \int_{-\infty}^{\infty} e^{ixt} f(x)dx = \mathcal{F}^{-1}_{\frac{x}{2\pi}}\left[f\left(\frac{x}{2\pi}\right)\right](t),$$

where $\mathcal{F}^{-1}$ is the inverse Fourier transform.

Theorem 5.1 *Let $\{X_i\}_{i=1}^n$ be a collection of independent random variables with identical probability distribution function f. Let $S_n = \sum_{i=1}^{n} X_i$ and let f_{S_n} be the probability distribution of the random variable S_n. Then*

$$f_{S_n} = f * f * \ldots * f,$$

where the convolution $*$ is taken n times.

Proof

Let Φ_f and $\Phi_{f_{S_n}}$ be the characteristic functions of f and f_{S_n}. Then

$$\Phi_{f_{S_n}}(t) = \mathbb{E}\left(e^{itS_n}\right) = \mathbb{E}\left(e^{it\sum_{i=1}^{n} x_i}\right) = \mathbb{E}\left(\prod_{i=1}^{n} e^{itx_i}\right).$$

Because the random variables are independent, we find

$$\Phi_{f_{S_n}}(t) = \prod_{i=1}^{n} \mathbb{E}(e^{itx_i}) = \prod_{i=1}^{n} \Phi_f(t) = \Phi_f(t) \cdot \ldots \cdot \Phi_f(t).$$

Using the previous remark the last result ca be written as

$$\Phi_{f_{S_n}} = \Phi_f \cdot \ldots \cdot \Phi_f = \mathcal{F}^{-1}[f] \cdot \ldots \cdot \mathcal{F}^{-1}[f].$$

The convolution theorem says that $\mathcal{F}[H \cdot H] = \mathcal{F}[H] * \mathcal{F}[H]$ or $H \cdot H = \mathcal{F}^{-1}[\mathcal{F}[H] * \mathcal{F}[H]]$.

By induction we have $H \cdot \ldots \cdot H = \mathcal{F}^{-1}[\mathcal{F}[H] * \ldots * \mathcal{F}[H]]$.

Thus with $H = \mathcal{F}^{-1}[f]$ we find

$$\Phi_{f_{S_n}} = \mathcal{F}^{-1}[\mathcal{F}[\mathcal{F}^{-1}[f]] * \ldots * \mathcal{F}[\mathcal{F}^{-1}[f]]] = \mathcal{F}^{-1}[f * \ldots * f].$$

Since $f_{S_n} = \mathcal{F}[\Phi_{f_{S_n}}]$, we have from the last result $f_{S_n} = f * \ldots * f$.

□

Remark

We recall that f_Z is the probability density function of the Z-location, that $f_{\Delta X}$ is the probability density function of the X-displacement, and that $f_{\Delta X|Z}$ is the probability distribution function of ΔX given Z.

Using conditional probability and the fundamental assumptions (59) and (55) we have

$$\begin{aligned} f_{\Delta X} &= \int f_{\Delta X|Z} f_Z dZ \\ &= \frac{a}{(H-a)\sqrt{2\pi\Pi_2}} \int_1^{H/a} \frac{1}{\sqrt{2\beta_{||}(aZ)}} e^{-\frac{(\Delta X - \Pi_1 \gamma(aZ))^2}{4\Pi_2 \beta_{||}(aZ)}} dZ. \end{aligned} \tag{63}$$

Let $\overline{\Delta X} = \frac{1}{n}\sum_{k=1}^{n} \Delta x_k$ be the mean displacement of n matched particles. We define the following probability distribution functions.

Definition 5.2 *Let f_S be the probability distribution function of $n\overline{\Delta X}$. Let f be the joint probability distribution function of N measured $n\overline{\Delta X}$.*

With theorem 5.1 we compute f_S as n times the convolution of $f_{\Delta X}$ with itself, in other words

$$f_S = f_{\Delta X} * \ldots * f_{\Delta X} \quad \text{with } f_{\Delta X} \text{ given by (63).} \tag{64}$$

The following figure (Fig. 13) shows the probability density function $f_{\Delta X}$ on the left and the probability density function f_S on the right computed for the linear profile (11) with $\Pi_1 = 3$ and $\Pi_2 = 4$. We know that the convolution of two vectors of length l produces a

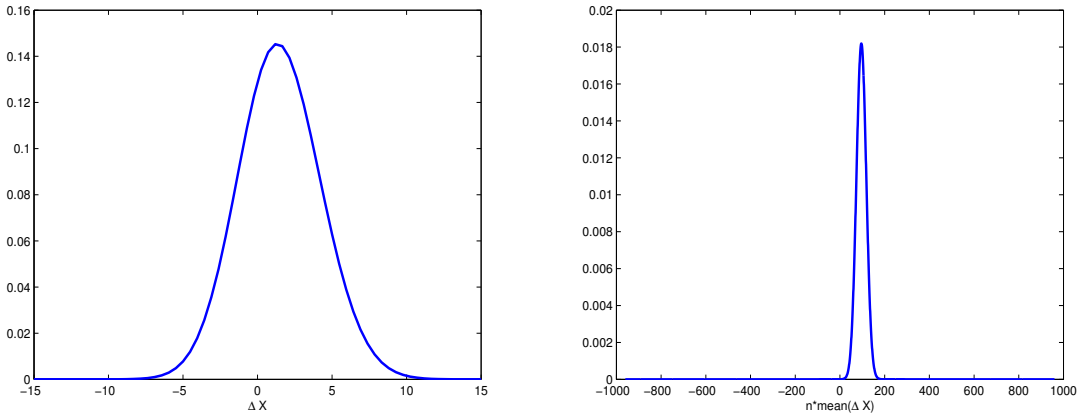

(a) $f_{\Delta X}$ (b) f_S

Figure 13: Probability density function of the displacements ΔX and of n times the mean of the displacements $n\overline{\Delta X}$ for the linear profile with $\Pi_1 = 3$ and $\Pi_2 = 4$.

vector of length $2l - 1$. Thus, if the domain of H is $[t_0, t_1]$ discretized at l points, then the

domain of $H * H$ will be $[2t_0, 2t_1]$ discretized at $2l-1$ points. Clearly the domain of f_S on figure 13(b) is 64 times larger than the domain of $f_{\Delta X}$ on figure 13(a). The other effect of the convolution is to narrow the width and height of the peak.

Figure 14 compares the histogram of a $n\overline{\Delta X}$ set with $Z \in [1, H/a]$ for the parabolic profile (12) with probability density function f_S computed with equation (64) (red dashed line). Going even further, the blue dotted line represents the probability density function obtained by fitting the data set $n\overline{\Delta X}$ for $Z \in [1, H/a]$ by a single Gaussian. The values of the parameters are $\Pi_1 = 3$, $\Pi_2 = 4$, $n = 64$ and $N = 2^{18}$. Again the differences between the integrated Gaussian (red dashed line) and the fitted Gaussian (blue dotted line) are minimal in the height and location of the peak. These minimal distinctions make the desired optimization highly sensitive, but there is nevertheless a gain in precision when using the integrated Gaussian.

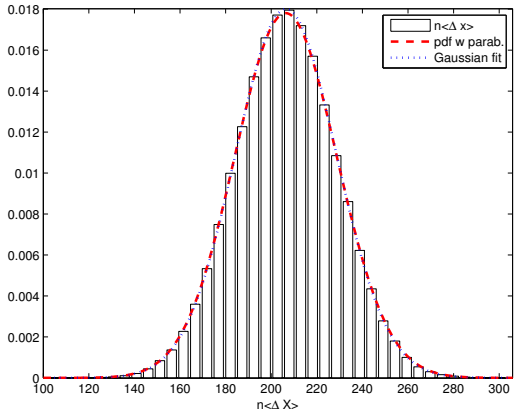

Figure 14: Comparison for the parabolic profile between the histogram of the distribution $n\overline{\Delta X}$, the integrated probability density function, and a fitted Gaussian with $n = 64$, $N = 2^{18}$, $\Pi_1 = 3$ and $\Pi_2 = 4$.

Finally, assuming independence between two window measurements, we have that the joint probability density function f is given by

$$f = \prod_{i=1}^{N} f_S \quad \text{with } f_S \text{ given by (64).} \tag{65}$$

5.2 Maximum Likelihood Estimate

Given N measured mean values $n\overline{\Delta X}$, Π_1, Π_2 and $\beta_{||}(aZ)$, we apply a maximum likelihood estimate on the probability density function of observed mean $X-$displacements. We define the function

$$\phi(\{\gamma_j\}_{j=1}^{M}) = -\sum_{i=1}^{N} \ln f_S(n\overline{\Delta X}_i), \tag{66}$$

where M is the number of discrete points Z at which we estimate γ. The most likely values for γ_j, $j = 1, \ldots, M$, are obtained by minimizing ϕ. The statistical reconstruction problem has been reduced to two numerical integrals and one minimization algorithm. First, we evaluate the probability density function f_S by repeated convolution (see Alg. 5.2) of the probability density function $f_{\Delta X}$, computing the integral by Gauss-Legendre quadrature for given γ_j, $j = 1, \ldots, M$ values at the Legendre collocation points (see Alg. 5.1). Finally, we minimize the function ϕ with a direct simplex algorithm penalizing solutions that do not produce an increasing sequence γ_j, $j = 1, \ldots, M$ (see Alg. 5.3).

5.2.1 Numerical Integration

Let $f_{\Delta X}^{num}$ denote the numerical approximation of $f_{\Delta X}(\Delta)$ and J denote the numerical approximation of $\int_1^{H/a} f_{\Delta X|Z}(\Delta, Z)dZ$ for given γ_j, $j = 1, \ldots, M$ and displacement Δ.

Algorithm 5.1 Numerical approximation of $f_{\Delta X}(\Delta)$

- Given: $\beta_{||}(aZ)$, Π_1 and Π_2
- Input: γ_j, $j = 1, \ldots, M$
- Define M Gauss-Legendre points s_j and weights w_j on $[-1, 1]$, $j = 1, \ldots, M$ ([33])
- Transform the points $Z_j \in [1, H/a]$ to s_j with $Z_j = 1 + \frac{s_j+1}{2}(\frac{H}{a} - 1)$, $j = 1, \ldots, M$
- Evaluate with Gauss quadrature $J = \frac{H-a}{2a} \sum_{j=1}^{M} w_j f_{\Delta X|Z}(\Delta, Z_j)$ with $f_{\Delta X|Z}$ as in (63)
- Probability distribution function $f_{\Delta X}^{num} = \frac{aJ}{H-a}$
- Output: $f_{\Delta X}^{num}$

Let f_S^i denote the numerical approximation of f_S for a given set of mean displacements $n\overline{\Delta X}_i$, $i = 1, \ldots, N$. First, we compute the convolution using the discrete Matlab function *conv* inductively over a fixed interval $[-L, L]$, where L is an estimate of the biggest probable displacement (usually $L = 20$). Because the convolution is nothing other than an integral we multiply the result of the discrete convolution by the length of the increment. Finally, we approximate $f_S(n\overline{\Delta X}_i)$ at the given $n\overline{\Delta X_i}$ by linear interpolation.

Algorithm 5.2 Numerical approximation of $f_S(n\overline{\Delta X}_i)$

- Given: $\beta_{||}(aZ)$, Π_1 and Π_2
- Input: γ_j, $j = 1, \ldots, M$
- Define a vector Δ of 64 equidistant (distance δ) points on $[-L, L]$
- For the displacement vector Δ compute $f_{\Delta X}^{num}$ with algorithm 5.1
- Set $g = conv(f_{\Delta X}^{num}, f_{\Delta X}^{num})\delta$
- Inductive loop over $k = 1, \ldots, n-2$: $g = conv(f_{\Delta X}^{num}, g)\delta$
- Normalize g to a probability density function
- Linearly interpolate g at $n\overline{\Delta X}_i$ to get f_S^i
- Output: f_S^i

5.2.2 Minimization with perfect mean displacements

Let Φ be the numerical approximation of ϕ. The fact that the velocity profile increases away from the wall can be included by discarding or penalizing non-increasing solutions. Because of the high sensitivity of the model, the first solution is inconclusive. We instead penalize non-increasing solutions by adding to the value of the function a factor (10^3) depending on the sum of the squares of the negative increment of γ. An initial guess $\gamma_{0,j}$ is obtained by searching the space of linearly spaced increasing sequence for a minimum of Φ for small M. For $M \geq 7$ we interpolate the initial guess from the final result for a smaller value of M.

Instead of an unknown profile γ we could assume that $\gamma(aZ) = \gamma_0 + \gamma_1 Z + \gamma_2 Z^2 + h.o.t$ and

Algorithm 5.3 Minimization with exact mean displacements

- Given: $\beta_{||}(aZ)$, Π_1 and Π_2
- Input: $\overline{\Delta X}_i$, $i = 1, \ldots, N$
- Initial guess: $\gamma_{0,j}$, $j = 1, \ldots, M$
- Numerical probability density function f_S^i with algorithm 5.2
- Function to be minimized: $\Phi(\{\gamma_j\}_{j=1}^M) = -\sum_{i=1}^{N} \ln f_S^i$
- Penalty: Add to Φ a multiple of the sum of the squares of the negative γ increments
- Minimization using *fminsearch*, a simplex direct search method
- Output: γ_j, $j = 1, \ldots, M$

substitute this into the minimization algorithm 5.3. Since this method reveals itself to be even more sensitive than the one described for a general γ, we will not study it further.

5.3 Results

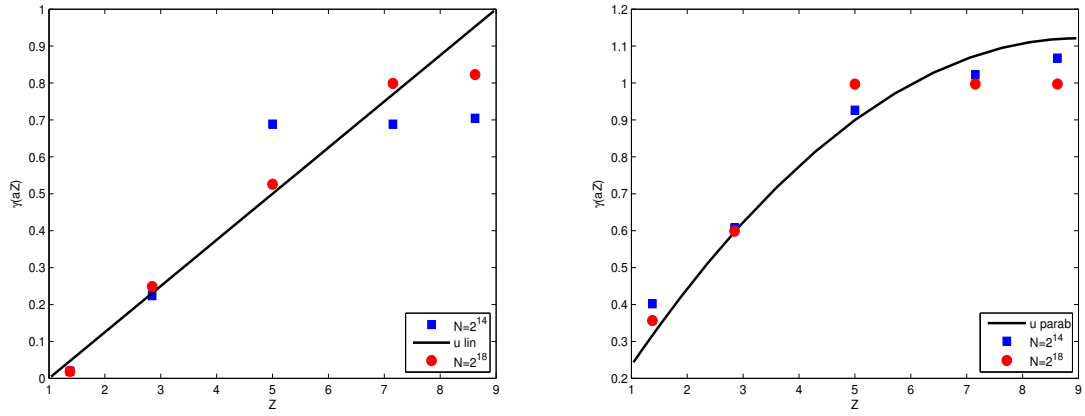

(a) Linear profile

(b) Parabolic profile

Figure 15: Exact mean: Velocity profile reconstruction at five points ($M = 5$) for the linear and parabolic profile with data set size $N = 2^{14}$ and $N = 2^{18}$.

We begin by applying the reconstruction algorithm 5.3 on the linear (11) and parabolic (12)

profile (Fig. 15) at $M = 5$ points with parameters $\Pi_1 = 3$, $\Pi_2 = 4$, $n = 64$ and two values for N, $N = 2^{14}$ or $N = 2^{18}$. In each figure, the underlying profile is plotted as a solid line.

5.3.1 Error plots

Since the accuracy of the reconstructed points does not appear to improve (see Fig. 15) when the data size N increases form 2^{14} to 2^{18}, we are motivated to instead consider breaking one block of data up into separate reconstructions over each of B blocks of size 2^b. To determine the best value for B and 2^b we study the behavior of the relative error. In figure 16, we compute the L^2-norm of the relative error of the reconstructed values

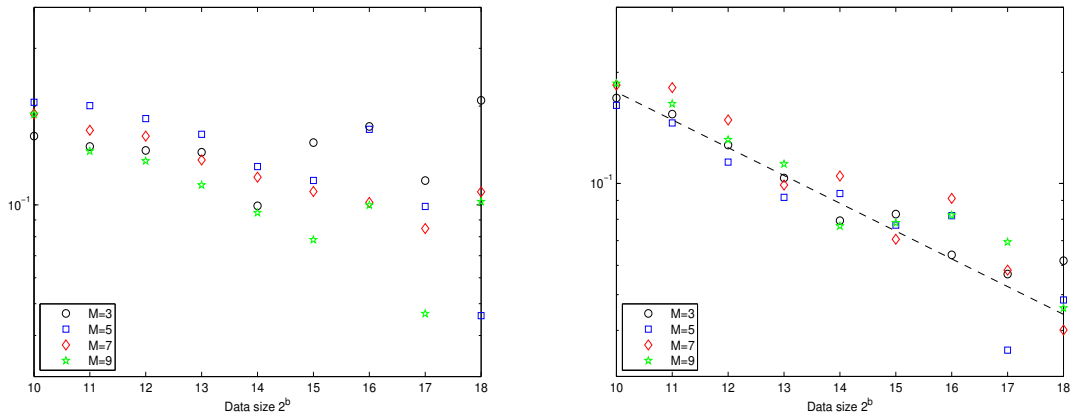

(a) Linear profile

(b) Parabolic profile

Figure 16: Exact mean: L^2-relative error averaged over the number of blocks B of size 2^b at $M = 3$, $M = 5$, $M = 7$, $M = 9$ for the linear and parabolic profile.

γ_j, $j = 1, \ldots, M$ with respect to the true $\gamma(aZ_j)$, $j = 1, \ldots, M$ for individual blocks, the errors being then averaged over the number of blocks B for four different values of M ($M = 3$, $M = 5$, $M = 7$, $M = 9$). In other words,

$$E_1 = \frac{1}{B} \sum_{k=1}^{B} \frac{\sqrt{\sum_{j=1}^{M} w_j |\gamma_j^k - \gamma(aZ_j)|^2}}{\sqrt{\sum_{j=1}^{M} w_j \gamma(aZ_j)^2}}, \tag{67}$$

where γ_j^k is the reconstructed value at Z_j for the block B_k, $k = 1, \ldots, B$, $j = 1, \ldots, M$. Note that we approximate the L^2-norm by a weighted Gauss-Legendre sum. The plots in figure

16 are semi-log plots of E_1 with respect to the exponent b in the block size 2^b. For the linear profile (Fig. 16(a)) we observe the same behavior as in figure 15(a), namely that increasing the data size does not improve the accuracy of the reconstruction. For the parabolic profile on the right (Fig. 16(b)), we find a decay of the relative error E_1 in function of the data size b of the form $(2^b)^{-1/4}$ revealing a stagnation of the error for data size larger than 2^{14}.

We consider next E_2, the L^2-norm of the relative error of the block averaged reconstructed values $\overline{\gamma_j}$, $j = 1, \ldots, M$, with respect to the true $\gamma(aZ_j)$, $j = 1, \ldots, M$ (Fig. 17). By $\overline{\gamma_j}$ we denote the average over the blocks of the reconstructed values

$$\overline{\gamma_j} = \frac{1}{B} \sum_{k=1}^{B} \gamma_j^k \quad j = 1, \ldots, M. \tag{68}$$

Thus in figure 17 we plot

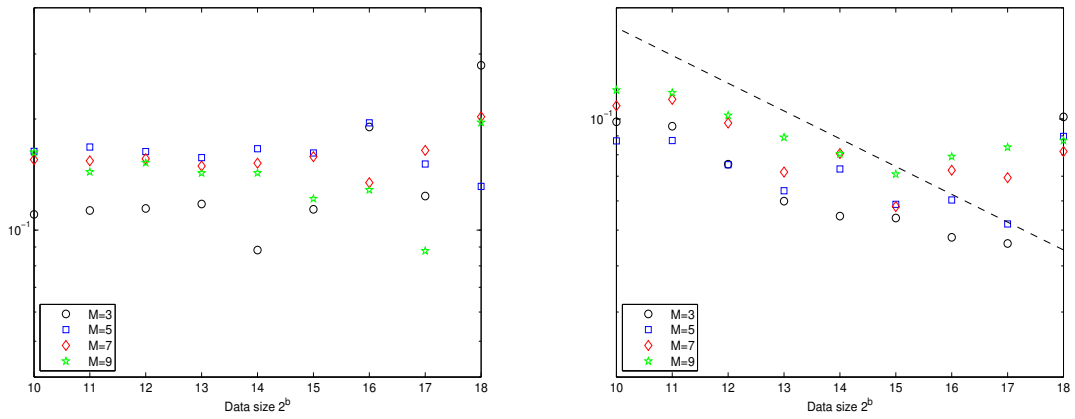

(a) Linear profile

(b) Parabolic profile

Figure 17: Exact mean: L^2-relative error with γ averaged over the number of blocks B of size 2^b at $M = 3$, $M = 5$, $M = 7$, $M = 9$ for the linear and parabolic profile.

$$E_2 = \frac{\sqrt{\sum_{j=1}^{M} w_j |\overline{\gamma_j} - \gamma(aZ_j)|^2}}{\sqrt{\sum_{j=}^{M} w_j \gamma(aZ_j)^2}}, \tag{69}$$

where γ_j^k is the reconstructed value at Z_j for the block B_k and w_j are the weights associated with the Gauss-Legendre quadrature, $j = 1, \ldots, M$, $k = 1, \ldots, B$. The plots in figure 17 are semi-log plots of E_2 with respect to the exponent b in the block size 2^b. The plots show that

averaging over more blocks of smaller size reduces the spread between the relative error for different M, but creates larger errors. Thus averaging reconstructed velocity profiles over blocks of data of smaller size improves the resolution of the reconstruction. This is visible for both the linear and parabolic profile, where starting with size $2^b = 2^{15}$ the relative error E_2 starts growing. Moreover, the parabolic profile (Fig. 17(b)) follows up to 2^{15} a decay close to $(2^b)^{-1/4}$. We deduce that the best reconstruction on a data set of size $N = 2^{18}$ will be achieved when the average of the reconstructed points is done over 8 or 16 blocks (size 2^{15} or 2^{14}). We also notice that increasing the number of discrete points to $M = 7$ or $M = 9$ does not produce significantly better results, but lengthens the computation time (see section 5.4).

In practice, of course, the goal of the reconstruction is to obtain the velocity profile, the true profile being unknown. So, finally, we compare the L^1-norm of the variance of the reconstructed profiles from the individual blocks, plotted as semi-log plot versus the exponent b in the block size 2^b (Fig. 18). By this, we mean

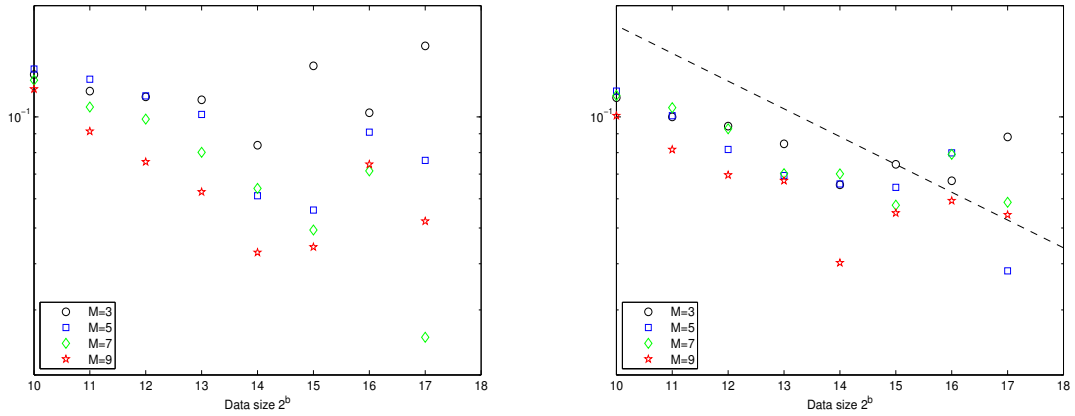

(a) Linear profile

(b) Parabolic profile

Figure 18: Exact mean: L^1-norm of the variance of γ averaged over the number of blocks B at $M = 3$, $M = 5$, $M = 7$, $M = 9$ for the linear and parabolic profile.

$$E_3 = \sum_{j=1}^{M} w_j \frac{1}{B} \sum_{j=1}^{B} (\gamma_j^k - \overline{\gamma_j})^2. \tag{70}$$

Again, we note for both the linear and parabolic profiles that the variance increases for data size bigger than 2^{15} with in the parabolic profile (Fig. 18(b)) a decay of the form $(2^b)^{-1/4}$. Figure 18 confirms that a better result can be obtained and recognized when averaging the reconstructed γ over $B = 8$ or $B = 16$ blocks corresponding to blocks of size 2^{15} or 2^{14}.

5.3.2 Linear, parabolic, and exponential reconstruction

Using the result of the block averaging technique investigated in the previous subsection (Figs. 16, 17 and 18) we now reconstruct the velocity profile for the linear case with $B = 16$ blocks and $M = 5$. In figure 19, we examine both the spread of the values obtained for each block, the average $\overline{\gamma_j}$, $j = 1, \ldots, M$ and standard deviation. The standard deviation is plotted as 90% confidence interval errorbars for the averaged block reconstructed values $\overline{\gamma_j}$, $j = 1, \ldots, M$. For comparison, we plot in figure 20 the averaged block reconstructed

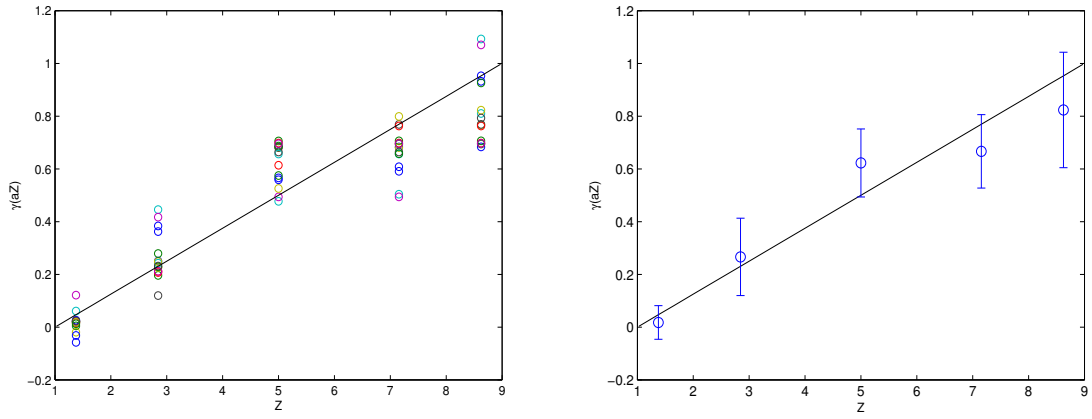

(a) Scatter plot

(b) Errorbar plot

Figure 19: Exact mean: (a) Scatter plot of the different block reconstructed $\overline{\gamma_j}$, $j = 1, \ldots, M$ and (b) block-averaged $\overline{\gamma_j}$, $j = 1, \ldots, M$ with 90% confidence interval for the linear profile with $B = 16$ and $M = 5$.

values $\overline{\gamma_j}$, $j = 1, \ldots, M$ for the linear profile with 16 blocks and 90% confidence interval for the cases $M = 3$ and $M = 7$. The four plots in figure 19 and 20 confirm that the block averaged reconstructed values $\overline{\gamma_j} = \frac{1}{B}\sum_{k=1}^{B} \gamma_j^k$, $j = 1, \ldots, M$ is a good approximation of

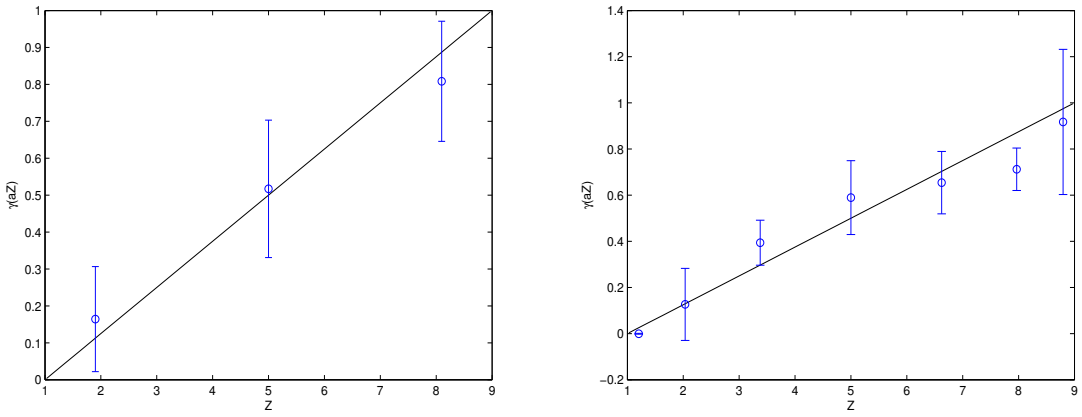

(a) $M = 3$ (b) $M = 7$

Figure 20: Exact mean: Block-averaged $\overline{\gamma_j}$, $j = 1, \ldots, M$ with 90% confidence interval for the linear profile with $B = 16$ and $M = 3$, $M = 7$.

$\gamma(aZ_j)$, $j = 1, \ldots, M$. Increasing the number of points M from 3 to 5 produces a better approximation, but more importantly it reduces consequently the size of the errorbars. Comparing figures 19(b) and 20(b) we see that there is not a significant gain in accuracy in increasing M from 5 to 7. Some of the errorbars (for example the first one) get smaller, while others (last one) get bigger during this process. Moreover, because the space of increasing sequence of length 7 is now too big to be heuristically searched, we interpolate the initial guess for $M = 7$ from the block averaged reconstructed values $\overline{\gamma_j}$, $j = 1, \ldots, M$ with $M = 5$. Therefore to obtain arguably a slightly better result with $M = 7$, we still need the reconstructed data from $M = 5$.

Next, we discuss the size of the errorbar at the last point Z_M. We recall that to make sure that particles stay in the channel we introduced a perfectly elastic reflection at the upper wall, $Z = H/a$ (see Section 3.3). This creates a bias in the sampled positions, since particles on both sides of the wall are represented with the same velocity. This effect is not present at the wall $Z = a$, because the diffusion coefficient is zero at the lower channel wall and with the chosen $\Delta\tau$ the simulated particles can not cross it (Section 3.3). Therefore the errorbar is shorter at the first point Z_1.

Figure 21 is the averaged block reconstructed values $\overline{\gamma_j}$, $j = 1, \ldots, M$ for the parabolic profile with $B = 16$ blocks and 90% confidence interval with $M = 3$ and $M = 5$. For both values of M the averaged block reconstructed profile $\overline{\gamma_j}$, $j = 1, \ldots, M$ is a good approximation of the parabolic profile. We note again a relatively large errorbar at the last point on figure 21(b).

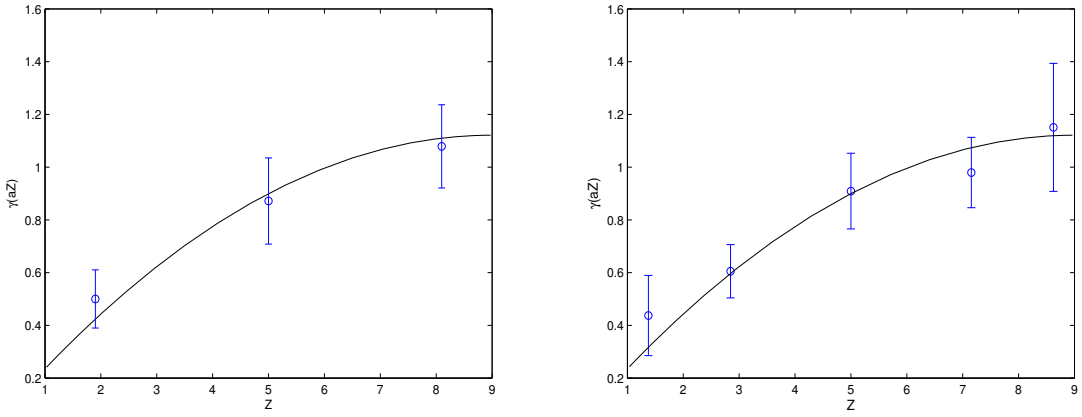

(a) $M = 3$ (b) $M = 5$

Figure 21: Exact mean: Errorbar reconstruction for the parabolic profile with $B = 16$, 90% confidence interval and $M = 3$, $M = 5$.

Finally, we apply the averaging block technique on the exponentially decaying velocity profile (Eq. (13)) at $M = 5$ points and $B = 16$ blocks and 90% confidence interval. Figure 22 illustrates the limitation of the block averaging statistical reconstruction on a fast increasing velocity profile. Keeping in mind that the last point might be biased, we see that the the statistical reconstruction is not able to recognize points of large inflexion (second point) correctly, while it reconstructs almost constant functions (third and fourth point) properly.

Nevertheless, because in the near-wall region the velocity profile is usually assumed to be linear or parabolic, we conclude that we have developed, ignoring the last point, a probabilistic algorithm to reconstruct the velocity profile at four Z-locations given exact mean X-displacements and a computation domain of the same size than the observation domain.

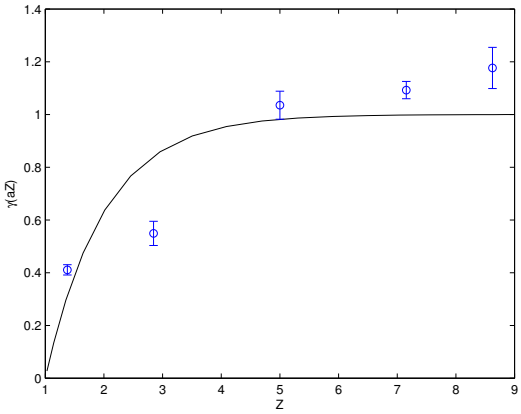

Figure 22: Exact mean: Errorbar reconstruction for the exponentially decaying profile with $B = 16$, $M = 5$ and 90% confidence interval.

5.4 Computational Cost

We discuss the computational cost of the different reconstructions. The mean displacement data generated by the Milstein code (see Chap. 3) are saved as binary files of size 128K. The machine is an 18 nodes beowolf cluster, where each node is a dual 2 GHZ AMD Athlon with 2 GB RAM. The filestore is a dual AMD 2800+ Athlon with 16B RAM.

Because the entire problem can be reduced to a minimization of the function Φ, Φ has to be evaluated at M points for the entire block of data of size N/B. Thus the major resource restriction is RAM memory. Moreover, at each function evaluation the probability density function using recursively $n - 1$ discrete convolutions has to be computed.

The following three tables 2, 3 and 4 contain the computational time required for the averaged block reconstruction for different number of blocks B, and correspondingly data size 2^b, for the linear and parabolic profile with $M = 5$ (Table 2), $M = 3$ (Table 3) and $M = 7$ (Table 4). From the tables 2 and 3, we see that, when compared to the time required to generate the data (10 days, see Chap. 3) the minimization routine is fast. For example, the studied case of $B = 16$ blocks is computed in about 15 minutes. When $M = 3$

B	256	128	64	32	16	8	4	2	1
2^b	2^{10}	2^{11}	2^{12}	2^{13}	2^{14}	2^{15}	2^{16}	2^{17}	2^{18}
Lin.	3h40	2h	57min	33min	17min	10min	8min45	8min30	2min30
Par.	3h45	1h50	52min	27min	13min30	9min	7min	6min	7min30

Table 2: Exact mean: Computational time for the linear and parabolic profile as a function of B with $M = 5$.

B	256	128	64	32	16	8	4	2	1
2^b	2^{10}	2^{11}	2^{12}	2^{13}	2^{14}	2^{15}	2^{16}	2^{17}	2^{18}
Lin.	1h25	45min	23min30	13min	6min	5min	4min	4min	4min
Par.	1h30	46min	24min	14min	7min30	5min	3min	3min	4min

Table 3: Exact mean: Computational time for the linear and parabolic profile as a function of B with $M = 3$.

(Table 3) both the linear and parabolic profiles run in the same amount of time. On the other hand, when $M = 5$ (Table 2) starting with $B = 8$ the reconstruction of the parabolic profile is achieved more quickly than of the linear profile. This can hardly be explained, but it might simply be related to this particular data set. In this sense, when the number of blocks gets bigger, the size of each one gets smaller and therefore it is harder to find an appropriate minimum with fewer points. Also worth noticing is the fact that as the number of blocks increases, there are more values to store. As an approximate rule of thumb, we say that starting with $B \geq 8$, doubling the number of blocks double the computational time. The next table 4 is the computational time for $M = 7$. This table confirms that the slightly better accuracy obtained with 7 points compared to 5 points is not worth the computational effort for two reasons. First of all, the computational time has increased by a factor of between five and ten and second of all, this reconstruction can only be obtained when the suitable initial guess is given through the result of a 5 points reconstruction, adding more time to the entire process.

B	256	128	64	32	16	8	4	2	1
2^b	2^{10}	2^{11}	2^{12}	2^{13}	2^{14}	2^{15}	2^{16}	2^{17}	2^{18}
Lin.	7h10	3h15	1h34	46min	30min	12min	14min	17min	19min
Par.	13h30	6h45	3h50	1h47	1h16	40min	35min30	23min	26min

Table 4: Exact mean: Computational time for the linear and parabolic profile as a function of B with $M = 7$.

Finally, table 5 contains the number of function evaluations and iterations for each of the 16 blocks of size 2^{14} of the block averaged reconstructed values $\overline{\gamma_j}$, $j = 1, \ldots, M$ for the linear (Table 5 top) and parabolic profile (Table 5 bottom) at $M = 5$ discrete points. Those numbers have purely an informative value, as they can, from one block to another block of the same size, quadruple. The only pattern that can be noticed is that the number of function evaluations is roughly 1.5 to 2 times the number of iterations.

Block	1	2	3	4	5	6	7	8	9	10	11	12	13
Eval.	652	584	541	503	731	399	568	503	478	775	271	501	174
Iter.	400	350	329	301	443	230	337	303	281	486	156	297	96

Block	14	15	16
Eval.	466	668	397
Iter.	279	398	238

Block	1	2	3	4	5	6	7	8	9	10	11	12	13
Eval.	216	358	231	575	845	267	828	191	435	369	239	391	661
Iter.	116	200	126	347	528	153	508	108	254	222	138	230	405

Block	14	15	16
Eval.	293	195	430
Iter.	167	105	252

Table 5: Exact mean: Function evaluations and iterations for the linear (top) and parabolic (bottom) profile with $M = 5$.

CHAPTER VI

VELOCITY PROFILE RECONSTRUCTION WITH PIV MEANS

In the previous chapter (Chap. 5), we demonstrated that it is possible to statistically reconstruct the velocity profile based on the probability density function of perfect mean X-displacements between window pairs. However, in the experimental set-up, the mean displacements are not exact, but approximated through PIV imaging techniques. The goal of PIV is to extract from two image windows the mean displacement of n particles without the knowledge of the individual displacements under the assumption that particles have comparable displacements. In the first part of this chapter, we describe basic cross-correlation algorithms (see [19], [37], [35]). Then we test the reconstruction on approximated mean X-displacements using the same algorithms (Alg. 5.1, 5.2, 5.3) as in chapter 5.

6.1 Particle Image Velocimetry (PIV)

6.1.1 Image matrix

From the simulation of the dimensionless Langevin system (19)-(21) with the Milstein scheme (Chap 3) we generate flows of tracer particles over time. If the particles were point-particles we could define for each cell of a given grid a value based on the number of point-particles present in the cell. Since the particles have a radius and their centers are not necessarily in the center of the cell, they can cover more than one grid cell. Therefore we consider a grid of size M_x by M_x and a Gaussian intensity distribution

$$I(\mathbf{r}) = I_0 \exp\left(\frac{-||\mathbf{r}-\mathbf{r}_0||^2}{2\sigma_p^2}\right) \quad \mathbf{r} = (X, Y), \tag{71}$$

where $\mathbf{r}_0$ is the position of the center of the cell and I_0, σ_p are constants. A radius σ_p of 1 means that 68.3% of light scattered by the particle is imaged onto a circular area of radius 1. The parameters are chosen to match the experimental parameters ([29]): the size of the region of interest is $H_x = 25\mu$m, $H_y = 5\,\mu$m, $H = 450$ nm, $a = 50$ nm, $n = 64$, $M_x = 32$,

$\sigma_p = 2$ and $I_0 = 255\exp(-Z/100)$ is the exponentially decaying intensity function. To each grid cell corresponds an entry in the image matrix obtained with the intensity $I(\mathbf{r})$ given by (71). Because the grid is generated from the bottom left corner of the window and the matrix from the top left corner, the intensity of a particle located in the cell with left-hand corner (j, i) is reported in the entry $(M_x - i + 1, j)$ of the image matrix as illustrated in the following figure (Fig. 23). If there is more than one particle in a grid cell, the intensity

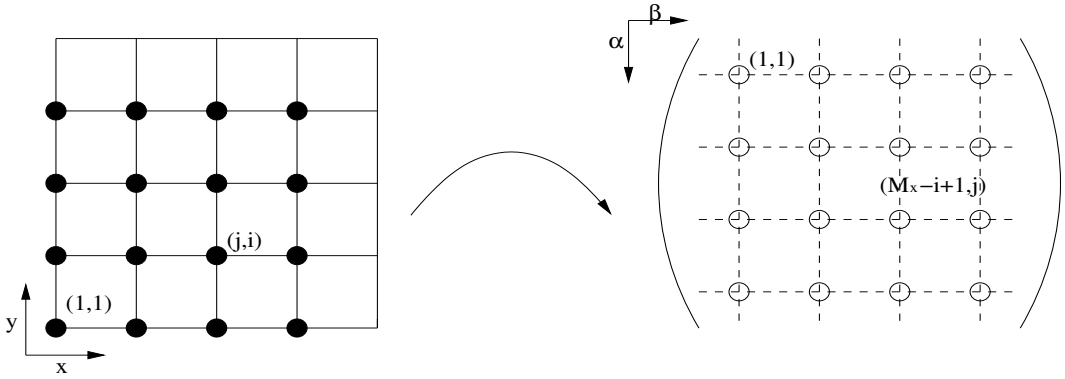

Figure 23: Correspondence between grid elements and matrix entries.

at that entry is the sum of the intensities for each particle. Algorithm 6.1 describes the generation of the image matrix. Note that, in order to include the particles in the last row and column of the grid, we expand the grid to an $M_x + 2$ by $M_x + 2$ grid with no particle in the added cells.

Algorithm 6.1 Generation of the image matrix

- Given: cell with left-hand edge (j, i) and center $\mathbf{r}_0 = (X_0, Y_0)$
- Input: $X_i, Y_i, Z_i\, i = 1, \ldots, n$, $M_x \times M_x$ grid with midpoints and edges
- Find the m particles in the cell with position $\mathbf{r}_i = (X_i, Y_i)$, $i = 1, \ldots, m$
- Compute $I_0^i = 255\exp\left(\frac{-Z_i}{100}\right)$, $i = 1, \ldots, m$
- Intensity: $I(\mathbf{r}_i) = I_0^i \exp\left(\frac{-||\mathbf{r}_i - \mathbf{r}_0||^2}{2\sigma^2}\right)$, $i = 1, \ldots, m$
- Output: $im(M_x - i + 1, j) = \sum_{i=1}^{m} I(\mathbf{r}_i)$

6.1.2 Cross-correlation function and displacement

Definition 6.1 *Let im_1 and im_2 be two image matrices. The discrete cross-correlation function $\Phi_{12}^{norm}(m,n)$ of the sampled images $im_1(m,n)$ and $im_2(m,n)$ is given by (see [19], [37])*

$$\Phi_{12}^{norm}(m,n) = \frac{\sum_{k=-\infty}^{\infty}\sum_{l=-\infty}^{\infty} im_1(k,l)im_2(k+m,l+n)}{\sum_{k=-\infty}^{\infty}\sum_{l=-\infty}^{\infty} im_1(k,l)\sum_{k=-\infty}^{\infty}\sum_{l=-\infty}^{\infty} im_2(k,l)}.$$

From the definition we remark the following.

Remarks

1. If im_1 and im_2 are δ-functions of particles with a radius of 1, then the numerator of Φ_{12}^{norm} is non-zero exactly when (k,l) is the position of the particle in the first image and (m,n) corresponds to the displacement between the two images.

2. The denominator of Φ_{12}^{norm} is a normalization coefficient, so that when many particle images match up with their corresponding shifted particles, the cross-correlation value is near 1.

Let Φ_{12} denote the non-normalized discrete cross-correlation function, in other words the numerator of the cross-correlation function Φ_{12}^{norm}. Φ_{12} is nothing else than the two-dimensional discrete convolution. Therefore we apply the two-dimensional convolution theorem which relates complex multiplication in frequency domain to convolution in space domain. Algorithm 6.2 uses two-dimensional Fast Fourier Transform to compute Φ_{12}.

Algorithm 6.2 Non-normalized discrete cross-correlation function

- Input: image matrices im_1 and im_2 computed with algorithm 6.1
- $F = fft2(im_1) \quad G = fft2(im_2)$, two-dimensional Fast Fourier Transform
- $\Theta = F \cdot \overline{G}$
- $\Phi_{12} = fft2^{-1}(\Theta)$ two-dimensional inverse Fourier transform
- Output: Φ_{12}

The location of the maximum peak of the cross-correlation function gives a first approximation of the mean displacement between the windows. Because an immobile particle should have a peak located at $(0, 0)$, we shift the entries of Φ_{12} with the command *fftshift* so that the zero frequency components are in the center of the spectrum. Finally, we convert the displacements expressed in matrix-coordinates to true displacements (see Fig. 23). Since a displacement in the X-grid direction corresponds to an integer multiple of the β-matrix coordinates (column), the approximated X-displacement is computed from the j location of the peak. In a similar way, because a displacement in the Y-grid direction is equivalent to a negative integer multiple of the α-matrix coordinate (row), the approximated Y-displacement uses the i location of the peak and reverses the sign. The factors $M_x/2+1$ reflect the shifting of the components (see Alg. 6.3).

Algorithm 6.3 Approximated mean displacements

- Given: $M_x \times M_x$ grid with cell size δ_x
- Input: Φ_{12} from algorithm 6.2
- Find $[i, j]$ the location of Φ_{12}^{max} the maximum of $fftshift(\Phi_{12})$
- $\overline{\Delta X}_{app} = (M_x/2 + 1 - j)\delta_x$
- $\overline{\Delta Y}_{app} = -(M_x/2 + 1 - i)\delta_x$
- Output: $\overline{\Delta X}_{app}$, $\overline{\Delta Y}_{app}$, and Φ_{12}^{max}

6.1.3 Gaussian surface fitting

To obtain an approximation of the mean displacement with an accuracy finer than the grid size δ_x, we use a Gaussian surface fitting technique (see [29]). The mean displacement between two windows is the first moment of the distribution of the displacements. To first order, the probability density function of the displacement can be approximated by a Gaussian of the form (see also Fig. 9 and Fig. 14)

$$w = h(X, Y) = a_1 e^{a_2(X-a_3)^2 + a_4(Y-a_5)^2}, \tag{72}$$

where a_3 and a_5 determine the mean X- and Y-displacements. From the previous algorithm 6.3 we have a first estimate of $a_1^0 = \Phi_{12}^{max}$, of $a_3^0 = \overline{\Delta X}_{app}$ and of $a_5^0 = \overline{\Delta Y}_{app}$. To gain better accuracy, we want to determine the constants $a_1, \ldots, a_5$ as a best fit through the eight points surrounding the peak. We number the neighbors starting from the top left corner (see Fig. 24) and we assume equidistant points. Since the center point corresponds

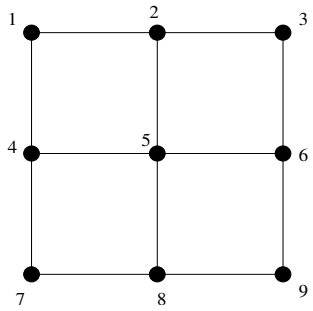

Figure 24: Eight neighbors grid.

to the maximum, we have $w_5 = h(a_3, a_5) = a_1$. Moreover, we find $w_2 = h(a_3, a_5 + \delta_x)$, $w_8 = h(a_3, a_5 - \delta_x)$, $w_6 = h(a_3 + \delta_x, a_5)$ and $w_4 = h(a_3 - \delta_x, a_5)$, where δ_x is the length of the cell. Therefore the initial guesses for a_2 and a_4 are given by

$$a_2^0 = \frac{\ln((z_4 + z_6)/(2a_1^0))}{\delta_x^2} \quad \text{and} \quad a_4^0 = \frac{\ln((z_2 + z_8)/(2a_1^0))}{\delta_x^2}. \tag{73}$$

Algorithm 6.4 finds the coefficients $a_1, \ldots, a_5$ using the non-linear minimization *lsqcurvefit*. Figure 25 is a mesh plot of the cross-correlation function Φ_{12} given by algorithm 6.2 to-

Algorithm 6.4 Gaussian surface fitting

- Given: $M_x \times M_x$ grid with cell size δ_x
- Input: Φ_{12}^{max} from algorithm 6.2, $\overline{\Delta X}_{app}$ and $\overline{\Delta Y}_{app}$ from algorithm 6.3
- Determine the 8 neighbors (Fig. 24)
- Function to be minimized: $w = a_1 e^{a_2(X-a_3)^2 + a_4(Y-a_5)^2}$
- Initial guess: $a_1^0 = \Phi_{12}^{max}$, $a_3^0 = \overline{\Delta X}_{app}$, $a_5^0 = \overline{\Delta Y}_{app}$, a_2^0 and a_4^0 given by (73)
- Minimization of w using *lsqcurvefit*, a non-linear least-squares curve fitting algorithm
- Output: $a_1, \ldots, a_5$

gether with a surface plot of the Gaussian density function (Eq. (72)) with the coefficients

$a_1, \ldots, a_5$ obtained from algorithm 6.4. There is noise in the cross-correlation function,

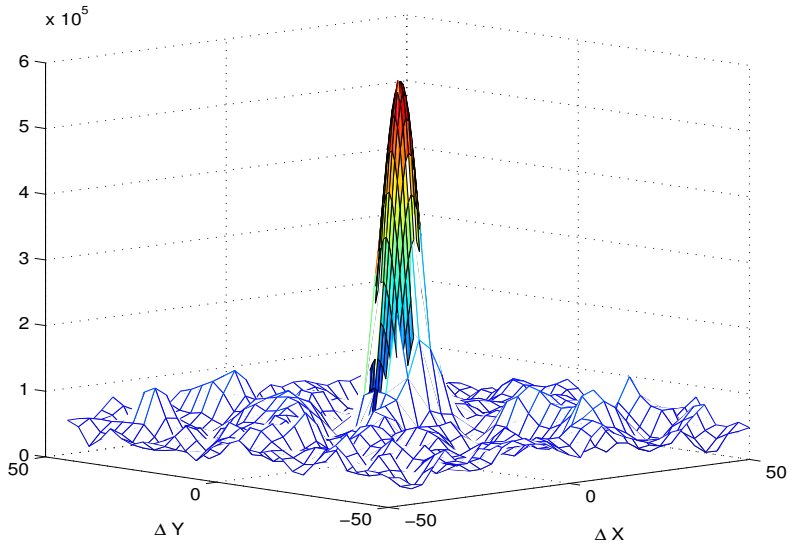

Figure 25: Gaussian surface fitting of the cross-correlation peak.

but not enough to forbid the detection of the peak. The Gaussian fitting algorithm 6.4 produces a smoother peak which allows for the determination of the approximated mean $X-$displacement as a_3.

Combining algorithms 6.1, 6.2, 6.3 and 6.4 we can find an approximate mean displacement between a window pair. Here, we note two important simplifications. First, we have not included any background noise, which pollutes the determination of the mean displacement. Second, we have not discussed overlapping windows or averaging cross-correlation function (see [35]). This last improvement is necessary with experimental data to overcome the uncertainties due to noise.

Because, in our case $H_x = 5H_y$, we decompose one image into five windows of size $H_y \times H_y$ without overlapping. We then average the five mean velocities obtained through cross-correlation to approximate the mean displacement over the window $H_x \times H_y$.

Sadr *et al.* ([29]) establish that for 2% particle mistach, the absolute error in the approximated mean is 0.0002 pixels. The absolute error becomes important with 45% particle mismatch. We apply the cross-correlation algorithms on the linear and parabolic data with $N = 2^{18}$, $\Pi_1 = 3$ and $\Pi_2 = 4$. There is no particle mismatch, however only half of the data lie within an absolute error of 0.0005 of their true value. This can be explained by the fact that approximating mean displacements through cross-correlation works only if the particle displacements of each particle are comparable to each others and are reasonable compared to the grid size. We proceed by applying the reconstruction algorithm on the smaller data set of PIV mean with an absolute error smaller than 0.0005.

6.2 Results

Because the data set has roughly 2^{17} points we start with the reconstruction profile at $M = 3$ points with $B = 8$ blocks (see Chap. 5) for the linear profile (11) and the parabolic profile (12). In figure 26, we plot the block averaged reconstructed mean together with

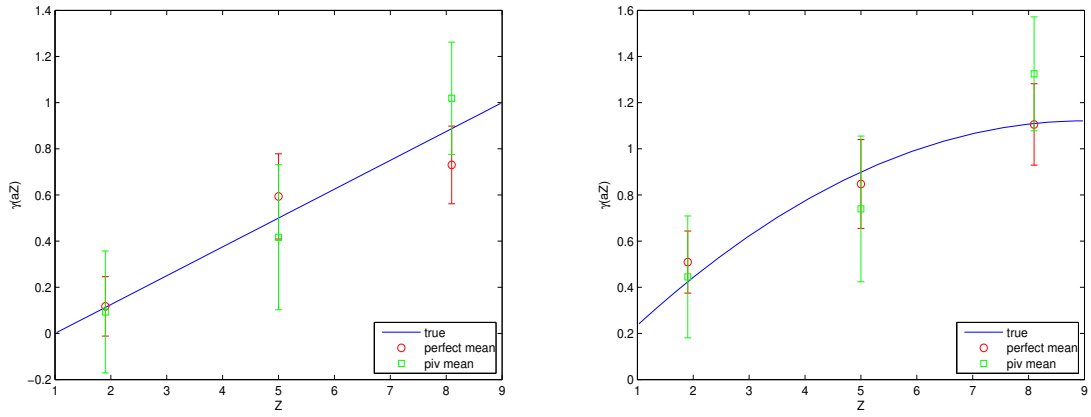

(a) Linear profile

(b) Parabolic profile

Figure 26: PIV: Errorbar reconstruction for the linear and parabolic profile with perfect mean and PIV approximated mean within 0.0005 absolute error, $M = 3$, $B = 8$ and 90% confidence interval.

90% confidence interval for perfect mean (red circle) and PIV approximated mean (green square) within 0.0005 absolute error. We first notice that the errorbars are longer with PIV

approximated mean than with exact mean. This makes perfect sense, since the additional errors due to the approximation of the means with cross-correlation techniques are included. The second aspect is that the last reconstructed point, especially in the parabolic profile (Fig. 26(b)), is badly approximated. There are two reasons for this: the upper wall and the penalty in the minimization. We already discussed in chapter 5 the effect of the artificial reflection at the upper wall on the reconstruction with perfect means. This phenomena is here augmented by the errors in the approximation of the means. We remember that the penalty in algorithm 5.3 was determined by a constant (usually 10^3) multiplying the sum of the squares of the negative γ increments. The effect of the constant is to force *fminsearch* to look for a minimum in a different neighborhood. However, if the only non increasing point is the last one, this may cause the new neighborhood to be too far away from the true values resulting in a bigger error at the last point.

Next (Fig. 27), we reconstruct the velocity profile using block averaging with $B = 16$, $M = 5$ for the linear and parabolic profile for the exact mean data set of size 2^{17} and for the one with approximated PIV mean. The conclusions from figure 27 are similar to the

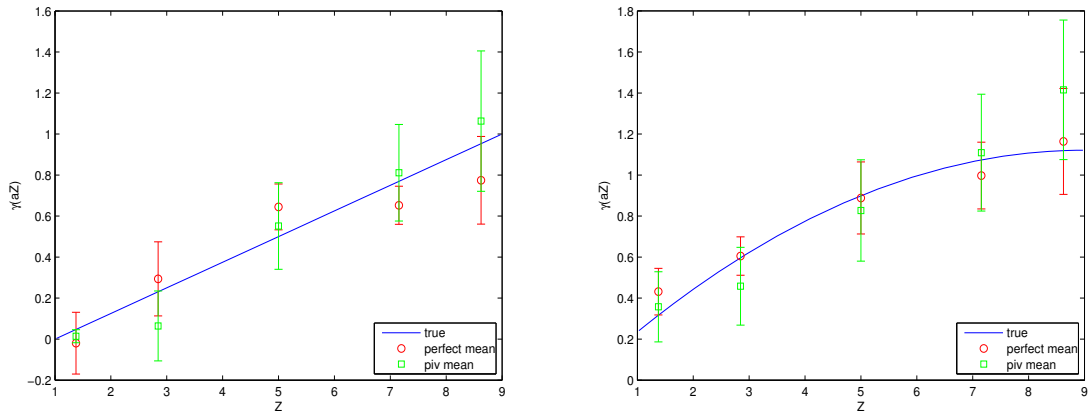

(a) Linear profile

(b) Parabolic profile

Figure 27: PIV: Errorbar reconstruction for the linear and parabolic profile with perfect mean and PIV approximated mean within 0.0005 absolute error, $M = 5$, $B = 16$ and 90% confidence interval.

results derived from figure 26. The errorbars for PIV approximated means are longer than exact mean displacements and the block averaged values $\overline{\gamma_j}$, $j = 1, \ldots, M$ produce, except at the last point, a good approximation of the corresponding values $\gamma(aZ_j)$, $j = 1, \ldots, M$. It is worth noticing that for the linear profile (Fig. 26(a)) the reconstructed point at Z_5 is actually better with PIV approximated means, than with exact means another illustration of the high sensitivity of the reconstruction.

Because the data used for PIV means is about half the size of the one used with exact means and because experimentally PIV displacements are obtained with high accuracy, we conclude that it is possible to statistically reconstruct the out-of-plane dependence of the velocity profile from in-plane images. Moreover, since experimentalists are mostly interested in the velocity profile in the near-wall region, it is not a major drawback that the block averaged reconstructed value closer to the upper wall has the largest errorbar.

6.3 Computational Cost

It takes, on a dual 2GHz AMD Athlon with 2GB RAM processor, between 5 and 10 seconds to approximate one X-mean displacement with algorithms 6.1-6.4. Because each cross-correlation is independent from the previous one, the generation of PIV data based on a set of displacements can be broken onto different processors, allowing for the computation to run in about 32 hours. We finish by summarizing the size of the files and the computational time needed for each of the steps of the entire reconstruction algorithm.

Step	Method	Computational time	File size
Data generation	Milstein and Ito double integral	10 days	3×256M
PIV	Cross-correlation and Gaussian fit	32 hours (parallel)	2M
Reconstruction	Minimization and Block average	15 minutes	M values

Table 6: Summary of the computer resource needed for the statistical reconstruction with PIV generated data.

CHAPTER VII

BIAS IN THE $Z-$DISTRIBUTION OF MATCHED PARTICLES

In the reconstruction algorithms in chapter 4-6 we assumed that the computation and observation domain were the same. This means that the distribution of particles in the Z-direction perpendicular to the wall is uniform. However, when the domains are different, the particles can move out and back into the window (computation domain) during the measurement time T. Because of the lack of information about the Z-locations of the particles, it is usually assumed, when there is more than one window in the observation domain, that the measured in-plane mean velocities represent the value at the Z-middle height. This supposes that the distribution of the Z-locations of particles that start and end in the window is uniform. In the next section, we show with a simple Milstein simulation based on the Z-Langevin equation (21) that the distribution of matched particles at nanoscale is not uniform. Again this is a consequence of hindered Brownian diffusion. Then, using a one dimensional space-time Fokker-Planck equation (4) we derive a fast algorithm computing the distribution of matched particles. Finally, we study some implications in terms of mismatch, drop-out and slip length.

7.1 Numerical Simulation of Particle Positions

We make the variable transformation: $H_e = Z - 1$ for $Z \in [1, H/a]$. H_e corresponds to the nondimensional edge-wall distance. This means that the wall is located at $H_e = 0$. For the rest of this chapter, every distance will be given in edge-wall distance. Let C be the dimensionless center of the window and let W be the dimensionless height of the window. Note that $W \leq H/a - 1$. With the variable transformation, the H_e-nondimensionalize Langevin equation in the direction perpendicular to the wall (Eq. (21)) becomes

$$dH_e = \Pi_2 \frac{d\beta_\perp(a(H_e+1))}{dZ} d\tau + \sqrt{2\Pi_2 \beta_\perp(a(H_e+1))d\tau} dW, \tag{74}$$

where $dW = \mathcal{N}(0,1)$, Π_2 is the dimensionless diffusive time, $\beta_\perp$ is the perpendicular component of the diffusion tensor (9). For simplicity, we set

$$\beta_\perp(a(H_e+1)) = \frac{6H_e^2+2H_e}{6H_e^2+9H_e+2} = \beta_\perp^e(H_e). \tag{75}$$

Following the discussion of chapter 3, the corresponding one dimensional Milstein scheme is

$$H_e^{j+1} = H_e^j + \Pi_2 \frac{d\beta_\perp^e}{dH_e}\bigg|_{H_e^j} \Delta\tau + \sqrt{2\Pi_2\beta_\perp^e(H_e^j)\Delta\tau}\Delta\omega + \frac{\Pi_2}{2}\frac{d\beta_\perp^e}{dH_e}\bigg|_{H_e^j} \Delta\tau(\Delta\omega^2-1) \tag{76}$$

with $j = 1,\ldots,N_t$, $\Delta\tau = 1/N_t$ and $\Delta\omega$ is normally distributed with mean 0 and variance 1. In the case that $H_e^j \leq 0$, we impose an artificial elastic boundary condition at the wall: $H_e^j = -H_e^j$. The initial distribution is uniform in the window $[C-W/2, C+W/2]$.

Figure 28 is the histogram of the H_e-locations of matched particles for the two cases $\Pi_2 = 1$ and $\Pi_2 = 5$ with $C = 0.5$ and $W = 1$ and a fixed radius $a = 50$ nm. The histogram is obtained by determining the particles in the window $[C-W/2, C+W/2]$ at $\tau = 1$ and plotting their corresponding locations at all in-between times. We set $N_t = 2^{10}$ and repeat the simulation 2^{11} times for $n = 32$ particles. Both plots show that the distribution of

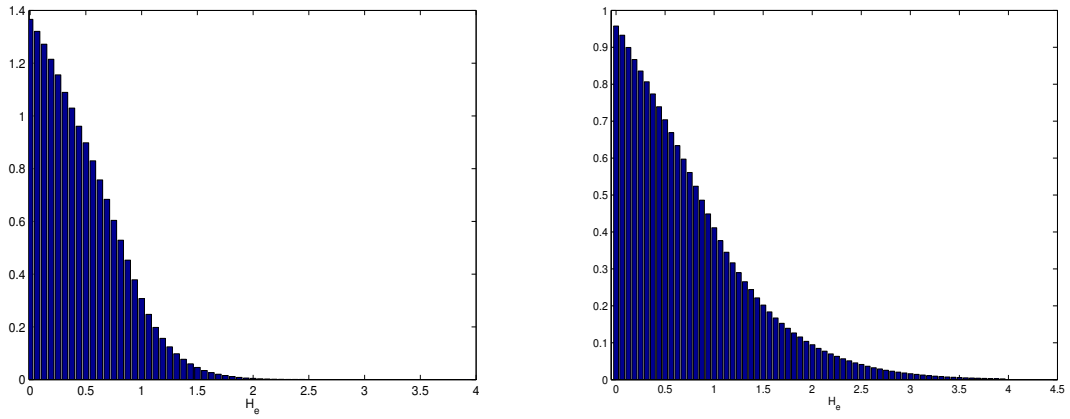

(a) $\Pi_2 = 1$ (b) $\Pi_2 = 5$

Figure 28: Histogram of the matched particles for $C = 0.5$ and $W = 1$ for $\Pi_2 = 1$ and $\Pi_2 = 5$.

matched particles is not uniform and not symmetric, since the window is the one closest

to the wall. Because of the cost in terms of RAM memory, we are motivated to find an alternate approach which computes directly the H_e-distribution of matched particles.

Since $\Pi_2 = \frac{D_\infty T}{a^2}$, there are two ways of decreasing Π_2: decreasing T the time elapsed between the window measurements or increasing the radius of the particle a. Because D_∞ is inversely proportional to a the dependence of Π_2 from a is inversely cubic. Thus, decreasing the particle radius to the quantum dot range ($a = 5$ nm, see [27]) has the dramatic effect of increasing Π_2 to about 20000.

7.2 Probability Density Function of Matched Particles

Let $\mathcal{W}(H_e, \tau)$ denote the probability density function of H_e at time τ given that the initial distribution at $\tau = 0$ is $\mathcal{W}_0(H_e)$. Then, the nondimensional one dimensional space-time Fokker-Planck equation in configuration space becomes (see Eq. (22))

$$\frac{\partial \mathcal{W}(H_e,\tau)}{\partial \tau} = \Pi_2 \frac{\partial}{\partial H_e}\left(\beta_\perp^e(H_e)\frac{\partial \mathcal{W}(H_e,\tau)}{\partial H_e}\right). \tag{77}$$

At the wall ($H_e = 0$) we use a Neumann boundary condition describing the no-flux condition. Let L be large enough so that no particle has a displacement bigger than L. We always have that $L \leq H$, where H is the height of the channel or depth of field of vision. Thus, we impose the same Neuman boundary condition at $H_e = 0$ and $H_e = L$:

$$\left.\frac{\beta_\perp^e(H_e)\partial \mathcal{W}(H_e,\tau)}{\partial H_e}\right|_{H_e=0} = \left.\frac{\beta_\perp^e(H_e)\partial \mathcal{W}(H_e,\tau)}{\partial H_e}\right|_{H_e=L} = 0. \tag{78}$$

The initial distribution $\mathcal{W}_0(H_e)$ is uniform in the window $[C - W/2, C + W/2]$:

$$\mathcal{W}_0(H_e) = \frac{1}{W}\chi_{[C-W/2,C+W/2]}(H_e). \tag{79}$$

$\mathcal{W}(H_e, \tau)$ is the distribution of H_e-locations starting from the uniform distribution (79), but it is not the probability density function of matched particles. Let $\mathcal{P}(H_e)$ be the probability density function of matched particles, that is particles that are in the window $[C - W/2, C + W/2]$ at $\tau = 0$ and in the window at $\tau = 1$. Let (H_e, τ) with $\tau < 1$ be the position of a particle at some time τ. The probability that this particle is a matched

particle is given by the probability that there is a path from $(H_{e,0}, 0)$ to (H_e, τ) with $H_{e,0} \in [C - W/2, C + W/2]$ and a path from (H_e, τ) to $(H_{e,1}, 1)$ with $H_{e,1} \in [C - W/2; C + W/2]$. The first probability is simply given by $\mathcal{W}(H_e, \tau)$. Because of the reflexivity of time and the symmetry of the Fokker-Planck equation (77), we have that the second probability is given by $\mathcal{W}(H_e, 1 - \tau)$. Therefore, we find for $\mathcal{P}(H_e)$

$$\mathcal{P}(H_e) = K \int_0^1 \mathcal{W}(H_e, \tau)\mathcal{W}(H_e, 1 - \tau)d\tau, \tag{80}$$

where K is a normalization constant.

7.2.1 Perturbation series solution

Because $\beta_\perp^e(H_e)$ decreases monotonically away from the wall, the idea is to use the solution of the heat equation in a uniform media with diffusivity Π_2 to obtain a perturbation solution of (77). We set $\mathcal{W}(H, \tau) = \mathcal{W}^0(H, \tau) + \varepsilon\mathcal{W}^1(H, \tau) + h.o.t$ and we write $\beta_\perp^e(H_e)$ as $1 - \varepsilon\frac{7H_e+2}{6H_e^2+9H_e+2} = 1 - \varepsilon\varphi(H_e)$ and let $\varepsilon \to 1$. Substituting those assumptions into (77) leads to the following partial differential equations for $\mathcal{W}^0(H_e, \tau)$ and $\mathcal{W}^1(H, \tau)$

$$\frac{\partial \mathcal{W}^0(H_e, \tau)}{\partial \tau} = \Pi_2 \frac{\partial^2 \mathcal{W}^0(H_e, \tau)}{\partial H_e^2} \tag{81}$$

$$\frac{\partial \mathcal{W}^1(H_e, \tau)}{\partial \tau} = \Pi_2 \frac{\partial^2 \mathcal{W}^1(H_e, \tau)}{\partial H_e^2} + \varphi(H_e)\Pi_2 \frac{\partial \mathcal{W}^0(H_e, \tau)}{\partial H_e}. \tag{82}$$

$\mathcal{W}^0(H_e, \tau)$ is the solution of the heat equation on a finite interval with Neuman boundary conditions. Thus $\mathcal{W}^0(H_e, \tau)$ can be expressed as a cosine series whose coefficients are given as Fourier cosine series. $\mathcal{W}^1(\eta, \tau|\eta_0)$ is the solution of the non-homogeneous heat equation whose solution is a convolution of the fundamental solution and the non-homogeneous part. This approach has the main disadvantage that any higher order approximation of $\mathcal{W}$ will contain more convolutions of lower order terms. Therefore we will not pursue it any further.

7.2.2 Numerical solution

The first method to solve numerically the partial differential equation (77) is to use a spectral method combined with time-discretization (see [33]). For this method to be stable, the

eigenvalues of the linearized spatial discretization operator, scaled by the time step, must lie in the stability region of the time-discretization operator. However, this is not enough to ensure the robustness of the algorithm at small Π_2, since the initial distribution is a sum of discontinuous $\delta-$functions. Moreover, because the boundary condition is not of Dirichlet type, the problem has to be made symmetric by solving it on the domain $[-L, L]$ with zero boundary condition at the edge. This leads to other stability problems, since by making the non-constant diffusion $\beta^e_\perp$ symmetric, we also create a cusp at the origin.

Thus, we abandon this method, instead turning to the built-in Matlab function *pdepe*, which solves parabolic and elliptic partial differential equations in one space and time variable with initial condition and Dirichlet and Neumann boundary conditions. The algorithm described next (Alg. 7.1) combines the backward and forward solutions of the Fokker-Planck equation (77) to obtain $\mathcal{P}$ defined by equation (80). Let the matrix S be the numerical approximation of $\mathcal{W}(H_e, \tau)$ over the time-space mesh and let P be the approximation of $\mathcal{P}$.

Algorithm 7.1 Probability density function of matched particles

- Input: Π_2, C, W
- Given: L length of space interval, N number of space steps, N_t number of time steps
- Generate a linearly spaced time $[0, L]$ and space $[0, \Pi_2]$ grid
- Define pdeic: uniform initial condition on the window $[C - W/2, C + W/2]$ as Eq. (79)
- Define pdebc: Neumann boundary conditions as Eq. (78)
- Define pdepe: the partial differential equation as Eq. (77)
- Solve with *pdepe* to obtain S
- Matched particles time dependent distribution: $P_{temp} = S. * S(end : -1 : 1, :)$
- Integrate over time with a trapezoidal rule
- Normalize with a trapezoidal rule to get P
- Output: P

7.2.3 Comparison

We use algorithm 7.1 to compute the probability density function of matched particles for the same cases as in figure 28. For validation purposes the underlying histograms (red) are plotted together with P (blue) on figure 29.

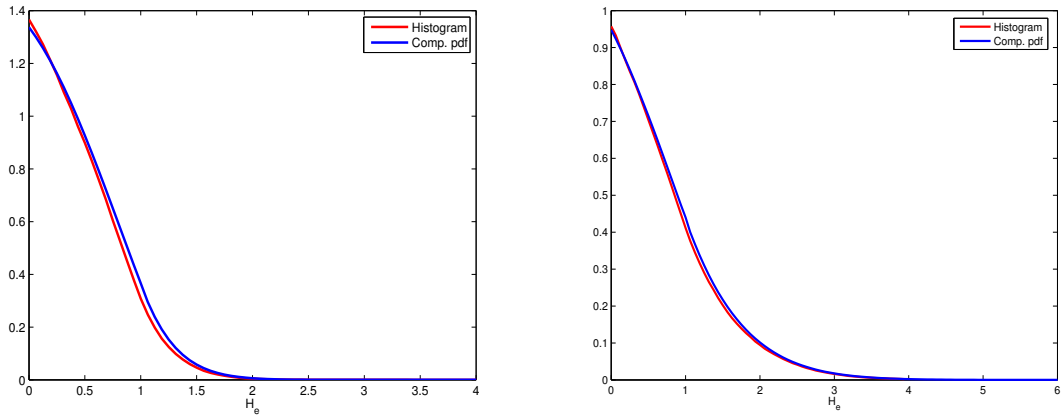

(a) $\Pi_2 = 1$ (b) $\Pi_2 = 5$

Figure 29: Comparison between the computed probability density function of matched particles and the histogram of matched particles at $C = 0.5$ and $W = 1$ for $\Pi_2 = 1$, $\Pi_2 = 5$.

In figure 30, we compare the histogram of the matched particles with the computed probability density function of matched particles P for two additional cases. On figure 30(a) the window has been shifted so that it does not touch the wall anymore, but it is centered at $C = 2.5$ with the same height $W = 1$. In figure 30(b) for the first window ($C = 0.5$, $W = 1$), Π_2 has been increased to 20.

The four plots in figures 29 and 30 demonstrate that algorithm 7.1 produces the same result as the histogram of the matched particles computed from the Langevin equation. The small differences between the two curves can be explained by numerical round-off errors during the normalization of both curves. There is an important computational gain by using a probabilistic method, even though the Fokker-Planck equation (77) can not be solved analytically. Computing and storing all the particles positions require a lot of RAM memory (256M) and a computational time varying between minutes and tens of minutes for a

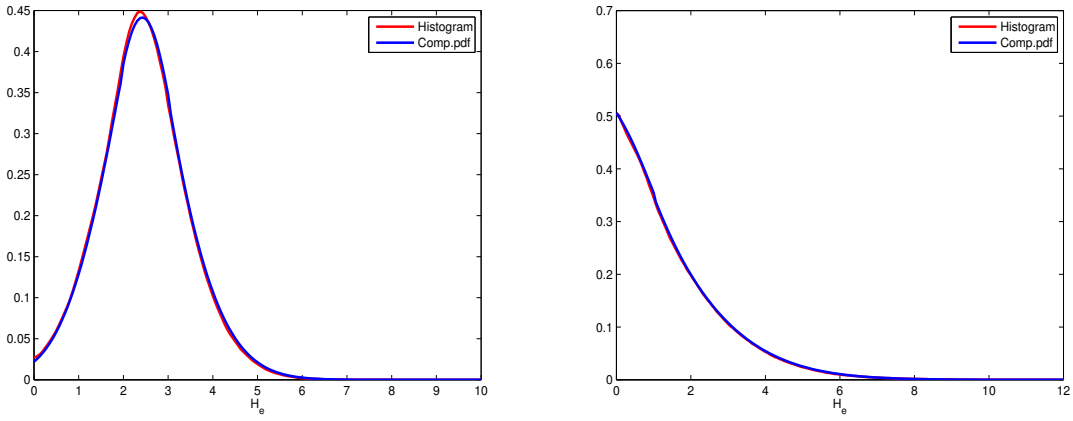

(a) $\Pi_2 = 4$, $C = 2.5$, $W = 1$

(b) $\Pi_2 = 20$, $C = 0.5$, $W = 1$

Figure 30: Comparisons between the computed probability density function of matched particles and the histogram of matched particles for different values of Π_2, C and W.

single group of dimensionless parameters. Because the Matlab function *pdepe* is very efficient, algorithm 7.1 runs in seconds, allowing rapid study of results across parameter values.

Following algorithm 7.1 a code has been developed that asks the user to input the measurement time T, the radius of the particles a, the dimensionless center C and width W of the window, the value for L the dimensionless diffusive length and return the probability density function of matched particles P together with its H_e and Z moments.

7.3 Results

7.3.1 Characterization of the bias

We use algorithm 7.1 to compute the probability density function of matched particles as a function of Π_2 to see when the uniform distribution assumption is valid. We set $a = 50$ nm, $C = 2.5$, $W = 5$ and vary T from 0.01 ms to 100 ms. Figure 31 is a waterfall plot of the probability density function of matched particles as a function of Π_2. If the dimensionless diffusive time Π_2 is small, the particles do not have time to move out of the window and as expected the distribution is uniform. As Π_2 increases, the probability density function

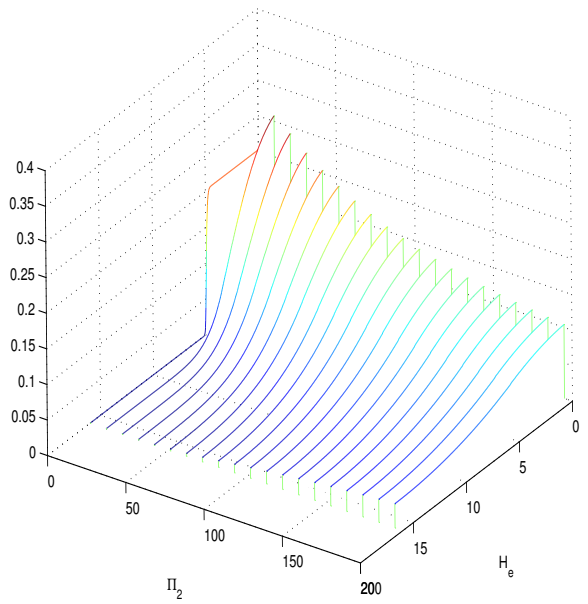

Figure 31: Probability density function of matched particles as a function of the dimensionless diffusive time Π_2 with $C = 2.5$ and $W = 5$.

starts by developing a peak close to the wall, before flattening and spreading over the entire region. This proves that assuming a uniform distribution of matched particles is only valid at Π_2 smaller than 0.1, in the case when $C = 2.5$ and $W = 5$. This corresponds for a particle of radius $a = 50$ nm to an exposure time T of approximately 0.05 ms. In nPIV $T = 2 - 5$ ms, thus the bias in the distribution of matched particles can not be neglected. However at microscale, with $a = 100 - 200$ nm the uniformity assumption, for $\Pi_2 < 0.1$ in the near-wall region is valid for an exposure time up to 1 ms.

In order to quantify the bias in the probability density function of matched particles we compute the moments of the distribution. The following figure (Fig. 32) contains the mean of the probability density function of matched particles for different values of the dimensionless diffusive time Π_2 compared to the center of the window C. We consider the nanoparticles setting with $a = 50$ nm, $C = 2.5$, $W = 5$ and we vary T from 0.01 ms to 95 ms (see also Fig. 31). The mean of a uniform distribution in the window $[C - W/2, C + W/2]$ is C. From figure 32 we note that the mean of the distribution of matched particles starts by

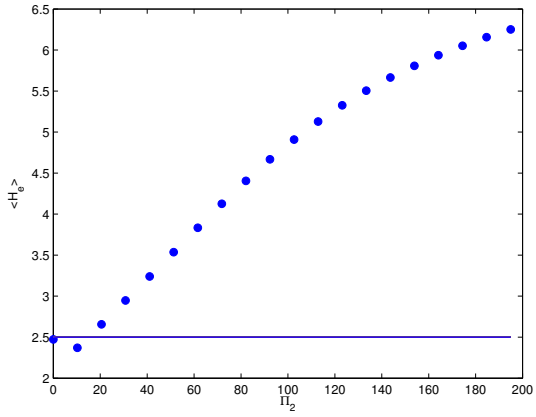

Figure 32: H_e mean of the probability density function of matched particles as a function of Π_2 with $a = 50$ nm, $C = 2.5$ and $W = 5$.

shifting to the left before becoming wider. Moreover, as Π_2 increases and the distribution gets broader, more and more particles move out of the window, so that the sampled location lies outside the window for $\Pi_2 > 105$.

The next plots (Fig. 33) are probability density function of matched particles for the first window for two experimental cases. In figure 33(a), we set $T = 2$ ms, $a = 50$ nm, $C = 2.5$ and $W = 5$ leading to $\Pi_2 = 4$ as in the experiments described by Yoda *et al.* ([38], [18], [30]), while on the right (Fig. 33(b)) we have $T = 10$ ms, $a = 5$ nm, $C = 10$ and $W = 20$ giving $\Pi_2 = 20500$ as reported by Pouya *et al.* ([27]) for quantum dots (QD). We remark that in the quantum dot case (Fig. 33(b)), particles diffuse on a longer scale, so that $L = 512$. Therefore $N = 8192$ and $N_t = 4096$, but algorithm 7.1 runs on a dual 2 GHz AMD Athlon processor with 2 GB RAM in less than five minutes. For both cases, the distribution is far from being uniform. For the nPIV case, we find $\overline{H_e} = 2.26$ compared to $C = 2.5$ and for the QD case we have $\overline{H_e} = 63.4$ compared to $C = 10$. Thus we conclude that the bias in the distribution of matched particles can be observed at nanoscales and it can be become dominant for quantum dots.

Finally, in figure 34 we look at the relation between the size of the window and the effects of the wall via hindered Brownian diffusion. We are mainly interested in the first window

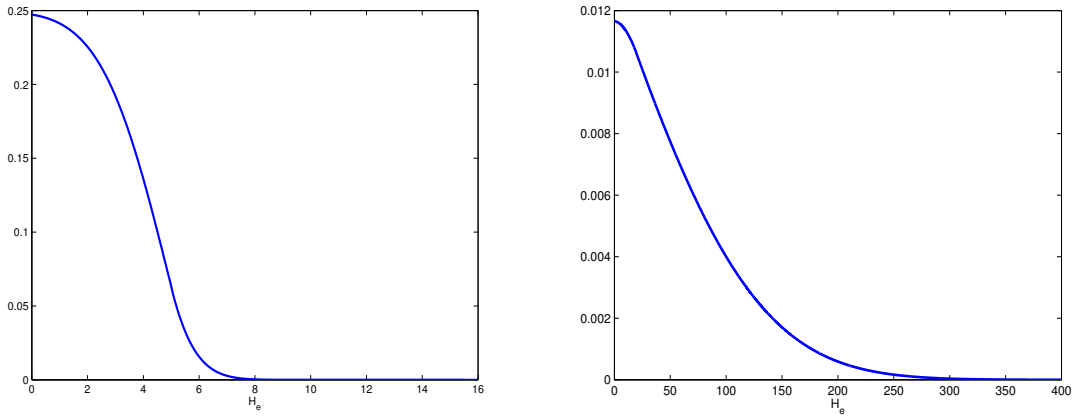

(a) nPIV: $\Pi_2 = 4\,C = 2.5\,W = 5$

(b) QD: $\Pi_2 = 20500$, $C = 10$, $W = 20$

Figure 33: Probability density function of matched particles in the first window for nPIV and quantum dot image velocimetry.

adjacent to the wall, thus we fix $W = 2C$. As W gets bigger, the particles do not have time to leave the window unless Π_2 is also increased; that is, the uniform distribution remains valid longer. However, if Π_2 is big enough, particles can drift out of the window again. On the other hand, as the window gets bigger, the wall effect diminishes, because the diffusion coefficient becomes constant to the Stokes-Einstein value D_∞. Therefore we expect the behavior of the location of the H_e mean of the distribution of matched particles to become similar for large windows. In order to compare the evolution of the H_e-mean

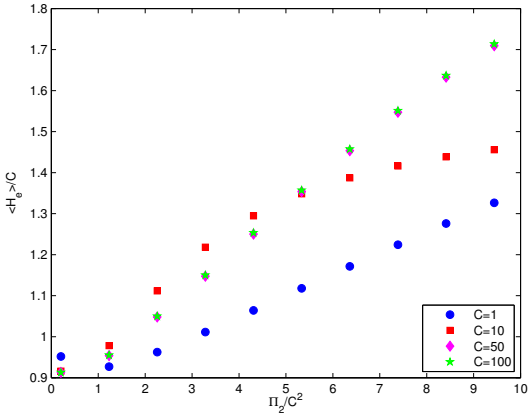

Figure 34: Comparison between rescaled H_e mean location of the probability density function of matched particles for $C = 1$, $C = 10$, $C = 50$ and $C = 100$ and $W = 2C$.

for the four windows $C = 1$ (blue circle), $C = 10$ (red square), $C = 50$ (purple diamond) and $C = 100$ (green star), we rescale the axis and now plot $\frac{H_e}{C}$ as a function of $\frac{\Pi_2}{C^2}$. From figure 34 we see that there is no difference between $C = 50$ (purple diamond) and $C = 100$ (green star). Therefore, this is a limiting curve showing that the effects of the wall become negligible for large enough windows. We remark that if the distribution were uniform, the value should be constant at 1. Thus, even for large windows we observe the same shifting of the probability density function of matched particles (first to the left and then to the right). Moreover in the large-window limit, where the diffusion coefficient is constant D_∞, the probability density function is an integral of a product of error functions, which when evaluated numerically agrees with the limiting curve observed in figure 34.

7.3.2 Slip or no-slip

Having established the bias in the H_e- and therefore Z- distribution of matched particles in experimental setting, we discuss its implication for the determination of slip length. The question of slip or no-slip at the wall goes back to Navier. At microscales, it has been established that the no-slip boundary condition holds. However, experimental results (see [16], [32], [34], [12], [20]) suggests that at nanoscale the no-slip boundary might be violated. Assuming that errors in the wall location are small, the slip at the wall is determined by linearly extrapolating the measured velocity to zero. If the velocity is zero at the wall, then there is no slip, else the slip length is the length which makes the velocity zero.

Let U be the measured velocity and let U_s be the sample mean velocity. U is an approximation of U_s. Since $\mathcal{P}$ is the probability density function of matched particles, we have with $u(Z)$ velocity profile

$$U_s = \int_a^\infty u(Z)\mathcal{P}(Z)dZ, \quad Z = H_e + 1. \tag{83}$$

First we consider a Couette flow of the form $u(Z) = GZ$ with no-slip. Then

$$U_s = G\int_a^\infty Z\mathcal{P}dZ = G\overline{Z}. \tag{84}$$

In other words, if U is measured over different $\overline{Z}$, G can be determined by linearly fitting

the values of U to $\overline{Z}$. We remark that U has previously always been set to the center of the window $C+1$, causing an erroneous value for G and even possibly slip. Experimentally, questions remain on how to change $\overline{Z}$, since it is not easy to change the size of the window W or to obtain with relatively small uncertainties data for more than three consecutive windows. However, it possible to change the elapsed time between measurements T and therefore Π_2.

In the case of slip, we have a linear flow of the form $u(Z) = G(Z+b)$ with b slip length and therefore the sample mean velocity U_s becomes

$$U_s = G\int_a^\infty Z\mathcal{P}(Z)dZ + Gb\int_a^\infty \mathcal{P}(Z)dZ = G\overline{Z} + Gb. \tag{85}$$

Again both G and b can be determined by a linear least square fit of U through $\overline{Z}$.

It is believed that the flow in near-wall region is mostly linear, but if this is not the case, a parabolic flow profile $u(Z) = FZ^2 + GZ + Gb$ could be recover using the second moment of the distribution of matched particles

$$U_s = F\overline{Z^2} + G\overline{Z} + Gb, \quad \overline{Z^2} = \int_0^\infty Z^2\mathcal{P}(Z)dZ. \tag{86}$$

This is now a non-linear least square fitting problem.

7.3.3 Multilayer PIV

Next, we turn our attention to errors in reported velocity field measurements. In their development of multilayer PIV Li *et al.* ([18]) compare the measured velocity in three layers to the expected mean velocity for different values of the dimensionless diffusive time Π_2. They find, especially in the first layer closest to the wall discrepancies of up to 6%. We show that those differences can be explained with the bias in the Z-distribution of matched particles.

We consider a shear flow of the form $u(Z) = GZ$ and we plot the ratio of the measured velocity U to the expected mean velocity U_m. U_m is the velocity in the middle of the window (corresponding to a uniform distribution), thus we have $U_m = G(C+1)$. Assuming that U is a good approximation of the sample mean velocity U_s we have $U \approx U_s = G\overline{Z}$ as in equation (84). Therefore we find for the ratio of U and U_m

$$\frac{U}{U_m} \approx \frac{\overline{Z}}{C+1}. \tag{87}$$

The three layers I, II, III for 50 nm radius particles in water at room temperature are defined in the following way: I: $1 < Z < 1.6$, II: $1.6 < Z < 2.7$ and III: $2.7 < Z < 7$. This corresponds to (in terms of H_e): $(C_I, W_I) = (0.3, 0.6)$, $(C_{II}, W_{II}) = (1.15, 1.1)$ and $(C_{III}, W_{III}) = (3.85, 4.3)$. We vary T from 1 ms to 4 ms corresponding to $\Pi_2 \in [2, 8]$. The result for each of the layer is plotted in figure 35 together with the values (empty symbols) for multilayer PIV reported by Li *et al.*. Because hindered Brownian motion decreases away

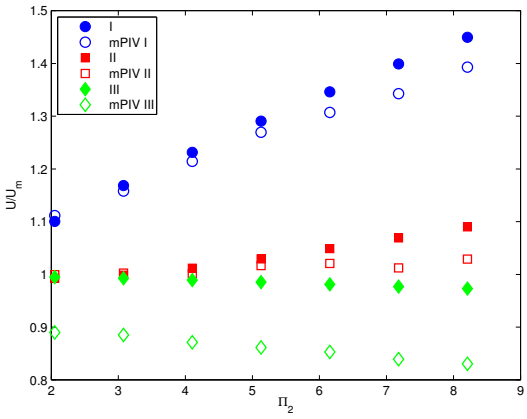

Figure 35: Ratio of U to U_m in layers I, II, III as a function of Π_2 compared with the values for mPIV reported by Li *et al.* ([18]).

from the wall, there is almost no bias in layer III and therefore U is really sampled in the middle of the window in the third layer. We remark that Li *et al.* report a value of 0.9 in layer III with a similar small decay as Π_2 increases, while we find a value of 1. It is believed, that evanescent waves and difficulties resulting from the illumination are responsible for the error in the last layer. Layer II does not present a bias as long as $\Pi_2 < 5$ in similarity with figure 34 and we see that in multilayers PIV where the values are almost constant

at 1, the illumination uncertainties are enough to correct for the bias. For layer I, the numbers in figure 35 obtained as a result of the bias in the distribution of matched particles follow almost exactly the curve described by Li *et al.* This demonstrates that errors in the measurement of the velocity field in the layer adjacent to the wall are dominated by the non-uniformity of the distribution of matched particles and can thus be corrected appropriately. In other words, the velocity sampled in the first window at nanoscale does not correspond to the velocity in the middle of the window.

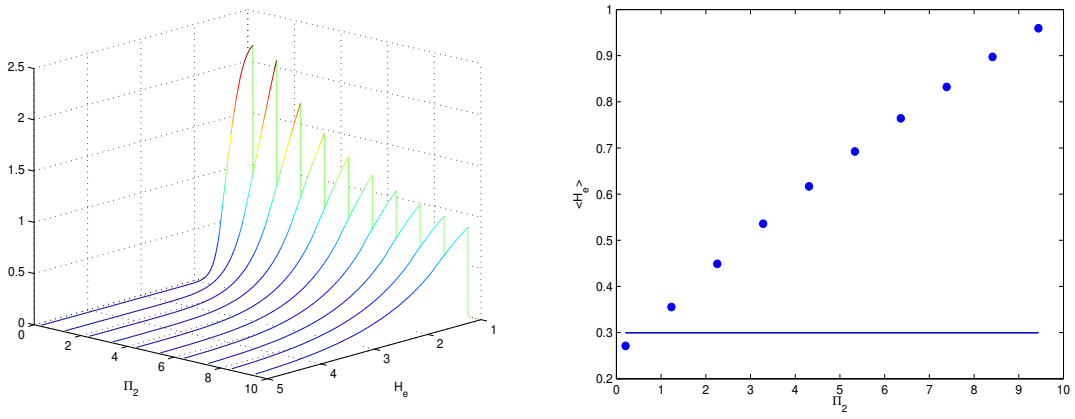

(a) Probability density function

(b) $\overline{H_e}$

Figure 36: (a) Probability density function of matched particles and (b) H_e mean as functions Π_2 for layer I.

Figure 36 consists of the waterfall plot of the probability density functions of matched particles (see Fig. 31(a)) and of the $\overline{H_e}$-location of matched particles as function of Π_2 (see Fig. 32) for layer I. We note that even for $T = 0.1$ ms, the distribution is not uniform and the center has shifted to the left. For all other values of T, the probability density function of matched particles becomes broader and consequently the center shift to the right. We remark that already for $T > 2$ ms ($\Pi_2 > 5$) the center of the distribution does not even lie in the window $[0, 0.6]$ anymore.

Finally, we use algorithm 7.1 to quantify the percentage of particles dropping-out of the

window between the elapsed measurement time T. If all the particles remain in the window, the probability density function $\mathcal{W}(H_e, 1)$ is uniform and its integral is 1. Therefore the drop-out is defined as

$$dropout = 1 - \int_{C-W/2}^{C+W/2} \mathcal{W}(H_e, 1) dH_e, \tag{88}$$

where $\mathcal{W}(H_e, 1)$ is the solution of the Fokker-Planck equation (77) at $\tau = 1$. In figure 37 we plot the drop-out percentage as a function of Π_2 for the first layer. The plot (Fig. 37)

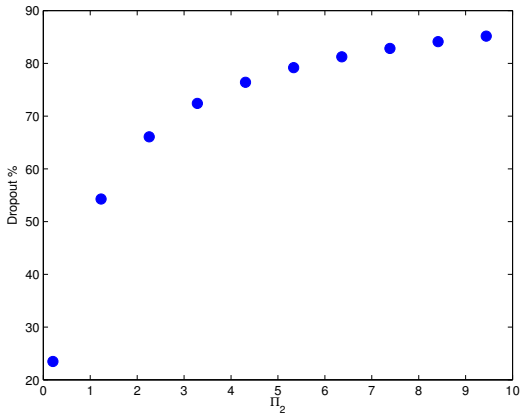

Figure 37: Dropout percentage as a function of Π_2 in layer I.

confirms that particles dropping-out of the window is a relevant issue. In fact, already for $T = 0.6$ ($\Pi_2 = 1.23$) more than 50% of the particles present in layer I do not remain in the layer at time T.

All the previous examples demonstrate the strength of algorithm 7.1 in determining the influence of particle mismatch and particle drop-out at nanoscale. It is expected (see Fig. 33(b)) that such effects remain for quantum dot image velocimetry. Those results are being applied to slip observations made by Joseph *et al.* ([12]), Lumma *et al.* ([20]) and Tretheway *et al.* ([34], [32]). We remark that for the latter one, the displacement is obtained via averaging the cross-correlation function over 50 image pairs. This means that the initial distribution of particles is not uniform, but has to be replaced by $\mathcal{W}(H_e, 1)\chi_{[C-W/2, C+W/2]}$.

CHAPTER VIII

BROWNIAN MOTION AND CORRELATION IN NPIV

The central element in the determination of mean displacements with PIV is the cross-correlation peak (see Chap. 6). If background noise dominates the measurement or if the displacements are not comparable, the location of the peak can not be found with certainty. Therefore there exists a close connection between the geometrical properties of the peak, Brownian motion and the illumination thechnique.

For light-sheet illumination and μPIV, Olsen and Adrian ([23], [24], [25], [26]) derive a mathematical representation of images. They include Brownian motion, but not hindered Brownian diffusion and are limited to an intensity function not depending on z, the direction perpendicular to the wall. In the case of illumination through evanescent waves, the intensity function is an exponentially decaying function of z of the form $I_0 \exp(\frac{-z}{z_p})$, where z_p is the penetration depth. We want to follow Olsen and Adrian to describe changes in the width and height of the cross-correlation peak due to hindered Brownian diffusion.

Let W_i be weighting functions defining the interrogation windows, $\mathbf{X}$ be the two-dimensional position vector in the image plane, $\mathbf{X_i}$ be the ith interrogation spot, $\mathbf{x}$ be the three-dimensional position vector in the fluid and let M be the magnification. Let I_{0i} define the shapes and intensities of the illumination pulses, $\mathcal{I}$ be the particle image intensity function per unit of intensity that illuminates the particle located at $\mathbf{x}$, and $g(\mathbf{x},t) = \sum_i \delta(\mathbf{x}-\mathbf{x}_i(t))$ indicate the Lagrangian position of each particle in the flow at time t.

Let $I_1(\mathbf{X})$ and $I_2(\mathbf{X})$ describe two images taken at time t_1 and t_2. We define mathematically the images in the following way.

Definition 8.1

$$I_1(\mathbf{X}) = W_1(\mathbf{X} - \mathbf{X_1}) \int I_{01}(\mathbf{x})\mathcal{I}(\mathbf{X} - M\mathbf{x}; z)g(\mathbf{x}, t_1)d\mathbf{x}$$
$$I_2(\mathbf{X}) = W_2(\mathbf{X} - \mathbf{X_2}) \int I_{02}(\mathbf{x}')\mathcal{I}(\mathbf{X} - M\mathbf{x}'; z')g(\mathbf{x}', t_2)d\mathbf{x}'.$$

The Lagrangian position $g(\mathbf{x}, t)$ can be decomposed into mean parts $C(\mathbf{x}, t) = \overline{g(\mathbf{x}, t)}$ and fluctuating parts $\Delta g(\mathbf{x}, t)$ with $\overline{\Delta g(\mathbf{x}, t)} = 0$ so that $g(\mathbf{x}, t) = C(\mathbf{x}, t) + \Delta g(\mathbf{x}, t)$.

Definition 8.2 *The local cross-correlation of the two images is defined by*

$$R(\mathbf{s}) = \int I_1(\mathbf{X})I_2(\mathbf{X} + \mathbf{s})d\mathbf{X}.$$

Using the definitions of the images I_1 and I_2 as well as the decomposition of g into mean and fluctuation parts, we have

$$\begin{aligned} R(\mathbf{s}) &= \int I_1(\mathbf{X})I_2(\mathbf{X} + \mathbf{s})d\mathbf{X} \\ &= \int d\mathbf{X} \int W_1(\mathbf{X} - \mathbf{X_1})(C(\mathbf{x}, t_1) + \Delta g(\mathbf{x}, t_1))I_{01}(\mathbf{x})\mathcal{I}(\mathbf{X} - M\mathbf{x}; z)d\mathbf{x} \\ &\quad \int W_2(\mathbf{X} - \mathbf{X_2} + \mathbf{s})(C(\mathbf{x}', t_2) + \Delta g(\mathbf{x}', t_2))I_{02}(\mathbf{x}')\mathcal{I}(\mathbf{X} - M\mathbf{x}' + \mathbf{s}; z')d\mathbf{x}'. \end{aligned}$$

Let $R_D(\mathbf{s})$ be the displacement component of the cross-correlation function

$$\begin{aligned} R_D(\mathbf{s}) = \int d\mathbf{X} \int W_1(\mathbf{X} - \mathbf{X_1})\Delta g(\mathbf{x}, t_1)I_{01}(\mathbf{x})\mathcal{I}(\mathbf{X} - M\mathbf{x}; z)d\mathbf{x} \\ \int W_2(\mathbf{X} - \mathbf{X_2} + \mathbf{s})\Delta g(\mathbf{x}', t_2)I_{02}(\mathbf{x}')\mathcal{I}(\mathbf{X} - M\mathbf{x}' + \mathbf{s}; z')d\mathbf{x}'. \end{aligned} \tag{89}$$

Let $\mathbf{u}(\mathbf{x})$ be a velocity vector field. Let $f(\mathbf{x}', t_2; \mathbf{x}, t_1)$ be the probability density function that a particle at $(\mathbf{x}, t_1)$ moves into the volume $(\mathbf{x}', \mathbf{x}' + d\mathbf{x})$ at t_2 given $\mathbf{u}(\mathbf{x})$. It was shown by Olsen and Adrian ([23]) that the conditional space-time correlation can be written as

$$\overline{g(\mathbf{x}, t_1)g(\mathbf{x}', t_2)} = C(\mathbf{x}, t_1)C(\mathbf{x}', t_2) + C(\mathbf{x}, t_1)f(\mathbf{x}', t_2; \mathbf{x}, t_1). \tag{90}$$

We consider $\overline{R_D(\mathbf{s})}$ the conditionally averaged displacement cross-correlation for the velocity field $\mathbf{u}(\mathbf{x})$ over the interrogation window. From equations (89) and (90) and the definition of Δg we find

$$\begin{aligned} \overline{R_D(\mathbf{s})} = \int d\mathbf{X} \int W_1(\mathbf{X} - \mathbf{X_1})I_{01}(\mathbf{x})C(\mathbf{x}, t_1)\mathcal{I}(\mathbf{X} - M\mathbf{x}; z) \int W_2(\mathbf{X} - \mathbf{X_2} + \mathbf{s}) \\ I_{02}(\mathbf{x}')\mathcal{I}(\mathbf{X} - M\mathbf{x}' + \mathbf{s}; z')f(\mathbf{x}', t_2; \mathbf{x}, t_1)d\mathbf{x}'d\mathbf{x}. \end{aligned} \tag{91}$$

To simplify the previous equation (91) we will need the following lemma about the product of two Gaussians.

Lemma 8.1

$$\int_{-\infty}^{\infty} \exp\left(-\frac{(x-\mu)^2}{2\sigma}\right) \exp\left(-\frac{(kx-\nu)^2}{2\tau}\right) dx = \frac{\sqrt{2\pi\sigma\tau}}{\sqrt{\sigma k^2+\tau}} \exp\left(-\frac{(k\mu-\nu)^2}{2(\sigma k^2+\tau)}\right). \tag{92}$$

Proof

We complete the square

$$\begin{aligned}\frac{(x-\mu)^2}{2\sigma} + \frac{(kx-\nu)^2}{2\tau} &= \frac{x^2(\tau+k^2\sigma) - 2x(\tau\mu+k\sigma\nu)}{2\sigma\tau} + \frac{\mu^2}{2\sigma} + \frac{\nu^2}{2\tau} \\ &= \frac{(x\sqrt{\tau+\sigma k^2} - \frac{\tau\mu+\nu\sigma k}{\sqrt{\tau+\sigma k^2}})^2}{2\sigma\tau} + \frac{(k\mu-\nu)^2}{2(\sigma k^2+\tau)}.\end{aligned}$$

The result follows since

$$\int_{-\infty}^{\infty} \exp\left(-\frac{(x-\upsilon)^2}{2\kappa}\right) = \sqrt{2\pi\kappa}.$$

□

Without Brownian motion, the probability density function f is simply a delta function $f(\mathbf{x}', t_2; \mathbf{x}, t_1) = \delta(\mathbf{x}' - \mathbf{x} - \Delta\mathbf{x})$.

In the presence of Brownian motion, the probability density function f is given by (see, e.g, Chandrasekhar [4])

$$f(\mathbf{x}', t_2; \mathbf{x}, t_1) = \frac{1}{(4\pi D\Delta t)^{3/2}} \exp\left(\frac{-(\mathbf{x}' - \mathbf{x} - \Delta\mathbf{x})^2}{4D\Delta t}\right) \quad \Delta\mathbf{x} = \mathbf{u}\Delta t,$$

where D is the Stokes-Einstein diffusion coefficient.

8.1 Light-Sheet Illumination

The particle image intensity function is not a function of z and can be written as ([23])

$$\mathcal{I}(\mathbf{X}) = I_0 \exp\left(\frac{-4\beta^2\mathbf{X}^2}{d_e^2}\right) \quad I_0 \text{ constant, } \beta^2 = 3.67,$$

where $d_e = \sqrt{M^2 d_p^2 + d_s^2}$ is the image diameter and d_s is the diameter of the point response function.

Theorem 8.1 *For light-sheet illumination in the absence of Brownian motion and under the assumptions that $C(\mathbf{x},t)$ and $\Delta\mathbf{x}$ are constant, the averaged displacement cross-correlation function* (91) *becomes*

$$\overline{R_D(\mathbf{s})} = \frac{C\pi I_0}{8\beta^2}\frac{d_e^4}{d_e^2}\int W_1(M\mathbf{x}-\mathbf{X}_1)W_2(M\mathbf{x}+M\Delta\mathbf{x}-\mathbf{X}_2)I_{01}(z)I_{02}(z+\Delta z) \exp\left(\frac{-2\beta^2(\mathbf{s}-M\Delta\mathbf{x})^2}{d_e^2}\right)d\mathbf{x}.$$

Proof

We substitute f and $\mathcal{I}$ into (91) to get

$$\overline{R_D(\mathbf{s})} = I_0^2 C\int d\mathbf{X}W_1(\mathbf{X}-\mathbf{X}_1)W_2(\mathbf{X}-\mathbf{X}_2+\mathbf{s})\int I_{01}(z)I_{02}(z+\Delta z)\exp\left(\frac{-4\beta^2}{d_e^2}(\mathbf{X}-M\mathbf{x})^2\right) \exp\left(\frac{-4\beta^2}{d_e^2}(\mathbf{X}-M\mathbf{x}-M\Delta\mathbf{x}+s)\right)d\mathbf{x}.$$

The integrand vanishes unless $\mathbf{X}\approx M\mathbf{x}\approx M\mathbf{x}+M\Delta\mathbf{x}-\mathbf{s}$ (see Olsen [23]).

Therefore we find for the previous integral

$$\overline{R_D(\mathbf{s})} = I_0^2 C\int d\mathbf{X}W_1(M\mathbf{x}-\mathbf{X}_1)W_2(M\mathbf{x}+M\Delta\mathbf{x}-\mathbf{X}_2)\int I_{01}(z)I_{02}(z+\Delta z) \exp\left(\frac{-4\beta^2}{d_2^2}(\mathbf{X}-M\mathbf{x})^2\right)\exp\left(\frac{-4\beta^2}{d_e^2}(\mathbf{X}-M\mathbf{x}-M\Delta\mathbf{x}+\mathbf{s})\right)d\mathbf{x}.$$

Using lemma 8.1 with $\mu = M\mathbf{x}$, $\tau=\sigma=\frac{d_e^2}{8\beta^2}$, $k=1$, $\nu = M\mathbf{x}+M\Delta\mathbf{x}-s$ we integrate with respect to $\mathbf{X}$

$$\overline{R_D(\mathbf{s})} = \frac{C\pi\mathcal{I}_{00}}{8\beta^2}\frac{d_e^4}{d_e^2}\int W_1(M\mathbf{x}-\mathbf{X}_1)W_2(M\mathbf{x}+M\Delta\mathbf{x}-\mathbf{X}_2)I_{01}(z)I_{02}(z+\Delta z) \exp\left(\frac{-2\beta^2(\mathbf{s}-M\Delta\mathbf{x})^2}{d_e^2}\right).$$

□

Olsen and Adrian ([23]) show that in the case of light-sheet illumination with Brownian motion the following expression holds.

Theorem 8.2 *For light-sheet illumination with Brownian motion and under the assumptions that $C(\mathbf{x},t)$ and $\Delta\mathbf{x}$ are constant, the averaged displacement cross-correlation function* (91) *becomes*

$$\overline{R_D(\mathbf{s})} = \frac{C\pi I_0^2}{8\beta^2}\int I_{01}(z)I_{02}(z+\Delta z)W_1(M\mathbf{x}-\mathbf{X}_1)W_2(M\mathbf{x}+M\Delta\mathbf{x}-\mathbf{X}_2) \left(\frac{d_e^4}{8d_e^2+8M^2\beta^2D\Delta t}\right)\exp\left(\frac{-2\beta^2(\mathbf{s}-M\Delta\mathbf{x})^2}{d_e^2+8M^2\beta^2D\Delta t}\right)d\mathbf{x}.$$

This shows, when compared to the result without Brownian motion (Thm. 8.1), that Brownian motion reduces the strength of the correlation by the ratio $d_e^2(d_2^2 + 8M^2\beta^2 D\Delta t)$ and broadens the diameter of the correlation peak from $\sqrt{2}d_e/\beta$ to $\sqrt{2}(d_e^2 + 8M^2\beta^2 D\Delta t)^{1/2}/\beta$.

8.2 μPIV

In microscopic PIV the image intensity function has the form

$$\mathcal{I}(\mathbf{X}, z) = \frac{A}{d_e(z)^2(s_0+z)^2}\exp\left(\frac{-4\beta^2\mathbf{X}^2}{d_e(z)^2}\right), \quad A, s_0 \text{ constant.}$$

The next theorem was discussed by Olsen and Adrian ([23]).

Theorem 8.3 *Assuming that perturbations due to Brownian motion are small, the averaged displacement cross-correlation function* (91) *becomes*

$$\overline{R_D(\mathbf{x})} = \frac{\pi A^2 I_{01} I_{02}}{8\beta^2}\int \frac{C(\mathbf{x},t)W_1(M\mathbf{x}-\mathbf{X}_1)W_2(M\mathbf{x}+M\Delta\mathbf{x}-\mathbf{X}_2)}{(s_0+z)^4 d_e^2}\frac{d_e^2}{d_e^2+8M^2\beta^2 D\Delta t}$$
$$\exp\left(\frac{-2\beta^2(\mathbf{s}-M\Delta\mathbf{x})^2}{d_e^2+8M^2\beta^2 D\Delta t}\right)d\mathbf{x}.$$

Theorem 8.3 demonstrates that the effect of Brownian motion on the signal strength is determined by the parameter $d_e^2(d_e^2 + 8M^2\beta^2 D\Delta t)$. However, since d_e varies through out the interrogation volume, this factor is hard to quantify other than numerically.

8.3 nPIV

We assume that $I_{01}(\mathbf{x})$, $I_{02}(\mathbf{x}')$, $C(\mathbf{x},t)$, $\Delta\mathbf{x} = \mathbf{u}(\mathbf{x})\Delta t$, and d_e the image diameter are constant. We set $\Delta z = 0$. Let z_p be the penetration depth.

We define an exponentially decaying intensity function

$$\mathcal{I}(\mathbf{X}) = I_0\exp\left(\frac{-z}{z_p}\right)\exp\left(-\frac{4\beta^2\mathbf{X}^2}{d_e^2}\right), \quad \beta^2 = 3.67. \tag{93}$$

With the above assumptions equation (91) becomes

$$\overline{R_D(\mathbf{s})} = I_{01}I_{02}CI_0^2\int d\mathbf{X}\int d\mathbf{x}W_1(\mathbf{X}-\mathbf{X_1})\exp\left(-\frac{z}{z_p}\right)\exp\left(-\frac{4\beta^2(\mathbf{X}-M\mathbf{x})^2}{d_e^2}\right)$$
$$\int d\mathbf{x}'W_2(\mathbf{X}-\mathbf{X_2}+\mathbf{s})\exp\left(-\frac{z'}{z_p}\right)\exp\left(-\frac{4\beta^2(\mathbf{X}-M\mathbf{x}'+\mathbf{s})^2}{d_e^2}\right)f(\mathbf{x}',t_2;\mathbf{x},t_1). \tag{94}$$

First, we study the influence of the exponentially decaying intensity function on the cross-correlation peak in the absence of Brownian motion. In this case, the probability density function f is a delta function $f(\mathbf{x}', t_2; \mathbf{x}, t_1) = \delta(\mathbf{x}' - \mathbf{x} - \Delta\mathbf{x})$.

Theorem 8.4 *For an exponentially decaying intensity function in the absence of Brownian motion, the averaged displacement cross-correlation function* (94) *becomes*

$$\overline{R_D(\mathbf{s})} = \frac{I_{01} I_{02} C I_0^2 \pi}{8\beta^2} \frac{d_e^4}{d_e^2} \int W_1(M\mathbf{x} - \mathbf{X_1}) W_2(M\mathbf{x} + M\Delta\mathbf{x} - \mathbf{X_2}) \exp\left(-\frac{2\beta^2(\mathbf{s} - M\Delta\mathbf{x})^2}{d_e^2}\right) \exp\left(-\frac{2z}{z_p}\right) d\mathbf{x}.$$

Proof

Substituting f into equation (94) we find

$$\overline{R_D(\mathbf{s})} = I_{01} I_{02} C I_0^2 \int d\mathbf{X} \int d\mathbf{x} W_1(\mathbf{X} - \mathbf{X_1}) \exp\left(-\frac{z}{z_p}\right) \exp\left(-\frac{4\beta^2(\mathbf{X} - M\mathbf{x})^2}{d_e^2}\right) W_2(\mathbf{X} - \mathbf{X_2} + \mathbf{s}) \exp\left(-\frac{z}{z_p}\right) \exp\left(-\frac{4\beta^2(\mathbf{X} - M(\mathbf{x} + \Delta\mathbf{x}) + \mathbf{s})^2}{d_e^2}\right).$$

The integrand vanishes unless the product of the two exponentials is large. Because both exponentials are narrow functions, this requires that $\mathbf{X} \approx M\mathbf{x} \approx M\mathbf{x} + M\Delta\mathbf{x} - \mathbf{s}$ and the previous equation simplifies to

$$\overline{R_D(\mathbf{s})} = I_{01} I_{02} C I_0^2 \int d\mathbf{X} \int W_1(M\mathbf{x} - \mathbf{X_1}) W_2(M\mathbf{x} + M\Delta\mathbf{x} - \mathbf{X_2}) \exp\left(-\frac{2z}{z_p}\right) \exp\left(-\frac{4\beta^2(\mathbf{X} - M\mathbf{x})^2}{d_e^2}\right) \exp(-\frac{4\beta^2(\mathbf{X} + \mathbf{s} - M\mathbf{x} - M\Delta\mathbf{x})^2}{d_e^2}\Big) d\mathbf{x}.$$

Next we integrate with respect to $\mathbf{X}$ using lemma 8.1 with $\sigma = \tau = \frac{d_e^2}{8\beta^2}$, $\mu = M\mathbf{x}$, $k = 1$ and $\nu = M\mathbf{x} + M\Delta\mathbf{x} - \mathbf{s}$. We find

$$\overline{R_D(\mathbf{s})} = \frac{I_{01} I_{02} C I_0^2 \pi}{8\beta^2} \frac{d_e^4}{d_e^2} \int W_1(M\mathbf{x} - \mathbf{X_1}) W_2(M\mathbf{x} + M\Delta\mathbf{x} - \mathbf{X_2}) \exp\left(-\frac{2\beta^2(\mathbf{s} - M\Delta\mathbf{x})^2}{d_e^2}\right) \exp\left(-\frac{2z}{z_p}\right) d\mathbf{x}.$$

□

Comparing the above result with theorem 8.1 for light sheet illumination we see that the negatively decaying intensity function results in a multiplication of the correlation peak by the exponential function $\exp(-2z/z_p)$.

Next we include hindered Brownian motion due to the presence of a wall located for simplicity at $z = 0$. Then the $z-$domain of integration is $[0, \infty]$. The probability distribution function f is given by Chandrasekhar ([4]), assuming a constant Stokes-Einstein diffusion coefficient D (in the region away from the wall), as

$$f(\mathbf{x}', t_2; \mathbf{x}, t_1) = \frac{1}{(4\pi D\Delta t)^{3/2}} \exp\left(-\frac{(x' - x - \Delta x)^2}{4D\Delta t}\right) \exp\left(-\frac{(y' - y - \Delta y)^2}{4D\Delta t}\right) \left[\exp\left(-\frac{(z' - z)^2}{4D\Delta t}\right) + \exp\left(-\frac{(z' + z)^2}{4D\Delta t}\right)\right].$$

Theorem 8.5 *For an exponentially decaying intensity function with hindered Brownian motion with constant Stokes-Einstein diffusion, the averaged displacement cross-correlation function* (94) *becomes*

$$\overline{R_D(\mathbf{s})} = \frac{CI_{01}I_{02}I_0^2\pi}{8\beta^2} \frac{d_e^4}{d_e^2 + 8M^2\beta^2 D\Delta t} \int W_1(M\mathbf{x} - \mathbf{X_1}) W_2(M\mathbf{x} + M\Delta\mathbf{x} - \mathbf{X_2}) \exp\left(-\frac{2\beta^2(\mathbf{s} - M\Delta\mathbf{x})^2}{d_e^2 + 8M^2\beta^2 D\Delta t}\right) \exp\left(-\frac{2z}{z_p}\right) \exp\left(\frac{D\Delta t}{z_p^2}\right) \left[erfc\left(\frac{\sqrt{D\Delta t}}{z_p} - \frac{z}{\sqrt{4D\Delta t}}\right) + \exp\left(\frac{2z}{z_p}\right) erfc\left(\frac{\sqrt{D\Delta t}}{z_p} + \frac{z}{\sqrt{4D\Delta t}}\right)\right] d\mathbf{x}.$$

Proof

Substituting f into equation (94) we find

$$\overline{R_D(\mathbf{s})} = \frac{I_{01}I_{02}CI_0^2}{(4\pi D\Delta t)^{3/2}} \int d\mathbf{X} W_1(\mathbf{X} - \mathbf{X_1}) W_2(\mathbf{X} - \mathbf{X_2} + \mathbf{s}) \int\int \exp\left(-\frac{z}{z_p}\right) exp\left(-\frac{z'}{z_p}\right) \exp\left(-\frac{4\beta^2(\mathbf{X} - M\mathbf{x})^2}{d_e^2}\right) \exp\left(-\frac{4\beta^2(\mathbf{X} - M\mathbf{x}' + \mathbf{s})^2}{d_e^2}\right) \exp\left(-\frac{(x' - x - \Delta x)^2}{4D\Delta t}\right) \exp\left(-\frac{(y' - y - \Delta y)^2}{4D\Delta t}\right) \left[\exp\left(-\frac{(z' - z)^2}{4D\Delta t}\right) + \exp\left(-\frac{(z' + z)^2}{4D\Delta t}\right)\right] d\mathbf{x}' d\mathbf{x},$$

where the $x'-$ and $y'-$integrals are over $(-\infty, \infty)$ and the $z'-$integral is over $[0, \infty)$.

First we integrate with respect to x' and y' using lemma 8.1 with $k = M$, $\mu = x + \Delta x$ or $\mu = y + \Delta y$, $\sigma = 2D\Delta t$, $\nu = s_x + X$ or $\nu = s_y + Y$ and $\tau = \frac{d_e^2}{8\beta^2}$. We find

$$\overline{R_D(\mathbf{s})} = \frac{I_{01}I_{02}CI_0^2}{\sqrt{4\pi D\Delta t}} \frac{d_e^2}{d_e^2 + 16M^2\beta^2 D\Delta t} \int d\mathbf{X} W_1(\mathbf{X} - \mathbf{X_1}) W_2(\mathbf{X} - \mathbf{X_2} + \mathbf{s}) \int\int \exp\left(-\frac{4\beta^2(\mathbf{X} + \mathbf{s} - M(\mathbf{x} + \Delta\mathbf{x}))}{d_e^2 + 16M^2\beta^2 D\Delta t}\right) \exp\left(-\frac{4\beta^2(\mathbf{X} - M\mathbf{x})^2}{d_e^2}\right) \exp\left(-\frac{z}{z_p}\right) \exp\left(-\frac{z'}{z_p}\right) \left[\exp\left(-\frac{(z' - z)^2}{4D\Delta t}\right) + \exp\left(-\frac{(z' + z)^2}{4D\Delta t}\right)\right] dz' d\mathbf{x}.$$

Again the integrand vanishes unless we have $\mathbf{X} \approx M\mathbf{x} \approx M\mathbf{x} + M\Delta\mathbf{x} - \mathbf{s}$.

Thus the previous equation simplifies to

$$\begin{aligned}\overline{R_D(\mathbf{s})} =& \frac{I_{01}I_{02}I_0^2C}{\sqrt{4\pi D\Delta t}} \frac{d_e^2}{d_e^2 + 16M^2\beta^2 D\Delta t} \int d\mathbf{X} \int\int W_1(M\mathbf{x} - \mathbf{X_1}) W_2(M\mathbf{x} + M\Delta\mathbf{x} - \mathbf{X_2}) \\ & \exp\left(-\frac{z}{z_p}\right) \exp\left(-\frac{z'}{z_p}\right) \exp\left(-\frac{4\beta^2(\mathbf{X} + \mathbf{s} - M(\mathbf{x} + \Delta\mathbf{x}))}{d_e^2 + 16M^2\beta^2 D\Delta t}\right) \exp\left(-\frac{4\beta^2(\mathbf{X} - M\mathbf{x})^2}{d_e^2}\right) \\ & \left[\exp\left(-\frac{(z'-z)^2}{4D\Delta t}\right) + \exp\left(-\frac{(z'+z)^2}{4D\Delta t}\right)\right] dz' d\mathbf{x}.\end{aligned}$$

We integrate with respect to X using lemma 8.1 with $k = 1$, $\mu = M\mathbf{x}$, $\nu = M\mathbf{x} + M\Delta\mathbf{x} - \mathbf{s}$, $\sigma = \frac{d_e^2}{8\beta^2}$ and $\tau = \frac{d_e^2 + 16M^2\beta^2 D\Delta t}{8\beta^2}$.

We have

$$\begin{aligned}\overline{R_D(\mathbf{s})} =& \frac{CI_{01}I_{02}I_0^2\pi}{8\beta^2\sqrt{4\pi D\Delta t}} \frac{d_e^4}{d_e^2 + 8M^2\beta^2 D\Delta t} \int W_1(M\mathbf{x} - \mathbf{X_1}) W_2(M\mathbf{x} + M\Delta\mathbf{x} - \mathbf{X_2}) \\ & \exp\left(-\frac{2\beta^2(\mathbf{s} - M\Delta\mathbf{x})^2}{d_2^2 + 8M^2\beta^2 D\Delta t}\right) \exp\left(-\frac{z}{z_p}\right) \int_0^\infty \exp\left(-\frac{z'}{z_p}\right) \left[\exp\left(-\frac{(z'-z)^2}{4D\Delta t}\right)\right. \\ & \left. + \exp\left(-\frac{(z'+z)^2}{4D\Delta t}\right)\right] dz' d\mathbf{x}.\end{aligned}$$

In order to evaluate the $z'-$integral we complete the squares in the following way

$$\begin{aligned}\frac{-z'}{z_p} - \frac{(z'-z)^2}{4D\Delta t} &= -\frac{\left(z' - (z - \frac{2D\Delta t}{z_p})\right)^2}{4D\Delta t} - \frac{z}{z_p} + \frac{D\Delta t}{z_p^2} \\ \frac{-z'}{z_p} - \frac{(z'+z)^2}{4D\Delta t} &= -\frac{\left(z' - (-z - \frac{2D\Delta t}{z_p})\right)^2}{4D\Delta t} + \frac{z}{z_p} + \frac{D\Delta t}{z_p^2}\end{aligned}$$

and we define the complementary error function *erfc(x)* as

$$erfc(x) = \frac{1}{\sqrt{\pi}} \int_x^\infty e^{-t^2} dt.$$

Then, setting $t = \frac{z' - \left(\pm z - \frac{2D\Delta t}{z_p}\right)}{2\sqrt{D\Delta t}}$ we have

$$\begin{aligned}\int_0^\infty \exp\left(-\frac{z'}{z_p}\right) \exp\left(-\frac{(z'-z)^2}{4D\Delta t}\right) dz' =& \exp\left(-\frac{z}{z_p}\right) \exp\left(\frac{D\Delta t}{z_p^2}\right) 2\sqrt{D\Delta t\pi} \\ & erfc\left(\frac{\sqrt{D\Delta t}}{z_p} - \frac{z}{2\sqrt{D\Delta t}}\right), \\ \int_0^\infty \exp\left(-\frac{z'}{z_p}\right) \exp\left(-\frac{(z'+z)^2}{4D\Delta t}\right) dz' =& \exp\left(\frac{z}{z_p}\right) \exp\left(\frac{D\Delta t}{z_p^2}\right) 2\sqrt{D\Delta t\pi} \\ & erfc\left(\frac{\sqrt{D\Delta t}}{z_p} + \frac{z}{2\sqrt{D\Delta t}}\right).\end{aligned}$$

Finally the averaged displacement cross-correlation function $\overline{R_D(\mathbf{s})}$ can be expressed as

$$\begin{aligned}\overline{R_D(\mathbf{s})} =& \frac{CI_{01}I_{02}I_0^2\pi}{8\beta^2}\frac{d_e^4}{d_e^2+8M^2\beta^2D\Delta t}\int W_1(M\mathbf{x}-\mathbf{X_1})W_2(M\mathbf{x}+M\Delta\mathbf{x}-\mathbf{X_2})\\ &\exp\left(-\frac{2\beta^2(\mathbf{s}-M\Delta\mathbf{x})^2}{d_e^2+8M^2\beta^2D\Delta t}\right)\exp\left(-\frac{2z}{z_p}\right)\exp\left(\frac{D\Delta t}{z_p^2}\right)\left[erfc\left(\frac{\sqrt{D\Delta t}}{z_p}-\frac{z}{\sqrt{4D\Delta t}}\right)\right.\\ &\left.+\exp\left(\frac{2z}{z_p}\right)erfc\left(\frac{\sqrt{D\Delta t}}{z_p}+\frac{z}{\sqrt{4D\Delta t}}\right)\right]d\mathbf{x}.\end{aligned}$$

□

To explain the effect of Brownian motion on the averaged displacement cross-correlation function $\overline{R_D(\mathbf{s})}$, we compare the results of theorems 8.4 and 8.5 in the same way as Olsen and Adrian derived their results for light-sheet illumination (Section 8.1). We find a similar influence of the Brownian motion, namely it reduces the strength of the correlation by the ratio $d_e^2(d_e^2+8M^2\beta^2\Delta t)$ and broadens the diameter of the correlation peak from $\sqrt{2}d_e/\beta$ to $\sqrt{2}(d_e^2+8M^2\beta^2D\Delta t)^{1/2}/\beta$ combined with an additional factor of the form

$$\exp\left(\frac{D\Delta t}{z_p^2}\right)\left[erfc\left(\frac{\sqrt{D\Delta t}}{z_p}-\frac{z}{\sqrt{4D\Delta t}}\right)+\exp\left(\frac{2z}{z_p}\right)erfc\left(\frac{\sqrt{D\Delta t}}{z_p}+\frac{z}{\sqrt{4D\Delta t}}\right)\right],$$

resulting form the hindered Brownian diffusion at the wall. This correction term is a function of z including complementary error function and it is therefore hard to quantify other than numerically.

This analysis can not be pursued further, because the next step would be to include a non-constant diffusion coefficient for hindered motion near a wall (e.g., Bevan-Prieve [2]), leading to integrals which are impossible to evaluate analytically.

CHAPTER IX

CONCLUSION

We studied fluid flow measurements in near-wall regions of microchannels. Many experimental parameters (polydispersity, image noise, corrections to the force exerted by the fluid, drop-out) have been left out in order to describe the basic stochastic properties of such a system. Hindered Brownian diffusion caused by the wall is included using the empirical Bevan-Prieve relation ([2]). The resulting Langevin equation in space is of the form

$$d\mathbf{X} = \mathbf{a}(\mathbf{X})d\tau + \mathbf{b}(\mathbf{X})d\mathbf{W} \quad dW^j = \mathcal{N}(0, d\tau),\ j = 1, \ldots, 3 \text{ and } \mathbf{b} = \sqrt{2\mathbf{D}(Z)\Pi_2},$$

where X, Y, Z are the dimensionless position of the particles in the XY-plane parallel to the wall, Z is the direction perpendicular to the wall and Π_2 is the dimensionless diffusive time.

Because the simulation is used to test a statistical hypothesis, we construct a numerical scheme with the biggest possible order of convergence. Since the system is coupled through the Z-component, the Milstein scheme requires the evaluation of double Ito integrals $\int\int dW^3 dW^1$. We showed in chapter 3 that the double Ito integrals can be numerically approximated with an Euler-Maruyama scheme as the solution of an appropriate system of stochastic differential equations. Moreover, we demonstrated that with $\Delta\tau$ small enough, the resulting scheme has strong order of convergence $\Gamma_1 = 1$ and weak order of convergence $\Gamma_2 = 1$.

Because experimental restrictions limit flow images to in-plane images, we developed a statistical reconstruction algorithm for the dependence of the velocity profile from the out-of-plane direction. The main idea is to assume that between two images particles have

moved in the X-direction according to one Euler step of the form

$$dX = \Pi_1 \gamma(aZ) + \sqrt{2\Pi_2 \beta_{||}(aZ)} dW \quad dW = \mathcal{N}(0,1),$$

where Π_1 is the dimensionless deterministic time and Π_2 is the dimensionless diffusive time. In chapter 4 and chapter 5, we showed that together with a uniform Z-distribution of particles in the window (in other words, the computation and observation domain are the same), this is a valid assumption. Since γ is the unknown profile, we used a maximum likelihood estimate based on the probability density function of perfect particle position and exact mean displacement to extract the velocity profile. Appropriate initial guess, penalization of the minimization function and average over different blocks of data are necessary to reduce the high sensitivity of the problem. We demonstrated the reconstruction for perfect particle identification (Chap. 4) and for exact mean (Chap 5) where the probability density function is obtained as a convolution. Finally, we extended the reconstruction algorithm to means approximated with particle image velocimetry (Chap 6). There are two main advantages of this reconstruction algorithm. First it is computationally fast (30 minutes) and second it does not use any information (like exponentially decaying intensity function) about the Z-location of the particles.

In chapter 7, we established that the distribution of particles that start uniformly in a window and end in the same window after a measurement time T (matched particles) is not uniform. Describing the distribution of particles with a Fokker-Planck equation, we constructed a fast algorithm for the estimation of the distribution of matched particles and of the resulting bias in its moments. After testing the algorithm against computer simulated data, we demonstrated its importance for experimentally relevant parameters bringing up the question of slip in near-wall region of microchannels and for quantum dot velocimetry.

We briefly mentioned in chapter 6 and in chapter 8 the effects of hindered Brownian diffusion on the cross-correlation peak. Those are analytically hard to quantify and very little remains known about them.

One of the major assumptions of the statistical reconstruction algorithm is that the distribution of matched particles is uniform. This was ensured by making the size of the computation domain equals the size of the observation domain. Therefore, the next step will be to replace this assumption by the correct non-uniform Z-distribution. This means that particles dropping-in and dropping-out of the field of vision become a relevant factor and that the number of particles in the window is not always n. Because we have developed an algorithm to compute the probability density function of matched particles, we want to incorporate it into the maximum likelihood estimate instead of the uniform Z-distribution. This will then allow for the comparison with some of the data obtain by Li *et al.* ([18]) about multilayers PIV. The problem can then be extended to the inclusion of more experimentally relevant factors like polydispersity or background noise.

The question of slip or no-slip in nanochannels is far from being answered. The algorithm developed for the distribution of matched particles is currently being jointly used with H. Li and M. Yoda to review velocity results presented in the literature.

Because the description of the images by Olsen does not clarify the effect of hindered Brownian motion on the cross-correlation peak, the approach of Breedveld *et al.* ([3]) could be adopted. This requires tracking particles positions, which is only a drawback for real experiments and not for computer simulations. Looking at the problem from this perspective, one might obtain more information about the role and effects of background noise and hindered Brownian motion on the cross-correlation peak.

Experimentalists have started to use quantum dots to measure flows in nanochannels ([27],[8]). This technique opens the door to a variety of theoretical and computational problems like the description of the system through a Langevin equation, the experimental relation for hindered Brownian diffusion, the Euler statistical assumption, the range of the dimensionless parameter Π_2 or the description of images through cross-correlation.

REFERENCES

[1] Adrian, R. J., "Particle-imaging techniques for experimental fluid mechanics," *Annual Review of Fluid Mechanics*, vol. 23, pp. 261–304, 1991.

[2] Bevan, M. A. and Prieve, D. C., "Hindered diffusion of colloidal particles very near to a wall: revisited," *Journal of Chemical Physics*, vol. 113, no. 3, pp. 1228–1236, 2000.

[3] Breedveld, V., den Ende, D. V., Tripathi, A., and Acrivos, A., "The measurement of the shear-induced particle and fluid tracer diffusivities in concentrated suspensions by a novel method," *Journal of Fluid Mechanics*, vol. 375, pp. 297–318, 1998.

[4] Chandrasekhar, S., "Stochastic problems in physics and astronomy," *Reviews of Modern Physics*, vol. 15, no. 1, pp. 1–89, 1943.

[5] Dufresne, E. R., Squires, T. M., Brenner, M. P., and Grier, D. G., "Hydrodynamic coupling of two Brownian spheres to a planar surface," *Physical Review Letters*, vol. 85, no. 15, pp. 3317–3320, 2000.

[6] Ermak, D. L. and McCammon, J. A., "Brownian dynamics with hydrodynamic interactions," *Journal of Chemical Physics.*, vol. 69, no. 4, pp. 1352–1360, 1978.

[7] Fuller, G. G., Rallison, J. M., Schmidt, R. L., and Leal, L. G., "The measurements of velocity gradients in laminar flow by homodyne light-scattering spectroscopy," *Journal of Fluid Mechanics*, vol. 100, pp. 555–575, 1980.

[8] Guasto, J. S., Huang, P., and Breuer, K. S., "Statistical particle tracking velocimetry using molecular and quantum dot tracer particles," in *Proceedings of IMECE2005*, 2005.

[9] Higham, D. J., "An algorithmic introduction to numerical simulation of stochastic differential equations," *SIAM Review*, vol. 43, no. 3, pp. 525–546, 2001.

[10] Hohenegger, C. and Mucha, P. J., "Statistical reconstruction of velocity profiles for nano particle image velocimetry." submitted SIAM Journal of Applied Mathematics.

[11] Huang, P., Guasto, J. S., and Breuer, K. S., "Direct measurement of slip velocities using three-dimensional total internal reflection velocimetry," in *Proceedings of IMECE2005*, 2005.

[12] Joseph, P. and Tabeling, P., "Direct measurement of the apparent slip length," *Physical Review E*, vol. 71, 2005.

[13] Kloeden, P. E., "The systematic derivation of higher order numerical schemes for stochastic differential equations," *Milan Journal of Mathematics*, vol. 70, pp. 187–207, 2002.

[14] Kloeden, P. and Platen, E., *Numerical solution of stochastic differential equations*. Berlin: Springer-Verlag, 1999.

[15] Lauga, E., "Apparent slip due to the motion of suspended particles in flows of electrolyte solutions," *Langmuir*, vol. 20, pp. 8924–8930, 2004.

[16] Lauga, E., Brenner, M. P., and Stone, H. A., *Handbook of Experimental Fluid Dynamics*, ch. Microfluidics: The no-slip boundary condtion. Springer-Verlag, 2005.

[17] Lauga, E. and Stone, H. A., "Effective slip in pressure-driven Stokes flow," *Journal of Fluid Mechanics*, vol. 489, pp. 55–77, 2003.

[18] Li, H., Sadr, R., and Yoda, M., "Multilayer nano-particle image velocimetry," 2005.

[19] Liang, D., Jiang, C., and Li, Y., "A combination correlation-based interrogation and tracking algorithm for digital PIV evaluation," *Experiments in Fluids*, vol. 33, pp. 684–695, 2002.

[20] Lumma, D., Best, A., Gansen, A., Feuillebois, F., Rädler, J. O., and Vinogradova, O. I., "Flow profile near a wall measured by double-focus fluorescence cross-correlation," *Physical Review E*, vol. 67, 2003.

[21] Meinhart, C. D., Wereley, S. T., and Santiago, J. G., "A PIV algorithm for examinating time-averaged velocity fields," *Journal of Fluids Engineering*, vol. 122, pp. 285–289, 2000.

[22] Meinhart, C., Wereley, S. T., and Santiago, J. G., "Piv measurements of microchannel flow," *Experiments in Fluids*, vol. 27, pp. 414–419, 1999.

[23] Olsen, M. G. and Adrian, R. J., "Brownian motion and correlation in particle image velocimetry," *Optics and Laser Technology*, vol. 32, pp. 621–627, 2000.

[24] Olsen, M. G. and Adrian, R. J., "Out-of-focus effects on particle image visibility and correlation in microscopic particle image velocimetry," *Experiments in Fluids*, pp. S166–S174, 2000.

[25] Olsen, M. G. and Adrian, R. J., "Measurement volume defined by peak-finding algorithms in cross-correlation particle image velocimetry," *Measurement Science and Technology*, vol. 12, pp. N14–N16, 2001.

[26] Olsen, M. G. and Bourdon, C. J., "Out-of-plane motion effects in microscopic particle image velocimetry," *Journal of Fluids Engineering*, vol. 125, pp. 895–901, 2003.

[27] Pouya, S., Koochesfahanil, M., Snee, P., Bawendi, M., and Nocera, D., "Singel quantum dot (QD) imaging of fluid flow near surfaces," *Experiments in Fluids*, vol. 39, pp. 784–786, 2005.

[28] Pozrikidis, C., *Boundary integral and singularity methods for linearized viscous flow*. Cambridge: Cambridge University Press, 1992.

[29] Sadr, R., Li, H., and Yoda, M., "Impact of hindered Brownian diffusion on the accuracy of particle-image velocimetry using evanescent-wave illumination," *Experiments in Fluids*, vol. 38, no. 1, 2004.

[30] Sadr, R., Li, H., and Yoda, M., "Bias due to hindered Brownian diffusion in near-wall velocimetry," PIV'05.

[31] Sadr, R., Yoda, M., Zheng, Z., and Conlisk, A., "An experimental and modeling study of electroosmotic bulk and near-wall flows in two-dimensional micro-and nanochannels," 2003.

[32] Thretheway, D. C. and Meinhart, C. D., "Apparent fluid slip at hydrophobic microchannel walls," *Physics of Fluids*, vol. 14, no. 3, pp. L9–L11, 2002.

[33] Trefethen, L. N., *Spectral methods in Matlab*. SIAM, 2000.

[34] Tretheway, D. C. and Meinhart, C. D., "A generating mechanism for apparent fluid slip in hydrophobic microchannels," *Physics of Fluids*, vol. 16, no. 5, pp. 1509–1515, 2004.

[35] Wereley, S. T. and Meinhart, C. D., *Diagnostic Techniques for Microfluidics*, ch. Micron-resolution particle image velocimetry. Springer-Verlag, in press.

[36] Westerweel, J., Geelhoed, P. F., and Lindken, R., "Single-pixel resolution ensemble correlation for micro-PIV applications," *Experiments in Fluids*, vol. 37, pp. 375–384, 2004.

[37] Willert, C. and Gharib, M., "Digital particle image velocimetry," *Experiments in Fluids*, vol. 10, pp. 181–193, 1991.

[38] Zettner, C. and Yoda, M., "Particle velocity field measurements in a near-wall flow using evanescent wave illumination," *Experiments in Fluids*, vol. 34, no. 1, pp. 115–121, 2003.